Mechanics of soil-blade interaction

A Thesis Submitted to the College of

Graduate Studies and Research

In Partial Fulfillment of the Requirements

For the Degree of Doctoral of Philosophy

In the Department of Mechanical Engineering

University of Saskatchewan

Saskatoon

By

Ahad Armin

Permission to use

In presenting this thesis/dissertation in partial fulfillment of the requirements for a Postgraduate degree from the University of Saskatchewan, I agree that the Libraries of this University may make it freely available for inspection. I further agree that permission for copying of this thesis/dissertation in any manner, in whole or in part, for scholarly purposes may be granted by the professor or professors who supervised my thesis/dissertation work or, in their absence, by the Head of the Department or the Dean of the College in which my thesis work was done. It is understood that any copying or publication or use of this thesis/dissertation or parts thereof for financial gain shall not be allowed without my written permission. It is also understood that due recognition shall be given to me and to the University of Saskatchewan in any scholarly use which may be made of any material in my thesis/dissertation.

Requests for permission to copy or to make other uses of materials in this thesis/dissertation in whole or part should be addressed to:

Head of the Department of Mechanical Engineering

University of Saskatchewan, College of Engineering

57 Campus Dr.

Saskatoon, Saskatchewan, S7N5A9, Canada

Abstract

The main objective of this research work is to develop a simulation procedure for modeling the soil-tool interaction for a blade of arbitrary shape. The primary motivation for this study is developing agricultural robots with limited power and pulling force to help farmers in crop production.

In this thesis, a finite element (FE) investigation of soil-blade interaction is presented. The soil is considered as an elastic-plastic material with the non-associated Drucker-Prager constitutive law. A separation procedure to model the cutting of soil and a method of calculating the forces acting on the blade are proposed and discussed in detail. The procedure uses a separation criterion that becomes active at consecutive nodes on the predefined separation surfaces. In order to mimic soil-blade sliding and soil-soil cutting phenomena contact elements with different properties are applied. To verify correctness of the FE model developed and the procedures used, the FE results are first compared with analytical results available for straight rectangular blades from classical soil mechanics theories; and then the FE results are compared with the experimental ones. Also the effects of blade width, depth and rake angle on blade's draft force were studied by simulating soil-blade interaction with different blade's dimensions.

After the analytical and experimental validation of the results for straight rectangular blade, the rectangular curved shape blade was modeled in order to investigate the effects of changing the blade's radius of curvature on the blade's draft force.

The soil interaction with straight triangular blade in different rake angles was simulated next. Since the analytical solutions are limited to rectangular blades, calculated draft forces for

triangular blade were verified only experimentally. The triangular and rectangular blades with the same width and depth of interaction were also investigated. The results showed that triangular blade draft force is around half of the amount of force acting on the rectangular blade with the same rake angle.

Also the effect of triangular blade's sharpness and changing the blade's radius of curvature on draft force was discussed. By changing the blade's sharpness, the draft forces of triangular blade were calculated in two conditions of constant blade's width and constant blade's contact length.

The approach presented in this thesis can be used to investigate the soil-tool interactions for real and more complex blade geometries and soil conditions, and ultimately for improving design of blades to be used in tillage operations.

Acknowledgement

I would like to express my earnest and heartfelt gratitude and appreciation to my supervisors Prof. Reza Fotouhi and Prof. Walerian Szyszkowski whose guidance, support and patience during all stages of this study enabled me to achieve success. I am also grateful for the help of my graduate advisory committee, Professors Jerzy A. Szpunar, James (J.D.) Johnston, and Mohamed Boulfiza for their helpful suggestions in general.

Financial support of this work provided by the University of Saskatchewan Graduate Scholarship and NSERC discovery grant is gratefully acknowledged. I am thankful to the Department of Mechanical Engineering for providing me a comfortable research environment.

I also want to thank my colleagues, Dr. Mohammad Vakil, Mr. Reza Aminzadeh, Mr. Ashkan Oghabi who helped me with my experiments and analysis. Also the help of departmental assistants, Mr. Douglas Bitner and Mr. Louis Ruth are greatly appreciated for helping me to setup the experiment setups and tests.

I would like to thank my dear mom and dad, and my brothers who have been a great emotional support for me from miles away. They are the people who have shaped me as a person that I am, and never stopped encouraging me through ups and downs.

Last but definitely not the least; I would like to express my deepest gratitude and appreciation to my dear wife, Nazanin. She is my whole life and as graceful as can be. I owe her for every bit of success I have had from the moment that she came into my life. She is the most important motivation for me to move forward and to be a better person each day passes by. Endless thank to her and her family.

Dedication

This thesis is dedicated to my father Naser Armin, my mother Mahdokht Mirhosseini and my dear wife Nazanin Samadi

Table of Contents

List of Figures

List of Tables

List of Symbols

B	Strain-displacement matrix for the element
c	Soil cohesion
C_P	Convergence parameter
d_s	Depth of soil block
d_1	Depth of cut soil
D	Material matrix
e	Element size on the separation plane
E	Modulus of elasticity
$f(\sigma)$	yield function
F	FEM blade's draft force
$\overline{F}$	FEM average force
F_e^p	Fictitious plastic force
F_e	Vector of external forces
F_D	FEM blade's draft force for particular conditions assumed in the simulation

F_{Vi}	Experimental vertical forces measured by load cells
F_{Di}	Experimental horizontal forces measured by load cells
F_{S1}	Experimental side force measured by side load cell
F_D^A	Analytical blade force
F_{DH}^A	Analytical horizontal blade force
g	Gravitational acceleration
h_1	Blade's total height
I_1	First invariant of the stress tensor
J_2	Second invariant of the stress deviator tensor
k	First material constants
K_e	Element stiffness matrix
(K_a, K_c, K_q)	Dimensionless cutting factors for wide blade
L_e	Length of additional soil
L_f	Maximum length of blade’s motion
L_v	Soil-blade sliding surface

L_h	Soil-soil separation surface
L_s	Length of soil block
M_x, M_y, M_z	Moments about, x, y, z axis
N	Matrix of the element's shape function
$(N_\gamma,\ N_c,\ N_q)$	Dimensionless cutting factors for narrow blade
$(N_{\gamma H}, N_{cH}, N_{qH})$	Horizontal components of cutting factors for narrow blade
$P_X, P_Y,\ P_Z$	Components of blade force
q_e	Nodal displacements
$Q(\sigma)$	Plastic potential function
Q_b	Bearing pressure
R	Radius of blade’s curvature
u	Distance traveled by the blade's tip
u_e	Displacement field of element
V_e	Volume of the element
w_1	Width of cut soil (also the width of blade)

w_2	Side widths of soil
w_s	Width of soil block
α	Blade rake angle
α_c	Angle of blade at the soil surface
α_{avg}	Average slope of blade
α_s	Sharpness angle of blade
β	Arc angle of blade
β_c	Second material constants
δU	Virtual change of total internal work
δW	Virtual change of external force work
δq_e^T	Arbitrary virtual increments
ε	Total strain vectors
ε_{el}	Elastic strain vectors
ε_P	plastic strain vectors
ε_x	Strain component (in the direction of the blade's motion)

ε_c	Limiting compacting strain
μ	Poisson's ratio
ρ	Density
σ	Stress vector
σ_n	Normal stress
σ_m	Mean stress or hydrostatic pressure
σ_i	Principal stresses
τ	Shear stress

Introduction and objectives

1.1. Introduction

According to [1], about half of the energy used in farming for crop production is consumed by tillage operation because of the high draft force generated when breaking and loosening the soil. In the past five decades, most soil-blade interaction research works were focused on developing models to predict the draft force for different soil conditions, tool geometry, and operating parameters such as depth of operation and tool direction [2]. Rather significant effects of these conditions and parameters on the force prediction have been demonstrated experimentally in several research works [3-6].

Analytical considerations of soil-blade interaction are typically restricted to straight blades and are based on a simplified limit analysis; nevertheless, when combined with experimental findings, they are widely used in design. The resulting formulas defining forces on blades during tillage operation can be found in [7] for two dimensional problems, and in [8] for three dimensional problems.

The blade shape obviously affects the form and size of the soil failure zone and consequently forces on the blade. In particular, it is known that curved blades work better than straight blades. Therefore, blades of more complicated geometries should be considered in optimization of the tillage operation. However, as already mentioned, any prediction of forces using analytical models would be limited to only a straight rectangular blade shape, and therefore not particularly useful in improving efficiency of tillage operations.

The Finite Element (FE) method has obviously a potential of modeling the interaction between soil and blades of arbitrary shapes and to find the blade force during this interaction. Also, such techniques can be used to obtain information about the failure zone, field of stress, soil

deformation, acting forces, and other parameters for any soil condition. Several models based on FE analysis to simulate soil-tool interaction and to obtain response of tools during these interactions have been presented in [9-18].

Two major challenges to be considered in the FE approach are the mechanical behavior of soil and the criteria for soil separation due to the cutting action of the blade [19]. Several models were proposed for simulating the constitutive law for soil; one of them is the Drucker-Prager's model that assumes a non-associated elastic plastic behavior [1]. From the numerical viewpoint soil separation is somewhat similar to the problem of cutting chips in machining operations [20-22], where various geometrical and physical separation criteria were developed based on critical values of displacements, strains, stresses, or strain energy to estimate the beginning of separation. A new criterion that uses the limit compacting strains in the direction of cutting is proposed here. When using this criterion to the FE model the soil particles are separated 'discreetly' at consecutive nodes starting from the node that is nearest to the cutting edge of the blade.

The overall objective of this research work is to develop a simulation procedure for modeling the soil-tool interaction for a blade of arbitrary shape. Developing limited power agricultural robots to help farmers in cultivation is the motivation of this study. Customized tillage tools which require less draft force and the same efficiency compared to existing ones should be designed so that they can be pulled by a robot.

Here the proposed procedure is tested on the straight blades in order to compare it with available analytical/experimental results from [7-8]. In particular, the use of contact elements modeling sliding and cutting as the blade moves through the soil is explained in detail, and the method of

calculating the draft force for the separation process that takes place discretely at successive nodes.

1.2. Objectives

In this research work a FE investigation of soil-blade interaction is presented. The general objective of this thesis is to propose a simulation procedure for modeling the soil-tool interaction for arbitrary shapes of a blade; this is done by verifying the amount of soil resistance force on blade of different shapes by comparing results from theoretical, experimental and FE Analysis. It is believed that the approach presented can be used to investigate the soil-tool interactions of real and more complex blade geometries, soil conditions and ultimately for improving design of blades used in tillage operations. A potential future plan can be to extend the procedure's applications to the analysis of blades of arbitrary shapes, which in turn can be used in developing software for optimization of the tillage operations.

This general objective has 5 distinct sub-objective defined as follows:

1. FE modeling and simulation procedure for modeling the soil-tool interaction

2. Developing a two-dimensional (2D) Finite Element Model of soil-blade interaction.

3. Developing a three-dimensional (3D) FE model of soil interaction with blades of rectangular and triangular shapes.

4. Validating the model by analytical and experimental results using tests performed in a soil bin facility.

5. Finding the effects of blade’s dimensions, rake angle and curvature on the draft force during the soil-blade interaction.

Literature review

1.3. Soil Properties

Amount of draft force acting on the blade during interaction with soil, is affected by the soil's physical and mechanical parameters. In this section the soil's physical and dynamic properties and their influence on draft force are discussed.

1.3.1. Soil physical properties

Soil physical properties include soil texture or structure that is associated with soil water content. Soil texture is one of the most important factors that may change the mechanical behavior and strength of soil. Soil texture classifies soils in several groups such as gravel, sand, silt and clay based on the size of individual grains [27]. Based on the "US Department of Agriculture" (USDA) standard, soil particles with diameter between 2-75mm are classified as gravel; consequently particles with finer diameters between 0.05-2mm are considered as sand and between 0.002-0.05mm considered as silt. The last group is clay in which the particle's diameters are less than 0.002mm. Based on [27], most soils do not fall in one specific category that is mentioned above and may be a mixture of two or more groups. Soils are classified based on the percentage of each category. It should be mentioned that by changing the soil texture, soil behavior will change, even though the mechanical condition stays same.

Another parameter that affects mechanical behavior of soil is its water content. Soil water content is the amount of water in the pore spaces of the soil particles calculated by:

$$\%\ \text{Soil water content} = \frac{(\text{mass of soil} - \text{dried mass of soil})}{\text{dried mass of soil}} \times 100$$

"Dried mass of soil" is the mass of soil after being dried for 24 hours in the temperature of $105^{\circ} C$ [27]. By changing the water content of soil, soil changes from a brittle solid (dry soil) to

viscous liquid (mud). By increasing the soil water content, soil strength is decreased from the lubricating effect of moisture layers on soil particles [3]. As [28, 29] concluded, the draft force for a dry bulk of soil would be much greater than moist soil.

1.3.2. Soil dynamic properties

As [30] stated, dynamic properties of soil are defined as those properties which appear through soil motion. Base on this definition, soil friction angle, soil cohesion and soil strength which are the operative factors during soil motion and interactions, are considered as *dynamic properties of soil*.

Since soil dynamic properties change during the soil motion, measuring dynamic properties of soil is very difficult. Moreover, placing the measuring devices in the soil may change soil reaction. As [30] mentioned, the results of similar experiments on the specific soil cannot be compared if the tests were performed under different soil conditions. The reason is based on different strength of soil for each condition. Therefore a typical way to handle this problem is assuming constant dynamic properties during soil interaction.

1.3.2.1. Soil Cohesion

Soil cohesion (c) is considered as a bonding force between soil particles per unit area [31] and is measured in (Pa). Soil cohesion is the force independent strength of soil. As mentioned above, physical properties such as soil texture and soil water content can affect cohesion which results from electrostatic bonds between clay and silt particles. Therefore, soils in the absence of clay or silt are not cohesive [32]. In soil mechanics, clays are classified as cohesive soils, whereas sand is considered as a non-cohesive soil. The relation between soil cohesion with soil texture and soil

water content is reported in [33, 34]. It is concluded that the more fine grained a soil is (high clay content), the greater the cohesion value.

1.3.2.2. Internal friction angle

Angle of internal friction (ϕ) is representing the existence of friction force between soil particles. Based on this definition, part of tillage energy is used to break the cohesive bonds between particles and their rolling and sliding on each other [2]. Same as soil cohesion, internal friction angle is affected by physical properties such as soil texture and soil water content. As [33, 34] concluded, normally coarse grained soils (high sand fraction) exhibit higher friction angles. Thus, sandy soils are considered as frictional soils because of their larger angle of internal friction in comparison with the clays. Internal friction angle mostly varied from 25° for moist and fine soil particles to about 45° for dry, dense, coarse soil particles [31].

1.3.3. Soil shear strength

According to [30] soil strength is the capability of soil to sustain an applied force. However soil strength may be affected by soil texture combination, but soil water content and bulk density are the most effective factors on soil strength changes. By expanding the volume of soil, the density of particles or bulk density decreases and subsequently strength will decrease. During tillage, soil can fail based on several effects such as shear, compression and tension. The shear effect on failure zone is higher than the other two. For years, many research works have been carried out in this field, but finally Coulomb proposed a general form of shear strength as shown below which is known as Mohr-Coulomb criteria.

$$\tau_{\max} = c + \sigma_n \tan\phi \qquad (2.1)$$

This criterion is used with triaxial test (shear strength test) to determine soil cohesion (c) and internal friction angle (ϕ). By drawing Mohr's circles based on triaxial test results on cylindrical soil sample and soil-failure line (a line tangent to Mohr's circles), soil cohesion (c) and internal friction angle of soil (ϕ) are determined (see Fig 3.2 in chapter 3.1). Cohesion is the intercept of the soil-failure line on the shear stress line and internal friction angle is the slope of the soil-failure line.

1.4. Analytical approach

Analytical approaches in soil tool interaction are based on limit analysis. As [35] stated, the concept of this method is to consider soil in the limit state, i.e. satisfying the condition (2.1). The other assumption is considering soil as a rigid body (non-deformable). Based on these assumptions, analytical approaches may be used to obtain information on the forces during soil-tool interaction. In the past five decades, several research studies were done in the area of soil-tool interaction in order to calculate the resultant forces on the soil and blade analytically [35]. The most practical research works which are focused on this topic are classified in two groups; two-dimensional and three-dimensional. When the width of the blade moving through the soil is ten times wider than its depth, the blade is considered a wide blade and approach is classified as two-dimensional; otherwise the blade is considered a narrow blade and a three-dimensional approach is more suitable [27]. The difference between wide and narrow blades is based on edge effects of soil movement outside of the width of blade [36]. In the narrow blade, considerable amount of soil moves sideways near edges of the moving soil zone, while in the wide blade the edge effect is negligible.

1.4.1. Two-Dimensional Models

Several equations were proposed to calculate soil resistance and forces acting on a wide blade during two-dimensional soil-blade interaction based on the logarithmic spiral method, which originally was developed by [37]. This logarithmic spiral method assumed that the soil in front of the tool consists of the Rankine passive zone [38] and the shear zone is limited by the logarithmic spiral curve as shown in Fig.2.1. Based on these assumptions, [37] proposed general two-dimensional equations as:

$$P = (\gamma_s d_1^2 N_\gamma + c d_1 N_c + Q_b d_1 N_q) w_1 \tag{2.2}$$

where γ_s is the soil specific weight, c is soil cohesion, Q_b is bearing pressure (due to soil accumulation), d_1 is cutting depth of the blade and $(N_\gamma,\ N_c,\ N_q)$ are dimensionless cutting factors that depend on the soil friction angle ϕ, and the blade rake angle α. This equation has been widely used for calculating forces acting on wide blades during interaction with the soil.

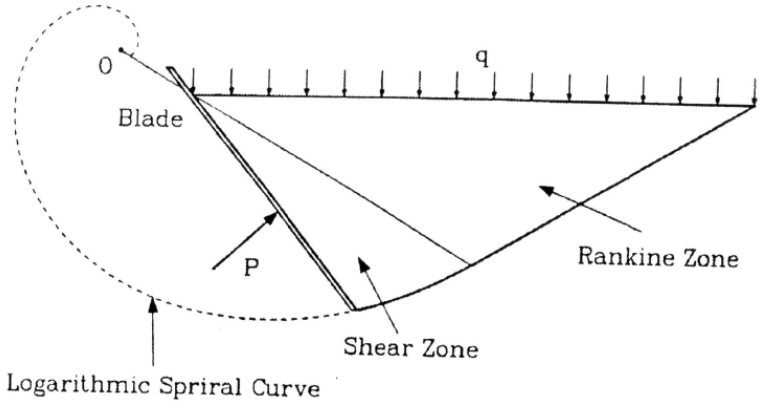

Figure 0.1: Logarithmic spiral failure method [35]

1.4.2. Three-Dimensional Models

As mentioned above, interaction between the soil and narrow blade is considered as a three-dimensional problem because of the edge effects of soil motion on the side of blade. Several three-dimensional soil cutting models were proposed to calculate the forces required for soil failure based upon empirical observations as follows.

1.4.2.1. Payne model

Based on soil mechanics theories and several experiments on soil failure shapes, [39] derived a three-dimensional soil failure model. Based on experimentally detected upward motion of soil in front of the blade during soil interaction, this model was developed as shown in Fig.2.2. The failure model was included by triangular center wedge, two side and one center crescent. By applying limited analysis on this model, resultant forces were derived, however solving these equations are fairly complicated and time consuming [35]. Authors of [40] showed experimentally that the shape of the failure zone is changed by changing the blade's geometry such as blade width and blade-soil interaction parameters including depth of interaction and blade's rake angle.

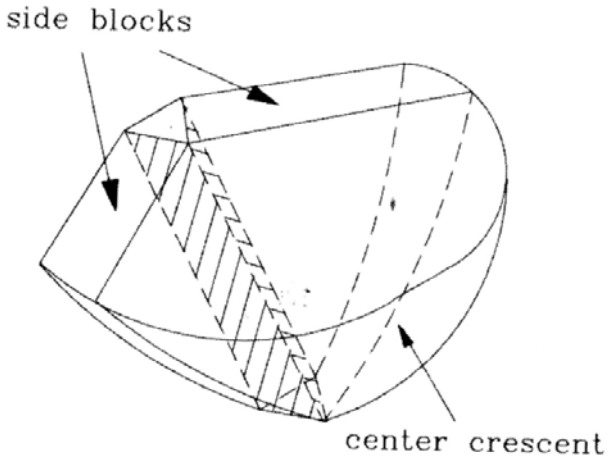

Figure 0.2: Payne's failure model [35]

1.4.2.2. O'Callaghan-Farrely model

Following Payne's soil failure model, [41] did several experiments on three different soils with vertical flat tines. Based on experimental observation, the soil failure formation was proposed as shown in Fig.2.3, which consisted of a forward failure section above critical depth and two horizontal crescents below the critical depth. Based on this model assumption, critical depth is equal to 0.6 of the tine width. The soil section above critical depth and in front of the tine is defined by two-dimensional logarithmic spiral method. The force results obtained from this model force equations are usually close to the test data except the force prediction when a very hard soil is interacted [42]. The main shortcoming of this model is related to its assumption as neglecting two side crescents above the critical depth. Also all tested tine plates were vertical and flat, and mass of the soil crescent below the critical depth was neglected [35].

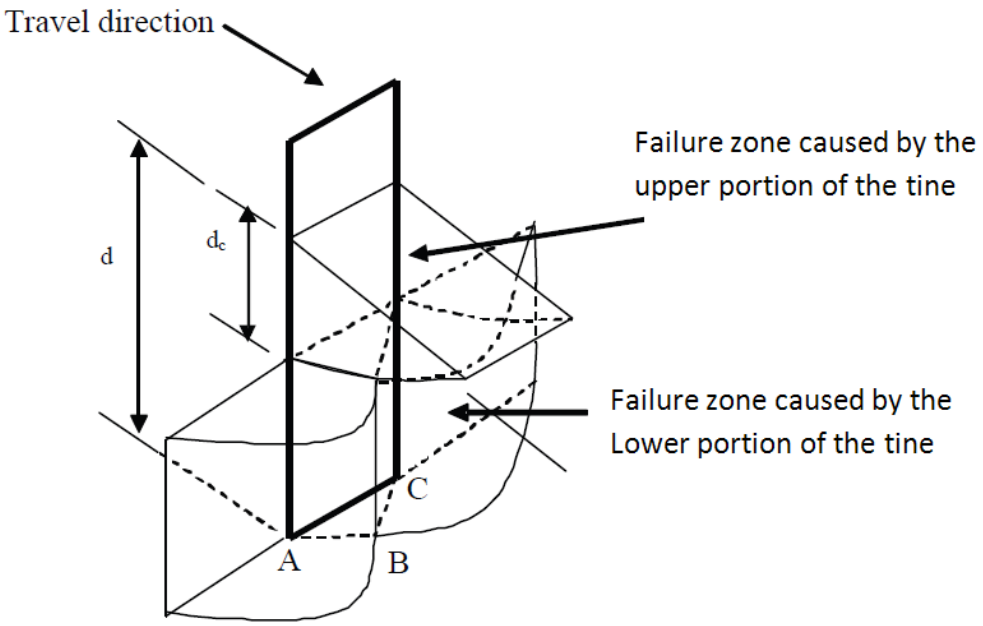

Figure 0.3: O'Callaghan-Farrely three-dimensional soil failure model [35]

1.4.2.3. Hettiaratchi-Reece model

A three-dimensional soil failure model, partially similar to the O'Callaghan-Farrely model was proposed by [42]. Same as previous model, Hettiaratchi and Reece assumed a critical depth for the blade and two horizontal transverse sections below the critical depth. A forward failure zone, in front of the soil-blade interface was also assumed as shown in Fig.2.4. Same as O'Callaghan-Farrely's model, the force related to the forward failure zone was determined by the two-dimensional equations. For transverse sections, three-dimensional equations were used in the same way as O'Callaghan-Farrely's model except that the gravitational component was counted in this model. However the effects of soil properties and tool geometries are included in the equations of this model, but this model is found to overestimate the blade force for vertical blades and under-predict for inclined blades [43].

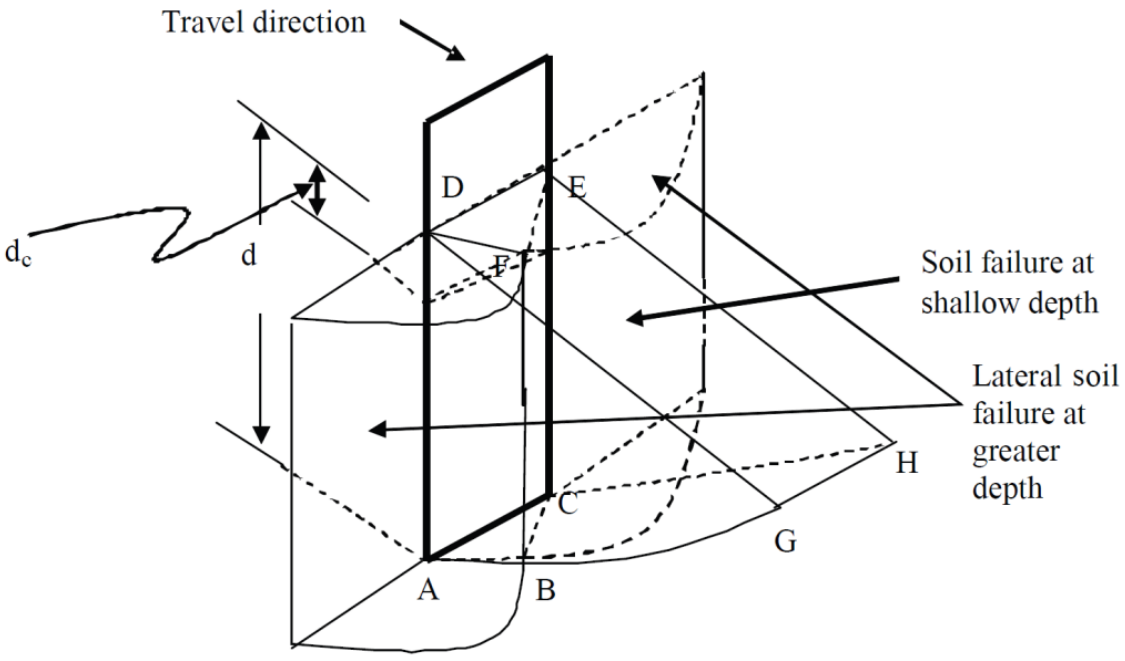

Figure 0.4: Hettiaratchi-Reece three-dimensional soil failure model [44]

1.4.2.4. Godwin-spoor model

In this soil failure model, six separate failure parts are assumed by [45]. Three sections include center wedge and two circular side crescents are located above the critical depth and three soil failure zones similar to Hettiaratchi-Reece's model are placed below the critical depth as shown in Fig.2.5. The total length of soil failure on the soil surface is defined by *r*, where this length would be changed by changing the soil strength or ratio of width to depth of blade [40]. However [40] performed several tests to estimate this rupture length (*r*), but according to [35], the determination of this length is still difficult.

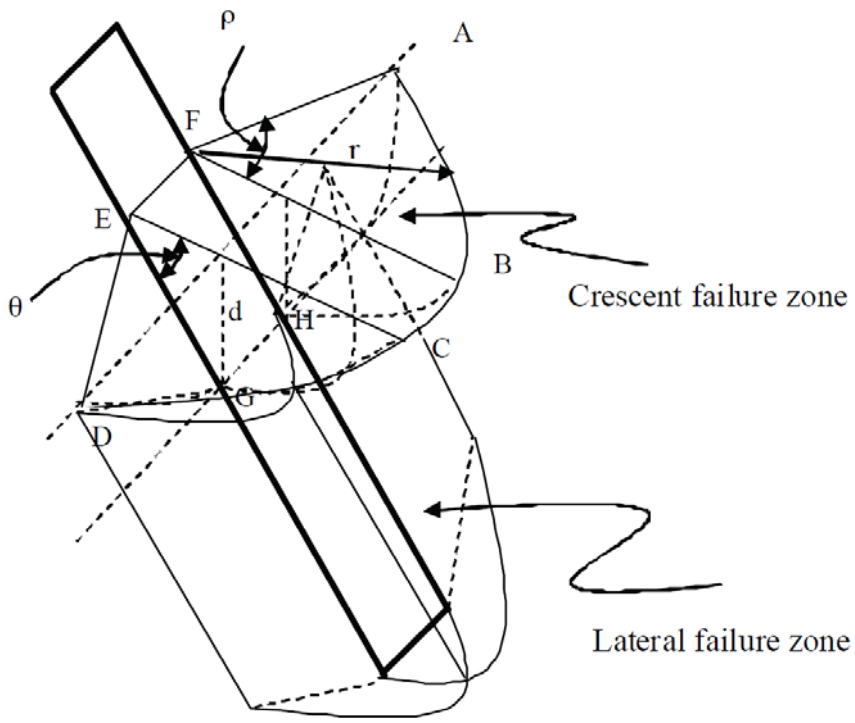

Figure 0.5: Godwin-spoor three-dimensional soil failure model [44]

1.4.2.5. McKyes-Ali model

A three-dimensional soil failure model without a need for experimental data such as rupture length, *r*, in Godwin-spoor's model was proposed by [8]. This model failure configuration is

almost similar to Godwin-spoor's model. The only difference is the assumption of flat planes for the bases of center wedge and circular side crescents in McKeys-Ali model in order to define the force direction at the base of failure zone as shown in Fig. 2.6. Since this model doesn't need prior information of the rupture length, using this model is much easier than the Godwin-spoor model. A set of graphs to determine dimensionless factors in the equations based on internal friction angle (ϕ) and external friction angle (δ) in order to make the equations more convenient to use was proposed by [25]. According to [46], the best correlation between analytical and experimental results can be achieved by using McKeyes approach.

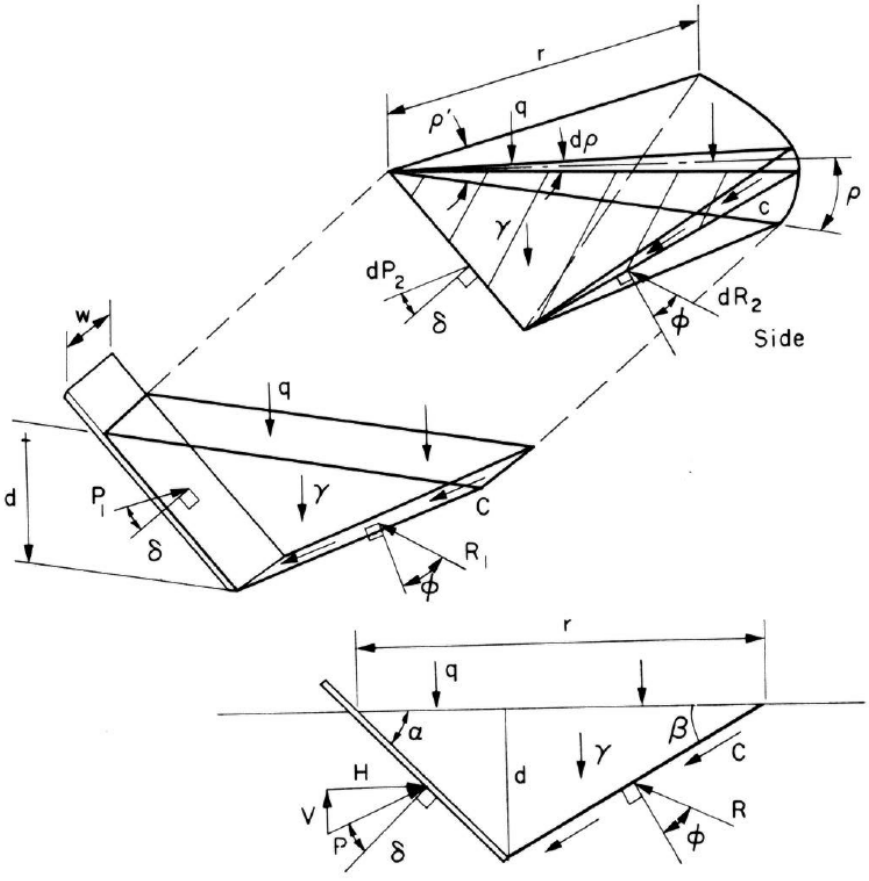

Figure 0.6: Three-dimensional soil failure model in front of a tool [8]

1.5. FE Method literatures

The previous section reveals that the limit analysis methods that are based on passive earth pressure theory have some serious restrictions. The major drawback of analytical methods is that they cannot provide enough information about soil deformations and displacements. This shortcoming is covered by developing numerical approaches such as FE method instead of conventional limit analysis methods.

The FE methods have led to the development of highly efficient numerical techniques that permit a more realistic simulation of the soil–tool interactions. These methods, if applied properly, can be used to predict the failure zone, field stress and deformation in the soil, and forces acting on blades without limitation on the shape of blades. Several Finite Element models have been presented to simulate soil-tool interactions as described in this chapter.

1.5.1. Constitutive law for FE soil modeling

The mechanical behavior, or stress-strain behavior of soil is the main challenge in the FE method. This constitutive equations, highly affect the accuracy of FE model results. Since soil is a non-linear material, the mechanical behavior of soil is very complex and cannot define the stress-strain behavior with a simple relationship [2]. Most of FE method research works can be classified in two groups based on types of their constitutive equations: nonlinear elastic and elasto-plastic models. Several studies performed based on considering soil as nonlinear elastic model [47-50]. These research works showed satisfactory results for some specific cases such as soil hydrostatic compression, but still more accurate soil behavior description is needed especially for soil deformation during soil interaction. Although during the soil cutting or soil-blade interaction, soil goes through extensive plastic deformations; but these models assumed the soil deformations as being totally recoverable.

Therefore, it is required to utilize elastic-plastic constitutive model to describe the soil behavior before and after soil failure more precisely. Several models were proposed for simulating the elastic-plastic constitutive law for soil; [52] is the most practical among them that assumes a non-associated elastic-plastic behavior. In this model, soil is considered as linear elastic material before soil failure and plastic deformation occurs after stresses reach the yield criteria.

1.5.2. FE Soil-blade interaction models

Improvement in computers and computational techniques has led to the development of a new generation of highly efficient numerical approaches to solve complicate engineering problems which are involved with both geometric and material nonlinearities [53].

Several research works investigated the soil-tool interaction by using a FE method that [14] classifies and tabulates them based on their significant features. Use of the FE method in soil-tool interaction has several advantages such as obtaining strain–stress information inside the entire soil; also there is no need to assume failure-zone geometry [35].

The first 2D FE soil-blade interaction was modeled by [47]. Using the plane strain assumption, the blade was considered a wide blade. Soil was divided in three sections, soil, soil-tool and soil-soil interfaces. The soil part was modeled with three-noded linear triangular elements whereas the soil-tool and soil-soil interfaces were modeled with 1D joint element with four-nodes as shown in Fig. 2.7.

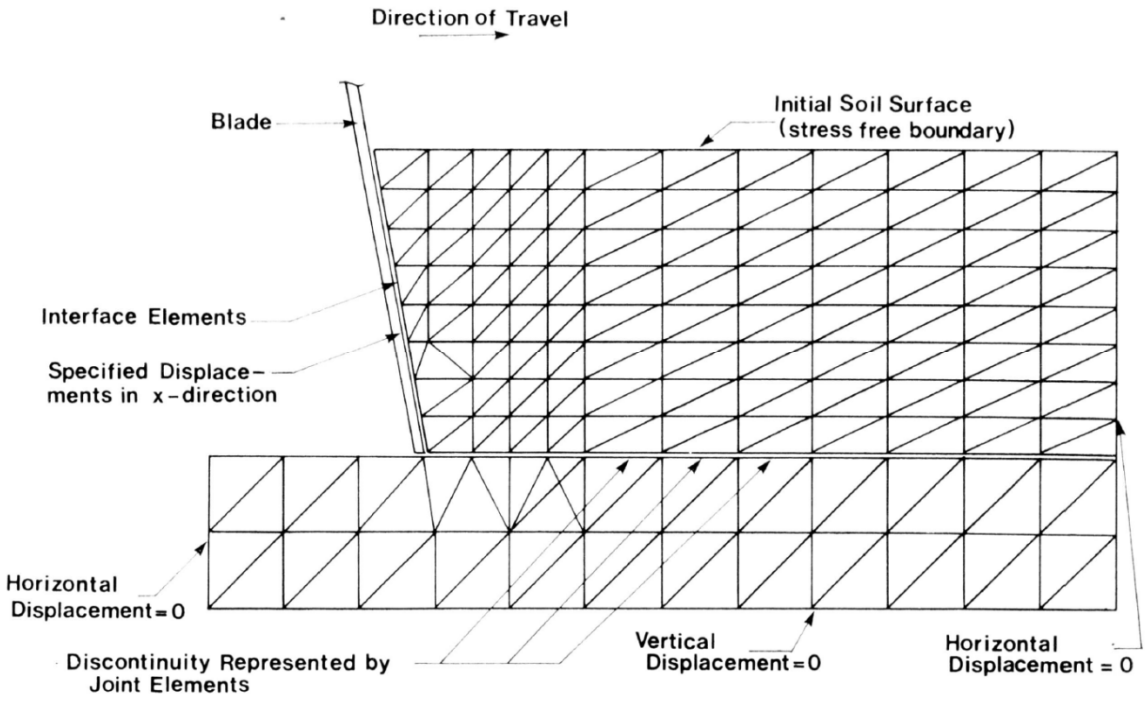

Figure 0.7: FE soil-blade interaction model [47]

These joint elements are attached to both triangular elements above and below of the interface that allow for large displacements. They modeled a blade with two different rake angles of 40° and 80° by assuming the soil as a nonlinear elastic material. They also performed several experiments to measure the forces and observe the soil deformations. The predicted force results and experimental blade forces had a good correlation [54].

The works in [55] developed a 3D soil-blade interaction model by considering the soil with Drucker-Prager material model. They also used artificial soil which is combined of sand, clay and spindle oil in order to decrease the effects of changing the moisture on the soil constitutive behavior. Soil-blade interface section was modeled with smooth 3D interface element. The soil was modeled with 8-noded brick element as shown in Fig.2.8. The force was applied at soil-tool interface nodes. By comparing to the experimental values, using interface element was being

necessary to make a correlation between force results. The FE force results were in agreement with experimental ones for the blade's rake angle of 30° and 45°. However the FE model under-predicted the draft force for a 75° rake angle. In general, their model prediction seemed to be stiffer compared with experimental results because of not considering the proper fracture propagation [54].

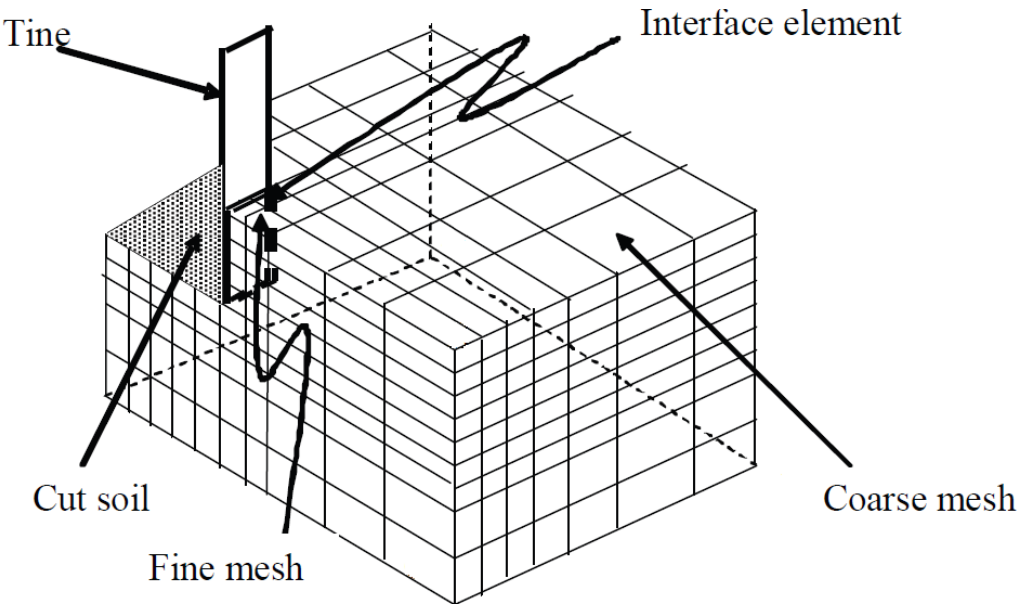

Figure 0.8: a typical 3D soil-blade interaction model shows interface element and mesh density [54].

A 3D soil-interaction with a narrow blade using material and geometrical nonlinearities was proposed by [56]. In this research work, soil was modeled as elastic-plastic with yield surface similar to the Mohr-Coulomb failure criterion. They simulated the soil-blade interface by using friction elements which connected nodes in the soil zone to corresponding nodes on blade. The novelty part of this study was on using frictional elements and considering specific stiffness for them. This element stiffness was selected based on the results of direct shear test data. [54] Did several tests to observe the soil deformation pattern and finding the blade's force.

Another 3D soil interaction model for narrow blade with 90° blade's rake angle was proposed by [48]. Soil constitutive relation was modeled based on Duncan and Chang hyperbolic model [12]. Also the Mohr-Coulomb criterion was assumed for soil failure. They compare their FE results with two analytical approaches, [8] and [57] which are based on limited analysis. As they claimed, their results were in reasonable agreement with calculated results from both two analytical models.

A 2D FE model in order to study the dynamic effect of soil-blade interaction was proposed by [58]. Similar to [48], Duncan and Chang's hyperbolic model was used for soil constitutive relation and soil failure was based on the Mohr-Coulomb criterion. Although [58] mentioned the presence of interface elements in the FE model, additional information was not provided [54]. Another issue that relates to the accuracy of this FE model was using 2D plain strain assumption for modeling a narrow blade (with 18 mm width); this may under-predict the blade force. By using this FE model, [58] compared the predicted draft forces for a vertical blade in soil-blade interaction with experimental results. These comparisons were indicated that during soil-blade interaction, blade draft force gradually increased with increase of blade's speed when this speed was less than 9km/h. But for a speed of more than 9km/h, draft force increased up to a peak value and then slowly dropped when blade moved further.

A dynamic soil-blade interaction to study high speed tillage for a narrow blade was proposed by [6]. The blade's speed was between 0.5 m/s to 10 m/s. Same as [58], soil constitutive equations followed the Duncan and Chang hyperbolic model. A special test facility was used to perform high speed soil-blade interaction for three different shapes the of blade: flat, triangular and elliptical shapes as shown in Fig. 2.9. It should be noted that the soil used for these experiments were Saskatchewan sandy clay loam soil. The blade's force was about 1% over-predicted for

blade's speed of 2.8m/s and 25% over-predicted for 8.4m/s speed. [6] Concluded that draft force of the triangular-shaped blade is less than the flat blade; it was also noted that the draft force of the elliptical-shaped blade is less than the triangular-shaped blade at higher speed. They believe that these results show the similarity of remolded soil and viscous fluid and that drag effects have more influence on draft force in comparison to soil strength [54].

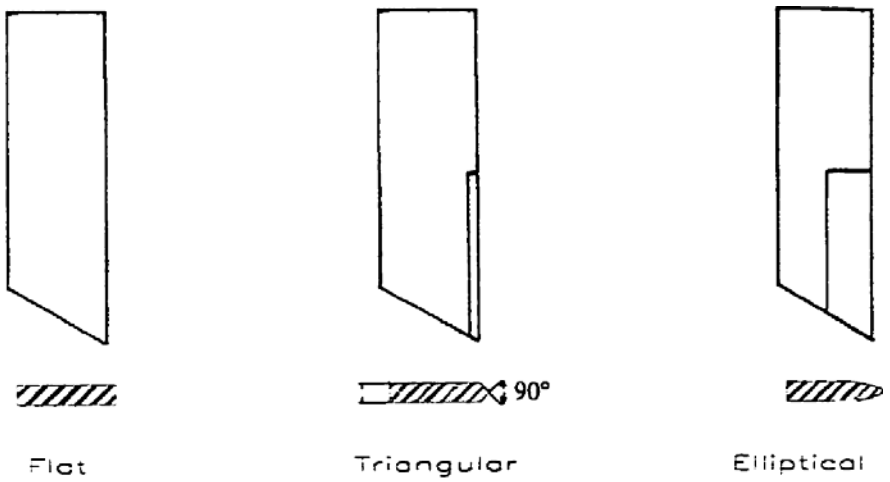

Figure 0.9: Tool's shape used in soil test [59]

[60] Proposed a 3D FE soil-blade interaction model in order to investigate the effect of non-homogenous sandy loam soil on the blade's force. The soil was modeled with an 8-noded brick element and considered as elastic-plastic materials with associated Drucker-Prager constitutive law. In order to verify the simulated results, they used four different subsoiler shanks and chisels with different angels and cutting depth. COSMOS, FE software was used to analyze this soil-blade interaction model. The FE results were over-predicted for both homogeneous and non-homogeneous soil in comparison with experimental results. This over estimation ranged from 11% to 16.8% for non-homogeneous soils and about 15% to 18.4% for homogeneous soils.

A 3D FE model for interaction between narrow blade and sandy soil was proposed by [9]. The effects of blade's speed and rake angle on the blade's draft force were investigated. The soil was modeled using an 8-noded brick element and considered as a hypo-plastic material. In this research work, two predefined failure surfaces were considered: a horizontal plane in direction of blade's motion and parallel to the tool tip and a vertical plane corresponding to the blade's edge. They performed several soil-blade simulations with different blade's speed and acceleration. Since non-cohesion sandy soil was used for simulation, the effect of speed on the draft force was minimal. They indicated that the force results for high blade speed has a short lived spike due to the rapid change of soil momentum and by further blade motion. The results show their independence from speed as [54] stated. Although [9] did not compare their results with analytical or other researcher work measured values, it was shown that the novelty of applying predefined failure surfaces in the soil-blade interaction modeling was very useful.

1.6. Experimental approach

Force comparison is the only viable testing approach in literatures that are used to validate analytical and simulation models of soil - tillage interaction. In this approach, the forces applied on several types of blades obtained by sensors are compared with simulation results in order to verify the simulation model. Experimentally, comparison of force results to validate the simulation model has 2 primary applications: first, it helps in design of tools, second, it helps to measure the dynamic properties of soil in the study of tillage mechanics. In this section, several types of field dynamometers and load cells that have been developed to sense the force acting on a tillage from the soil are introduced and discussed. Also, the soil bin facility, which used to validate our simulation results is described.

1.6.1. Force measurement instruments

A basic part of instruments which are used for draft-force measurements are force or pressure transducers. Dynamometers and load cells are instruments which are used for force measurements. Load cells can be categorized by the device that generates the output signal (pneumatic, hydraulic, electric) or by the way they detect force (bending, shear, compression, tension, torsion)

The operation of the load cells and dynamometers in agricultural and other applications are based on a single concept: force applied on the device creates a voltage proportional to the stress generated on the structure itself, which is translated into an electrical signal through the use of strain gauges.

Strain gauges are bonded onto a beam or structural member where it is deformed by applying load. In most cases, four strain gauges are connected in the form of a full Wheatstone bridge to obtain maximum sensitivity. Two of the gauges are usually in tension, while the other two are in compression, and all are wired with compensation adjustments. When a load is applied, the strain changes electrical resistance of the gauges proportional to the load.

Review of literature shows that several types of field dynamometers and load cells have been developed to sense the forces acting on the tillage from the soil; these devices can be divided into two main groups: first, externally located transducers and second, instrumented tillage tools, as [61] noted.

1.6.2. Externally located transducers:

Reports in this area include the design of two types of instruments: S-shape load cells and Extended Octagonal Ring dynamometer. Although the type of instrument that is used in soil-

tillage interaction has the main role in the accuracy of finding the loads, the location of these instruments is another factor that affects the accuracy of the resultant force.

The analysis of force in the soil tillage interaction system reveals that the complex set of forces and moments can be reduced to reactions in three principal axes: longitudinal, vertical, and lateral. Force instruments for such systems consist of individual strain gauges or load cells mounted on specific locations of the frame that support the tool, enabling the measurement of resultant forces. S-shape load cells are the most common load cells which are used in the soil-bins for measuring the forces during soil-tillage interaction. This type of load cell can provide an output if under tension or compression. When load is applied, the strain changes the electrical resistance of the gauges in proportion to the load that converts the force into measurable electrical signals. An S-shape six-load cell system that measures forces in three directions was used by [62]. The arrangement of the load cells was such that two load cells in the direction of tillage motion, measured the draft, three measured the vertical force, and one measured the side force. This arrangement of load cells is shown in Fig.2.10. The tool was attached to the bottom of the load frame, while the top of the frame was attached to the carriage. The forces from the tool were transmitted through six load cells to the carriage frame. This tool-force measuring system has been in use at the soil bin facility at the Department of Mechanical Engineering (formerly Agriculture and Bio resource Eng.), University of Saskatchewan since 1978. The details of how draft, vertical and lateral loads are generated from these load cells are explained in Sec. 4.1. The simulation results were validated based on this approach.

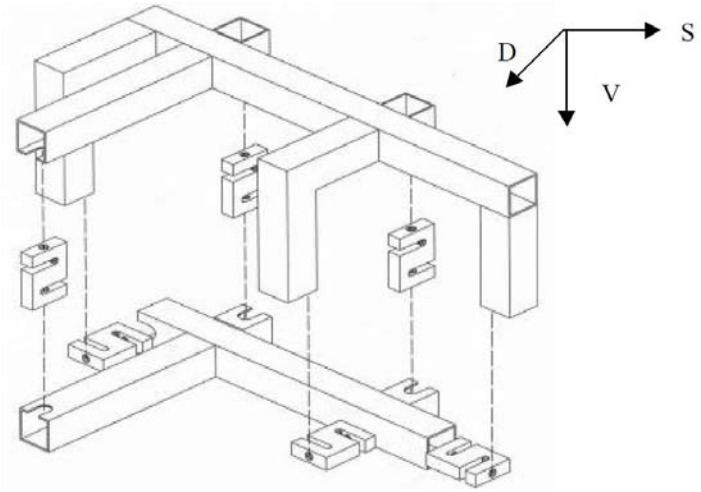

Figure 0.10: Six s-shape load cell arrangement [62].

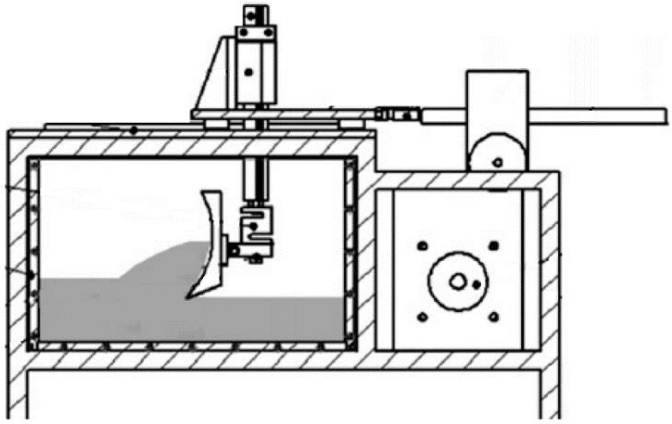

Figure 0.11: A schematic of soil box and the blade system [26].

Using one s-shape load cell in the horizontal direction and one load cell in vertical direction is another approach of using s-shape load cells. The issue with this approach is its low accuracy compared with the previous one. The soil-tool interaction model with discrete element method was simulated and the resultant draft forces were verified in the simple laboratory soil box by [26] as shown in Fig.2.11. The other deficiency of this method is ignoring the bending moment on vertical load cell. The problems with such an approach (using s-shape load cells for externally located transducer) include safety of the strain gauges which are exposed in s-shape load cells,

and inaccurate force prediction due to system frequencies that this causes low performance of the load cells in most of the soil bin tests [63]. These problems can be eliminated by use of the Extended Octagonal Ring (EOR) dynamometer as [61] noted.

EOR dynamometers that use strain gauges (usually connected in two full Wheatstone bridge circuits for high sensitivity) have been applied in many studies for measuring force acting on soil engaging implements as shown in Fig.2.12. EOR was led to Extended Multiple Octagonal Ring (EMOR) dynamometer that can measure force and moment much more accurately [64]. This type of dynamometer, based on mounting two EOR dynamometers "back-to-back", is able to attach to the carriage of the soil bin or framework for field measurements, as shown in Fig.2.13. In a follow-up research [65] tried to identify the optimal locations of the strain gauges on a double extended octagonal ring (DEOR) dynamometer which led in utilizing different strain gauge locations in order to increase the sensitivity of the dynamometer.

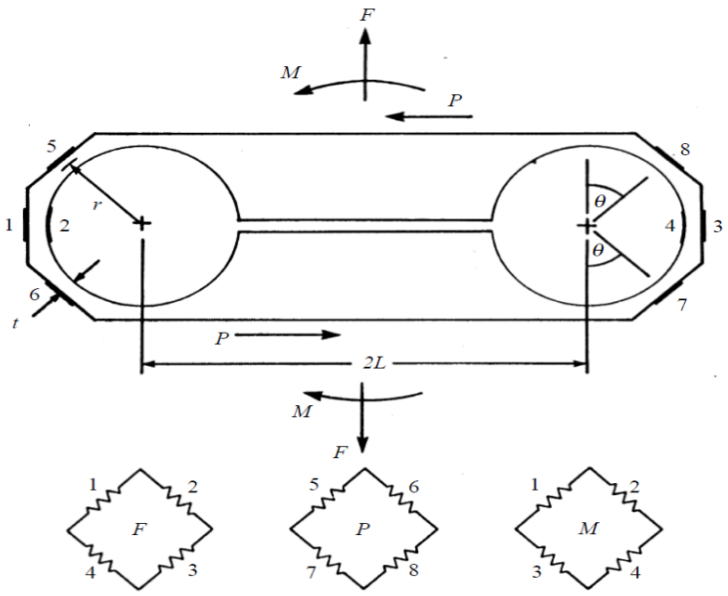

Figure 0.12: Extended Octagonal Ring showing applied forces, moments, and strain gauge bridges [64]

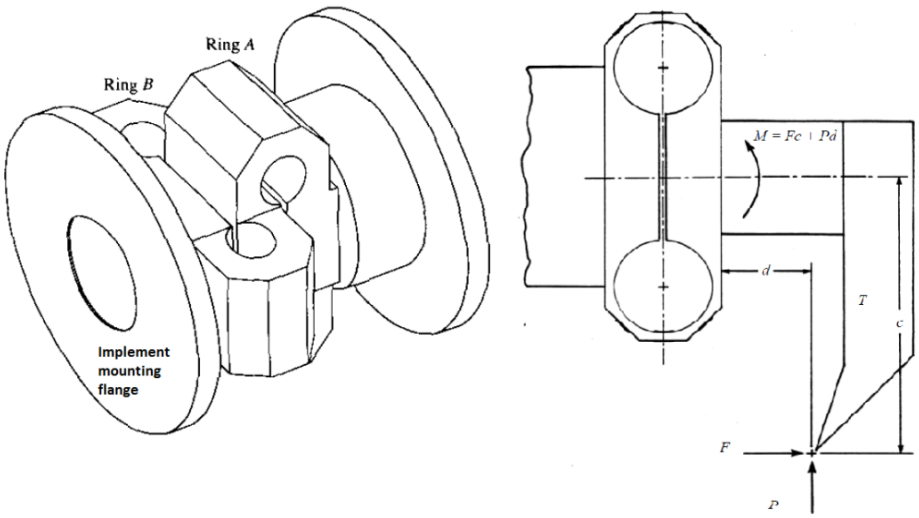

Figure 0.13: A schematic of extended octagonal ring dynamometer attachment on the implement framework [64]

Another approach that can be used for the soil bin purposes is to place instruments (both S-type load cell and Octagonal rings dynamometer) in the interface between the frame and tools which are engaged with soil. This approach removes the complexity of soil-tillage systems of forces which affect the measured forces. This approach is designed by [66] and used an extended octagonal load cell located in the beam as shown in Fig.2.14 and followed by [67] who used an S-type load cell between the shank and the frame.

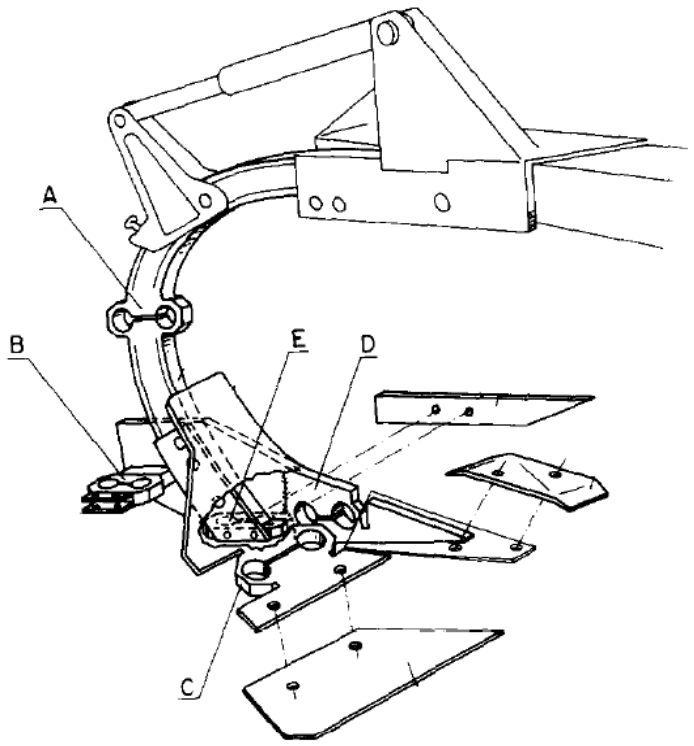

Figure 0.14: A, B, C, D, and E are the extended octagonal ring dynamometers which are located between frame and shank [66]

1.6.3. Instrumented Tillage Tools:

A more recent approach to measure the blade force during soil-tillage interaction is use of instrumented tillage-tools with transducers which are in direct contact with the soil. This method decreases noise signals which affect resultant forces and consequently increases the accuracy. Another feature of these devices is that they were designed to measure horizontal (draft) forces through several sensing elements located at different depths, thus it is possible to determine distribution of the soil resistance during interaction. This can be done in two different arrangements: using strain gauges or using force measuring instruments (load cells and dynamometers). [68] and [69] designed models by using sets of strain gauges mounted on the back side of a blade to measure moments and deformation of the beam caused by the soil during

blade motion. Using several strain gages along and back of the tool allowed [68] to interpret force distribution on the tool and consequently measured the tool's bending moment during soil-tool interaction, as shown in Fig. 2.15. On the other hand [70], [71], and [72] used load cells directly attached to the tools (cutting elements) in the direction of travel. In this arrangement, load cells were located inside a narrow soil-cutting blade and were extended in front of the blade edge, as shown in Fig. 2.16. In addition to its high accuracy, this approach is also used to find soil strength profile (SSP) at multiple depths.

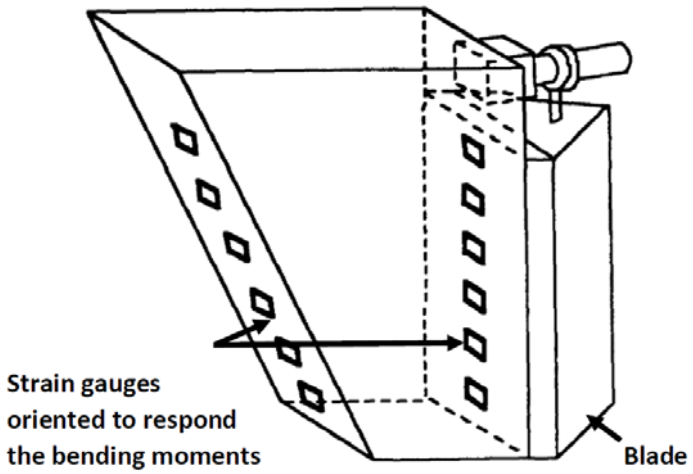

Figure 0.15: A schematic view of the instrumented tool used in [68]

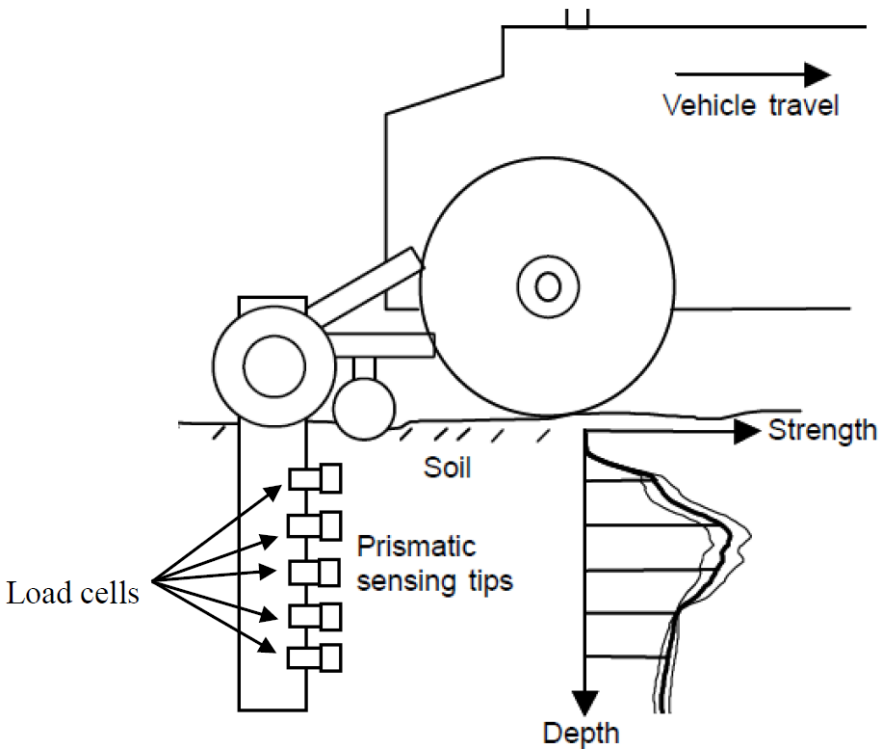

Figure 0.16: load cells located inside a narrow soil-cutting blade [72].

Finite element simulation

In this section, first FE formulation and the plasticity based constitutive law for soil are briefly outlined. Then the FE meshing and handling of the soil-blade interaction is explained. In particular, the procedure of simulating the cutting process (which is continuous) through the soil (described by a discrete FE mesh) is discussed in more details.

1.7. The FE formulation and constitutive law for soil

The strain vector (the vector formed by six components of the strain tensors, as defined in Mechanics of Solids) in an inelastic behavior is composed of:

$$\varepsilon = \varepsilon_{el} + \varepsilon_P, \tag{3.1}$$

where ε, ε_{el}, and ε_P are the total, elastic and plastic strain vectors respectively as indicated in Fig. 3.1.

The stress vector σ is defined as

$$\sigma = D\varepsilon_{el} = D(\varepsilon - \varepsilon_P) \tag{3.2}$$

Where D is the material matrix (E, Young's modulus in 1-D)

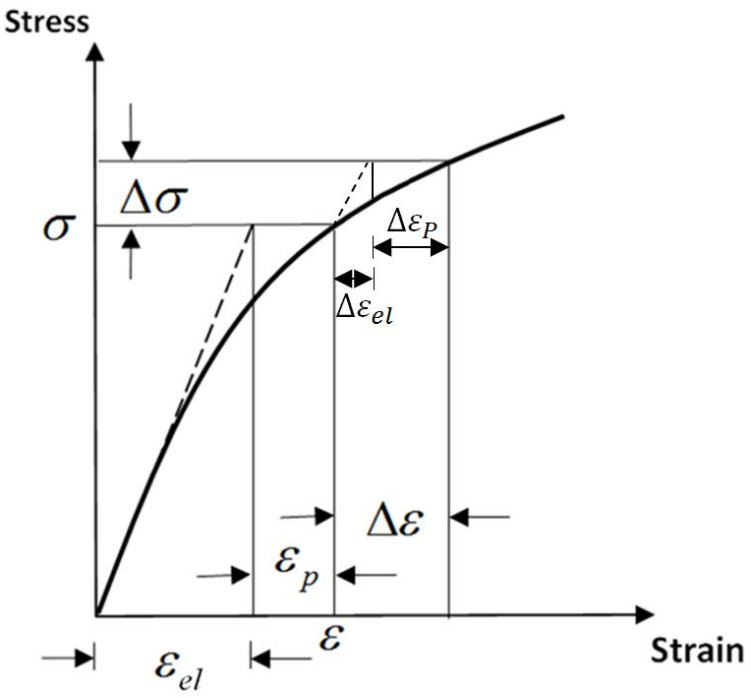

Figure 0.1: Elastic plastic stress-strain relation and iteration pattern

Elastic-plastic response of material is analyzed incrementally in which the following apply

$$\Delta\varepsilon = \Delta\varepsilon_{el} + \Delta\varepsilon_P, \tag{3.3}$$

and

$$\Delta\sigma = D(\Delta\varepsilon - \Delta\varepsilon_P), \tag{3.4}$$

Material plastic behavior is governed by the yielding function, $f(\sigma) \le 0$ (or the yield criterion, the behavior is elastic if $f(\sigma) < 0$ and plastic if $f(\sigma) = 0$) and the plastic flow rule which determine the plastic strain increments by

$$\Delta\varepsilon_P = \Delta\lambda \frac{\partial Q}{\partial\sigma}, \tag{3.5}$$

where $\Delta\lambda$ is a scalar related to magnitude of plastic strain increment and $Q(\sigma)$ is the plastic potential function. Equation (3.5) indicate that vector $\Delta\varepsilon_P$ is normal to the surface $Q(\sigma) = Const.$

In FE the displacement field of element, u, is assumed in the form

$$u_e = N \cdot q_e, \tag{3.6}$$

where N is matrix of the element's shape function and q_e is the corresponding vector of degrees of freedom (for the elements used in this thesis q_e are the nodal displacements).

Then the virtual incremental displacement will be

$$\delta u_e = N \cdot \delta q_e \tag{3.7}$$

The strain of element is related to the nodal displacement by this formula

$$\varepsilon = B \cdot q_e, \tag{3.8}$$

where B is the strain-displacement matrix for the element.

Then the virtual incremental strain is derived as

$$\delta\varepsilon = B \cdot \delta q_e \tag{3.9}$$

The basic formulas of FE can be derived by applying the principal of virtual work which states that the virtual (incremental) change of total internal work (strain energy) δU is equal to change of work of external force δW i.e.:

$$\delta U = \delta W, \tag{3.10}$$

The internal work δU is defined as

$$\delta U = \int_{V_e} \delta\varepsilon^T \sigma dV, \tag{3.11}$$

where V_e is the volume of the element. By applying Eq. (3.2) in (3.11), the strain energy is derived as

$$\delta U = \delta q_e^T \int_{V_e} B^T D(Bq_e - \varepsilon_P)dV = \delta q_e^T \left[\left(\int_{V_e} B^T DBdV \right) q_e - \int_V B^T D\varepsilon_P dV \right] = \delta q_e^T \left[K_e q_e - F_e^P \right] \tag{3.12}$$

where K_e is the element stiffness matrix specified as

$$K_e = \int_{V_e} B^T DBdV \tag{3.13}$$

and F_e^p is the fictitious plastic force defined as

$$F_e^p = \int_{V_e} B^T D\varepsilon_p dV \tag{3.14}$$

Note that as a result of inelastic strains, both K_e and F_e^P become dependent on vector q_e.

On the other hand the virtual work of external force F_e can be written in the form

$$\delta W = \delta q_e^T \cdot F_e, \tag{3.15}$$

where F_e is the vector of external forces applied to the element. By combining Eqs. (3.10), (3.12) and (3.15), one arrives at:

$$\delta q_e^T (K_e \cdot q_e - F_e^P - F_e) = 0, \tag{3.16}$$

For arbitrary virtual increments δq_e^T the following is true

$$K_e(q_e) \cdot q_e - F_e^P(q_e) = F_e \tag{3.17}$$

Where notations $K_e(q_e)$ and $F_e^P(q_e)$ are used to indicate that matrix K_e and vector F_e^P are both dependent on vector q_e.

Eq. (3.17) is referred to as the element equilibrium equation. Assembling all the elements equilibrium equations for the whole model results in

$$K(q) \cdot q - F^P(q) = F \tag{3.18}$$

where $K(q)$ and F^P represent the stiffness material and vector of plastic force for the whole model (q and F are vectors of DOFs and nodal forces respectively). Clearly these equations are nonlinear with respect to q.

Equations (3.18) are solved iteratively for each incremental step which symbolically can be represented by

$$q_{k+1} = K^{-1}(q_k)(F + F^P(q_k)), \qquad k = 0,1,2,... \tag{3.19}$$

Where q_0 is known from the previous step and the iterations (referred to as equilibrium iteration) are repeated until

$$\left\| q_{k+1} - q_k \right\| < C_P \tag{3.20}$$

at the end of the current step, where C_P is the convergence parameter.

In the FEA software ANSYS a more sophisticated Newton-Raphson iteration procedure (details can be found in [73]) was used.

If the plastic potential is the same as the yield function, then the plastic flow rule is called associated, with the increments of plastic strains normal to the yield surface. Otherwise, the flow rule is called non-associated with the direction of increments of plastic strains normal to the surface representing the plastic potential, but not to the yield function.

The Drucker-Prager yield function (also referred to as extended/modified Drucker-Prager criteria, for example in [23]) is pressure dependent, which makes it applicable for geotechnical materials. This function can be expressed as follows:

$$f(\sigma) = \beta_c I_1 + \sqrt{J_2} - k = 0 \tag{3.21}$$

Where k and β_c are material constants, and I_1 is the first invariant of the stress tensor (also $I_1 = 3\sigma_m$, where σ_m is mean or hydrostatic pressure) while J_2 is the second invariant of the stress deviator tensor defined using the principal stresses $(\sigma_1, \sigma_2, \sigma_3)$ defined by:

$$I_1 = \sigma_1 + \sigma_2 + \sigma_3 \tag{3.22}$$

$$J_2 = \frac{1}{6}\left[(\sigma_1 - \sigma_2)^2 + (\sigma_1 - \sigma_3)^2 + (\sigma_3 - \sigma_2)^2\right] \tag{3.23}$$

For soil the constants k and β are specified in terms of c and ϕ, the soil cohesion and the angle of internal friction respectively, as:

$$k = \frac{6c\cos\phi}{\sqrt{3}(3 - \sin\phi)} \tag{3.24}$$

$$\beta = \frac{2\sin\phi}{\sqrt{3}(3-\sin\phi)} \tag{3.25}$$

The values of c and ϕ can be determined from triaxial test, in which the maximum shear stress τ' in the presence of normal stress σ' is recorded and graphed as sketched in Fig. 3.2. The stresses τ' and σ', which are shown in the insert, are often related to the minimum and maximum principal stresses (σ_1 and σ_3 respectively) via 2D stress transformations. In our case these stresses will typically be in the plane of the blade's motion. The limit values of τ' and σ', which are usually related linearly, can be interpreted as $\sqrt{J_2}$ and $-I_1$ respectively. The direction of inelastic sliding θ is dependent on the internal friction through the relationship $\theta \approx 45^\circ - \phi/2$. It should be noticed that the thick-solid line represents the yield criterion (3.21) for the mean stress in compression.

In this research, the soil- blade interaction is modeled by the Drucker-Prager criteria with a non-associate flow rule. The numerical procedure available in FE software allows the use of the same functions for the plastic flow rule and for the yield surface, i.e. $Q(\sigma) = f(\sigma)$ and then rotate the vector $\Delta\varepsilon_p$ by the angle ν as indicated in Fig. 3.2. The angle ν represents the volumetric expansion and frictional-dilatancy behavior of the material (therefore it is also referred to as the dilatancy angle).

For the flow rule associated with criterion (3.21) the increments of plastic strains would have direction 1 that contains shear deformation and dilatations characterized by the dilatancy angle $\nu = \phi$. On the other hand, if there is no volumetric expansion, then $\nu = 0$ (shear type of deformation only), which corresponds the direction 3 (vertical) of the increments of plastic strain. According to [19] for real soil value of dilatancy angle ν is usually less than ϕ and

should be within the limits $0 < \nu < \phi$ as indicated by direction 2 (the values of parameters used in the paper are listed in Table 3.1).

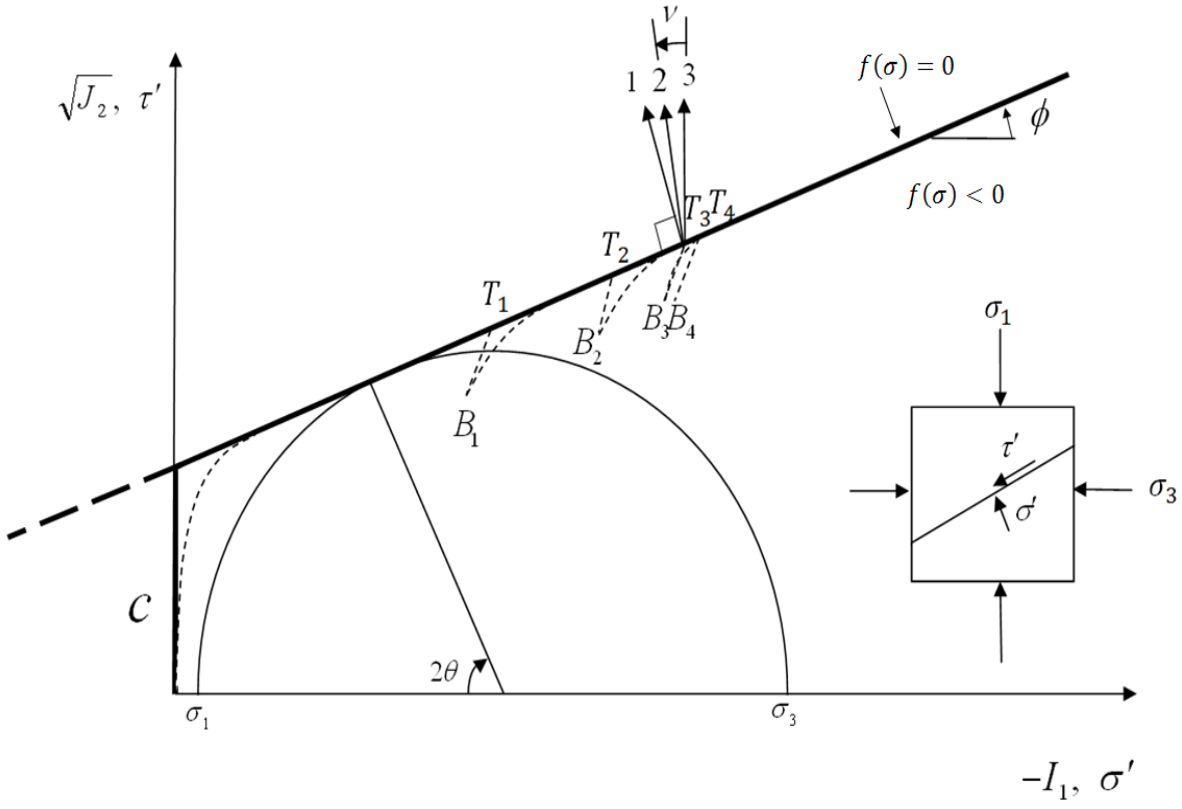

Figure 0.2: The Drucker-Prager material law with non-associated flow rule.

In the FE standard analysis, the material body analyzed is assumed as a continuum. However in the soil-tool interaction the soil besides being compressed by the motion of the tool (see in Fig. 3.3) is sliding on the tool interfaces, and is separated by the lower tip of the tool. In particular, modeling of the separation is a challenge (the sliding is modeled with the help of contact elements). In order to overcome this challenge, separation surfaces are actually modeled by two surfaces connected via the contact elements (and initially the nodes belonging to these two surfaces coincide). Such a configuration is indicated in Fig 3.3 (this picture is not to scale and only the line representing the horizontal separation surface is shown). Any relative soil motion

takes place on these surfaces during the soil-blade interaction. By entering the tool through the soil, these contact elements are turned off on correlated nodes and consequently the separation between soil elements is modeled.

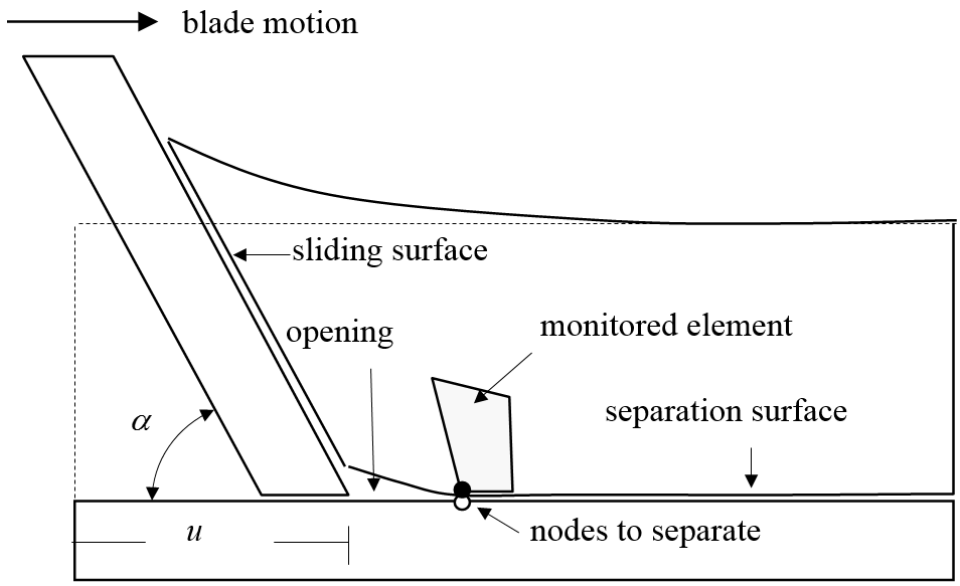

Figure 0.3: Details of modeling the blade-soil interaction

It should be noted that the yield criterion is not related to separation, which should be defined independently (but the stresses must be on the yield surface for the separation to happen). Since the separation status in FE analysis can only be defined at nodes, the simulated separation process is 'discrete' in the sense that there would be some stress relief when the status at a particular node is changed from initially connected to separated. For example if just before the first separation the stress state is defined by T_1 then just after separation it will be lowered and back to elastic region (see Fig. 3-2). In this region the highest stress state, defined by B_1, will be typically at the opening's tip, i.e. at the node to be separated next. Then after a further load increase (controlled here by the forced blade's displacement) the stress state is observed at the node that would separated next. This stress state must first reach the yield surface again and then

follow it until arriving at point T_2 where the separation criterion is met again. After separating at the subsequent node the stress state drops to B_2, and so on (points B_1, B_2.. are further interpreted and discussed in sections 3.2.2 and 3.2.3 and shown in Fig. 3.6 and Fig 3.7). Therefore in our FE analysis the constitutive law for soil being cut is represented by a line coinciding with the yield line but with elastic 'incisions' inwards (such as T_1B_1 in Fig.3.2) representing separation at the consecutive nodal point. More details of the separation procedure are explained in the next section after the geometry of the FE model.

In the numerical analysis for such a soil model with the external load increasing, a typical material behavior defined by this constitutive law is plotted with dotted curve in Fig.3.2. It starts with elastic deformations until the yield criterion is reached and then the curve lines up with the yield surface (points T_i are on this surface). Plastic deformations generated along the yield surface may be considered as compacting.

The properties of soil, as given by [24] and also used in this study, are listed in Table 3.1. The elastic–plastic behavior of soil is defined by the cohesion, internal friction angle, dilatancy angle, modulus of elasticity, specific weight, and Poisson’s ratio.

Table 0.1: Soil and blade parameters that are used in the present analysis.

Properties	Soil
c- Cohesion	$20\ KPa$
ϕ - Soil internal friction angle	35°
ν - Dilatancy angle	20°
E - Modulus of elasticity	$5\ MPa$
μ - Poisson's ratio	0.36
ρ - Density	$1220\ kg/m^3$

1.8. Soil-tool interaction including separation

1.8.1. Tow-Dimensional (2-D) FE modeling

In order to explain the soil separation in detail, this description is illustrated with the simplest model. The so-called wide blades (with width about 10 times greater than the cutting height) can be represented by 2-D models that obviously are much more numerically efficient and easier to interpret as shown in Fig.3.4. In such models quadrilateral PLANE42 elements from the ANSYS [23] library of elements, have 4 nodes and 2 degree of freedoms (DOF) at each node with the plane strain option. As mentioned in the previous section during soil-blade interaction, soil is sliding on the blade interface besides being compressed by the motion of the blade, and is separated by the lower tip of the blade between soil particles which are shown in the Fig.3.4 as L_v and L_h respectively.

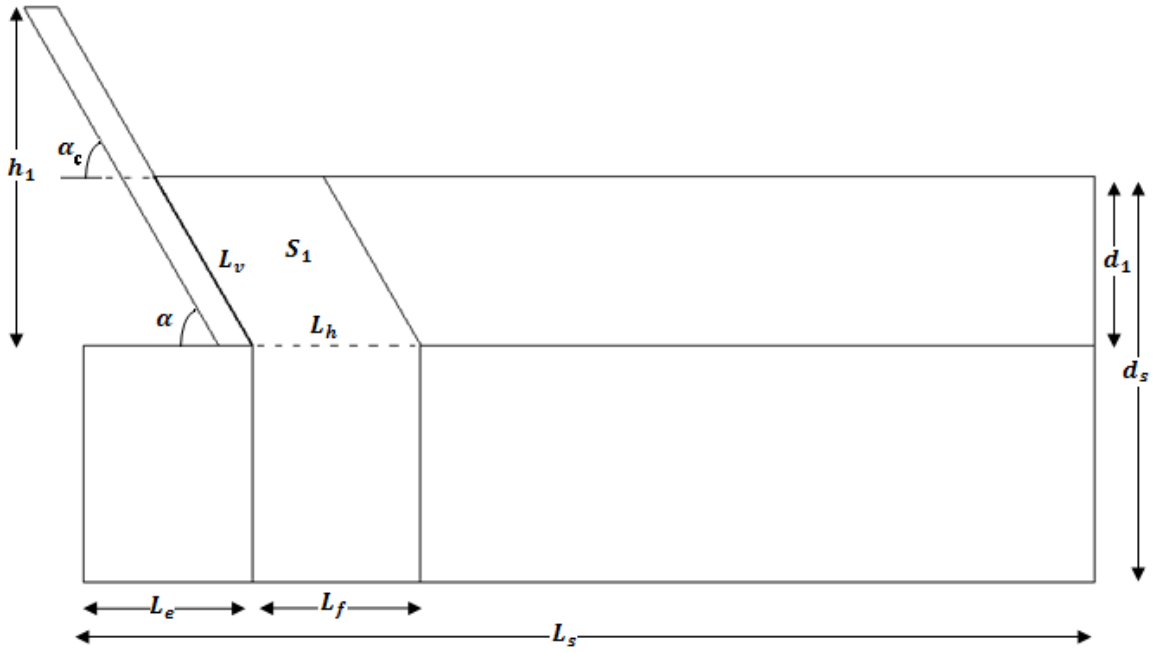

Figure 0.4: 2D soil-tool model for wide blade; L_v is contact surface between blade-soil, L_h is separation surface between soil particles.

In order to model the sliding and the separating, 2D surface-surface contact element, CONTA171 and TARGET169 elements were used. However for soil-blade sliding these contact elements with sliding options are used along L_v, but for the modeling soil-soil separation these elements with bonding options are used along L_h. The separation process is similar to the process of cutting chips in machining operations [20-22] or to the crack propagation process, i.e. there is always a small crack moving in front of the blade that allows the blade to travel through the soil (such a crack can be observed on the deformation pattern shown in Fig. 3.8). The nodes on the separation surface can move apart if a specified separation criterion is met. The distance u traveled by the blade's tip is measured from L_e, and its maximum value is L_f.

A 2D typical meshing pattern is indicated in Fig.3.5 and boundary conditions of the model can be listed as follows:

1. Bottom nodes, at Y=0, are fixed.

2. Nodes on vertical boundaries X=0 and X= L_s are fixed.

3. The blade is fixed in Y direction in order to limit blade motion in the X direction.

The meshing shown in Fig. 3.5 (which can be considered typical) uses a total number of 408 quadrilateral elements and 36 contact elements

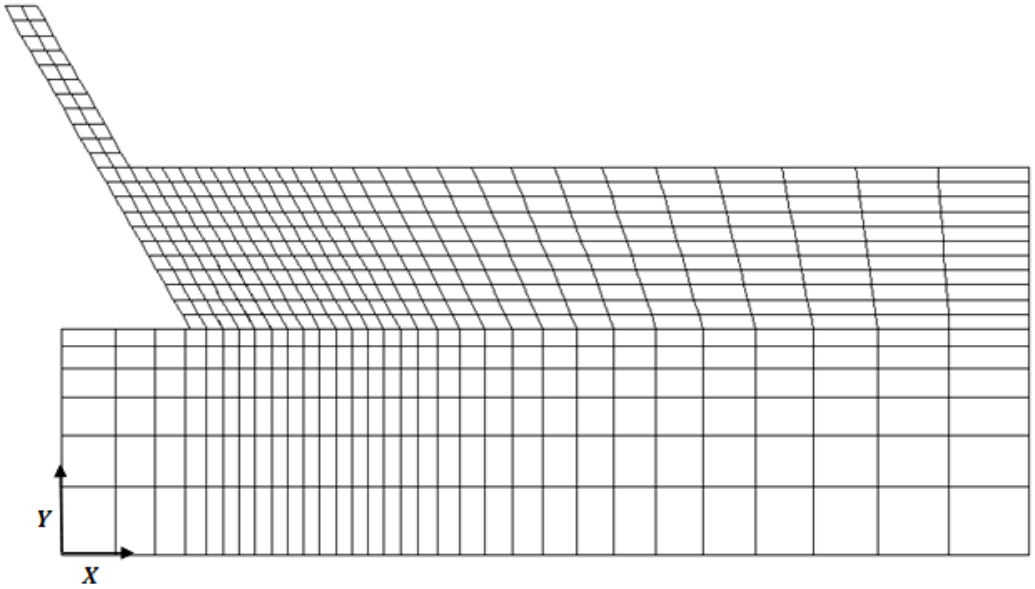

Figure 0.5: Finite element mesh for a typical 3D soil-tool interaction model

1.8.2. General solution procedure

As mentioned in sec. 3.1, an iteration procedure starts with the prior step results to update the equation (3.18) and resolve it again by applying the Newton-Raphson method.

Based on elastic-plastic material type and employing contact elements in this study, we are dealing with material and contact nonlinearities, which make equilibrium iteration harder to converge.

In the present study based on the motion of blade, the increments of u are assumed in steps (representing the 'load' steps in FE software that define the load history) in order to represent all the evaluation sets at the end of each step. The values of such steps are quite important from the numerical viewpoint since too small steps may result in a substantial increase of the time of calculations and large steps may result in divergence of the nonlinear solution. In this study, the length of each load step is fixed manually to balance calculation time and result convergence which are larger between the separation instances (approximately one tenth of element size) and smaller around the separation (around one twentieth of element size). After each load step, results are observed to check if they reach the separation criterion. This criterion is discussed in the next section.

A solution within a load step is acquired by applying the load incrementally (signifying the 'Sub' steps in FE software). Within each sub step, the program carries out several equilibrium iterations to achieve a converged solution. Based on the balance between the calculation time and the result convergence, FE software sets the number of sub steps of each load step in the automatic time stepping algorithm.

1.8.3. The separation criterion

The elements above and below the expected separation surface are connected at nodes using the contact elements that allow to activate or deactivate the bonding forces between them. The highest stress/deformation level is observed always in the element which is at the tip of the

opening and it is of a particular interest during the whole simulation. At the beginning all bonding forces are active and this element (to be referred as to the tip element) is adjacent to the tip of blade. As the blade starts to move the stresses go through the elastic phase (see the broken line in Fig. 3.2) until the solid line representing the yielding condition Eq.(3.21) is reached (where the Drucker-Prager plasticity rules are followed). In the tip element the strain component ε_x (in the direction of the blade's motion) is monitored continuously. The elasto-plastic process will continue until ε_x reaches a predefined magnitude of ε_c (which may be referred to as the limiting compacting strain) with the stress state reaching point T_1 in Fig. 3.2. At this instant the force bonding the nodes at the opening's tip (of the tip element) is deactivated, and the separated nodes generate the first opening of length equal to the size of the element's side. This is also associated with the stresses being relieved to the state denoted by point B_1, which will again be inside the elastic range (i.e. inside the surface defined by the yielding condition), and a drop in the value of ε_x below ε_c. With the blade moving forward the stress state will be increasing to reach the yielding condition again but at the new tip of opening that is now away from the blade's tip. The strain ε_x will become equal to ε_c at T_2 and the node separate at this tip increasing the opening's length by the size of element and causing the stress (and strain) relieve indicated by point B_2, and so on.

As discussed in the next sections, the numerical experimentations indicate that if $\varepsilon_c \approx 0.3$ then the resultant draft force was best matching the results obtained from the 'engineering' formulas presented in [7-8], and often used by the designers of tools for tillage operations.

Since the continuous process of cutting the soil is modeled 'discretely' (by disjoining consecutive nodes on the separation surface), the local stiffness in the vicinity of the opening's tip changes abruptly with the system appearing to be slightly stiffer before the separation and slightly softer after. Such effects will be taken into account in the next section that presents the method of calculating the draft force required to move the blade through soil.

The separation procedure also affects how the stress state in soil follows the Drucker-Prager criterion Eq.(3.21), which in the σ_1, σ_3 coordinates (i.e. in $\sigma_{\min}, \sigma_{\max}$ respectively and assuming σ_2 as at the instant of separation) can be represented by ellipsoidal yielding curves growing or shrinking dependently on the magnitude of the current pressure. Such curves for soil are significantly affected by the internal friction ϕ, and generally shift towards compressive stress components.

For the case of the rake angle $\alpha = 60^\circ$, and for the tip element at the nodes about to be separated (i.e. corresponding to points T_1, T_2, T_3, T_4 in Fig. 3.2) such curves are plotted in Fig. 3.6a. Only a relatively small portion of the curves in the location A-A which is redrawn in Fig. 3.6b was used in this case. For comparison the curve for $\phi = 0$ (independent of the pressure and intersecting the σ_1, σ_3 coordinates at $\pm 2c$) is also indicated. The figure shows some details of the stress state history for particular material points due to a continuous quasi-static motion of the blade.

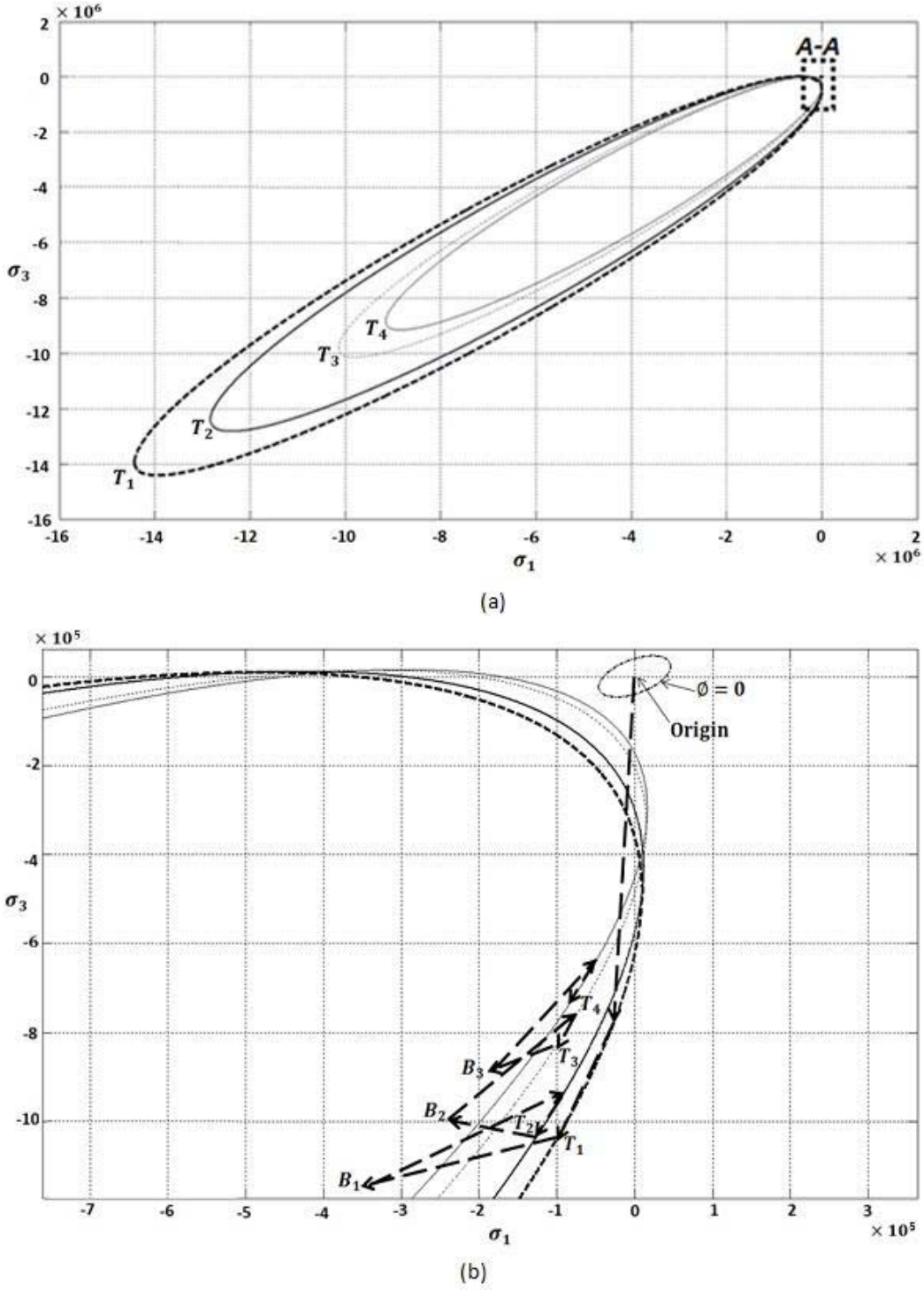

Figure 0.6: (a) The soil yielding function for the Drucker-Prager criterion at various stages of the cutting process. (b) Details of the stress state at different phases of the separation procedure.

For the point that initially is at the blade's tip, the history starts at B_0 (no stress) and ends at T_1 (just before the first separation). Then for the next point to separate, the history starts at B_1 (just after the first separation) and ends at T_2 (just before the second separation, and so on).

It should be noted that the curves for the states T_i are in general relatively close to each other (especially in the range shown in Fig. 3.6b), and are getting closer with consecutive separations. Such curves essentially coincide after about the fifth separation indicating that the simulation of the cutting process stabilizes, i.e. it becomes independent of the preliminary phase that starts from the unloaded state (this will be used in calculating the draft force from the plots as discussed in Fig. 3.7).

From the numerical point of view, the simulation with such stress histories demands a larger number of equilibrium iterations (we used the standard updated Newton-Raphson method) and a very careful monitoring of the convergence at each load step.

1.8.4. Calculating forces on the blade

As already mentioned the analysis is quasi-static, the stress-strain states in the whole FE model is calculated for increasing horizontal distance traveled by the blade (denoted by u in Fig. 3.3). The forces (draft and lift) acting on the blade are determined by properly integrating the stress components. As mentioned before, the size of each subsequent step can be estimated from the ε_x readings of the previous step. If ε_x is near ε_c, the step size is decreased to approach the separation criterion smoothly.

For an assumed mesh size a typical calculated draft force depends on the distance traveled as plotted in Fig. 3.7. The calculations start as elastic (*OE* range) with all the bonding forces active

(and therefore all the soil elements still connected), enter the plastic deformation at some point *E*, and then go to inelastic phase until deformation in the vicinity of the tip of the blade (point *A*) measured as ε_x, reaches the value ε_c. This happens when the blade's displacement and the corresponding draft force reaches the level defined by point T_1.

Then the bonding force in the first node is deactivated (or the elements above and below the separation plane closest to the blade are allowed to separate) which brings about a drop in the magnitude of the draft force to the value corresponding to point B_1.

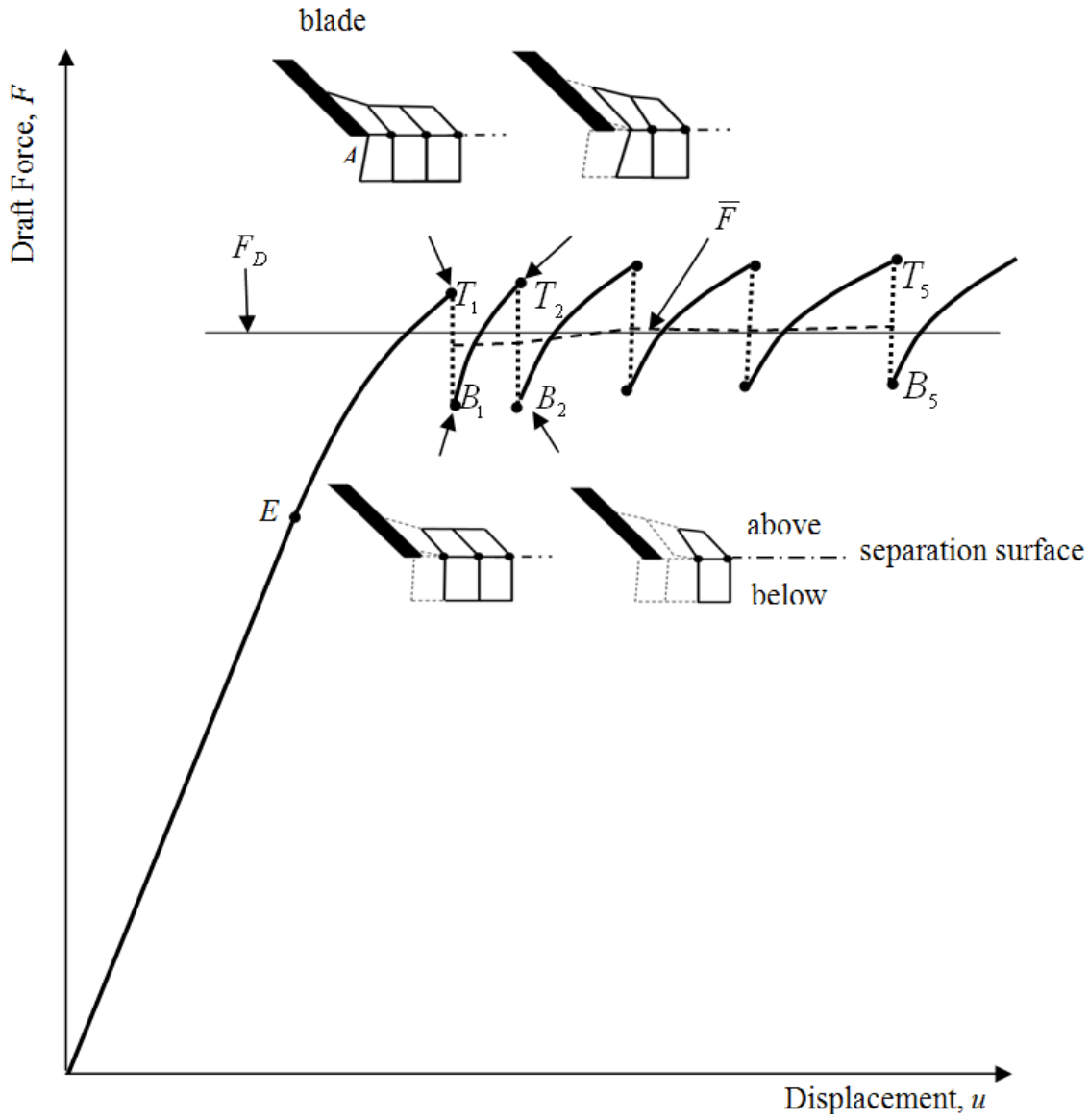

Figure 0.7: The force developed on the blade using the first six elements in front of the blade

The opening equal to the element size along the separation surface is created and the stresses and deformation in its vicinity are reduced enough (see the explanations in the previous section) for the analysis to start at B_1 from an elastic level. First the yielding condition is reached, and next ε_x increases to ε_c, which takes place at the blade's displacement and the draft force is denoted by point T_2. Deactivating the bonding force in the second node brings the draft force to the level

indicated by point B_2 (in the elastic range), and so on. The elements separated in the first and second deactivations are indicated with the broken lines.

The plot in Fig. 3.7 represents a typical relationship for the draft force vs. the blade's displacement covering five separations (i.e. the cutting/opening runs through five elements) as obtained from the simulation.

Some details of the meshing and opening after three separations are shown in Fig. 3.8. One can note in the enlarged picture that the elements above the separation line have shrunk about 30% in the horizontal direction, which is the consequence of assuming ε_c=0.3.

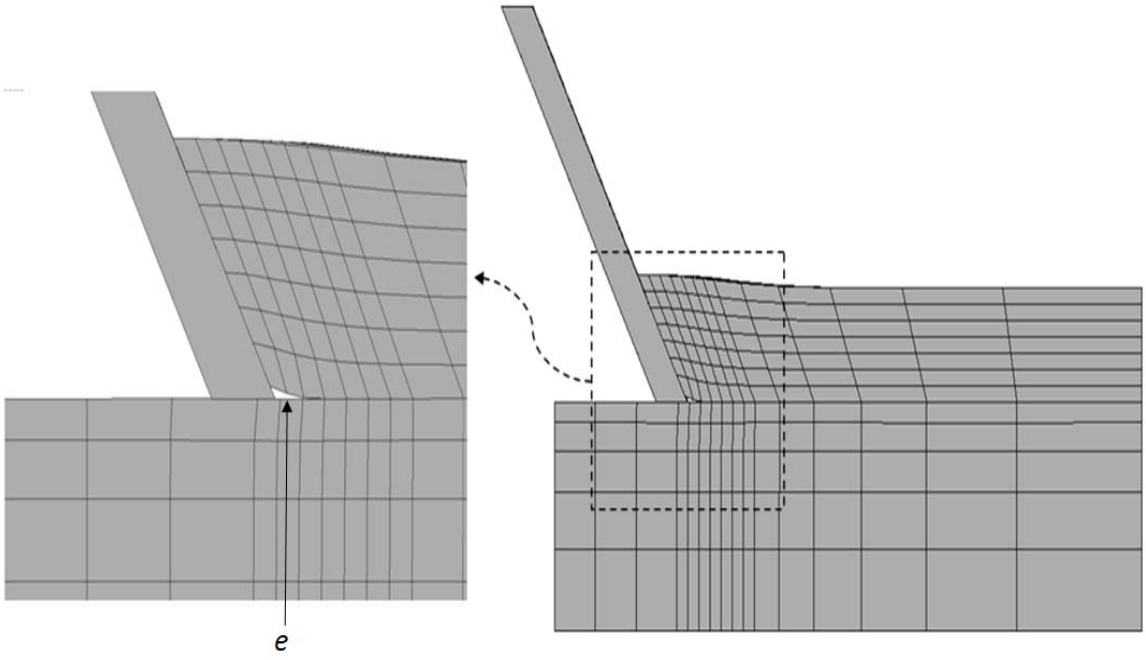

Figure 0.8: The soil deformation after three separations (note the opening in front of the blade's tip).

The separation simulated by the FE model takes place sequentially at the nodes on the separation surfaces, as already discussed. When the bonding force at a particular node is deactivated the

system suddenly changes its overall stiffness resulting in the draft force drop indicated by a jump $T_i - B_i$. It should be noted that the 'discrete' modeling of the separation force $F(T_i)$ is calculated for an underestimated length of the opening in front of the blade and for an overestimated bonding force in the node to separate. Similarly, force $F(B_i)$ is calculated for an overestimated length of the opening and for an underestimate bonding force at the same node. Also, the elements in configuration T_i are connected by one node more than in configuration B_i (at the same distance *u*). Therefore one may interpret $F(T_i)$ as an upper limit of the draft force calculated continuously, while $F(B_i)$ as a lower limit of that force.

How much the draft force is over- and underestimated (or the difference $F(T_i) - F(B_i)$) depends on the element size *e* on the separation plane (see Fig. 3.8). However, as our numerical experimentations indicate (to be presented in the next section), the average force $\overline{F} = \left[(F(T_i) + F(B_i)\right]/2$ for *e* small enough appears to be essentially independent of meshing. Therefore it can be considered as an approximation of the draft force for the blade's displacement *u* at the instant of a particular separation. This force is plotted as a broken line in Fig. 3.6; note that it becomes almost constant even after one or two separations. Such a force is denoted by F_D, and it represents the draft force characterizing the soil-tool interaction for particular conditions assumed in the simulation.

Since the shape of nonlinear portions $E - T_1$ and then $B_i - T_{i+1}$ of the draft force-displacement are of less importance, the plots in the next sections will be simplified to show only points T_i and B_i (to demonstrate how they are getting closer with smaller *e*), and then the plot of $\overline{F}$ and the value of F_D.

1.9. Three-Dimensional (3-D) FE modeling

In the FE general 3D model both soil and blade are represented by the hexahedral elements SOLID45 from the ANSYS [23] library of elements, which has 8 nodes and 3 degrees of freedom (DOF) at each node as shown in Fig.3.9 (translations in the nodal x, y, and z directions). The soil-blade sliding is modeled by the 3-D surface to surface contact elements CONTACT173 and TARGET170 with sliding option placed along the intersection of soil and blade surfaces. The same contact elements were used with both bonding and sliding options for simulating separation surfaces. The model with the elasto-plastic constitutive law, the separation procedure, and with elastic incisions (see Fig. 3.2) require a relatively large number of equilibrium iterations for convergence, thus the calculations are generally long (typically lasting several hours). Therefore a number of meshing patterns with higher density near the contact areas were tried for balancing the computational effort with accuracy of calculations. The effects of the elements' sizes on accuracy and convergence are discussed in the section presenting the results. In general only the models that can be considered converged are shown in this study.

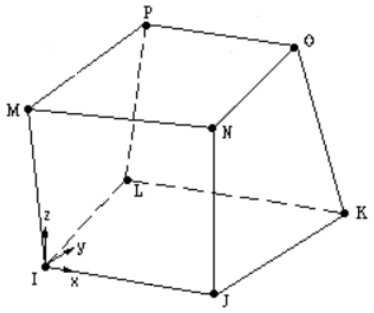

Figure 0.9: Hexahedral SOLID45 element which has 8 nodes and 3 translational degree of freedoms in x, y, and z directions at each node [23]

1.9.1. FE model, geometry and boundary conditions

1.9.1.1. Straight Rectangular blade

After illustrating the separation procedure by the 2-D FE model, this section is continued by simulation of interaction between soil and narrow blades or 3-D soil-blade interaction. Geometry of the 3D straight rectangular model is sketched in Fig. 3.10. The model is parametric with several parameters defining the geometry of soil and tool. The soil block is L_s = 300mm long, w_s = 300mm wide, and d_s = 150mm deep. These dimensions were selected in such a way that the solution in the vicinity of the blade is not sensitive to the block's size. The block is divided into sub-blocks that can be meshed with different mesh densities. The maximum distance blade can travel while cutting the soil, also the length of contacts between upper and lower blocks of soil, is L_f = 50mm. Parameter w_1 is the width of cut soil (also the width of blade), w_2 is the side widths of soil block (and $w_1 + 2w_2 = w_s$). The depth of cut soil is d_1; which is also the cutting depth of blade. Tilting of the blade with respect to the soil is defined by α, the rake angle.

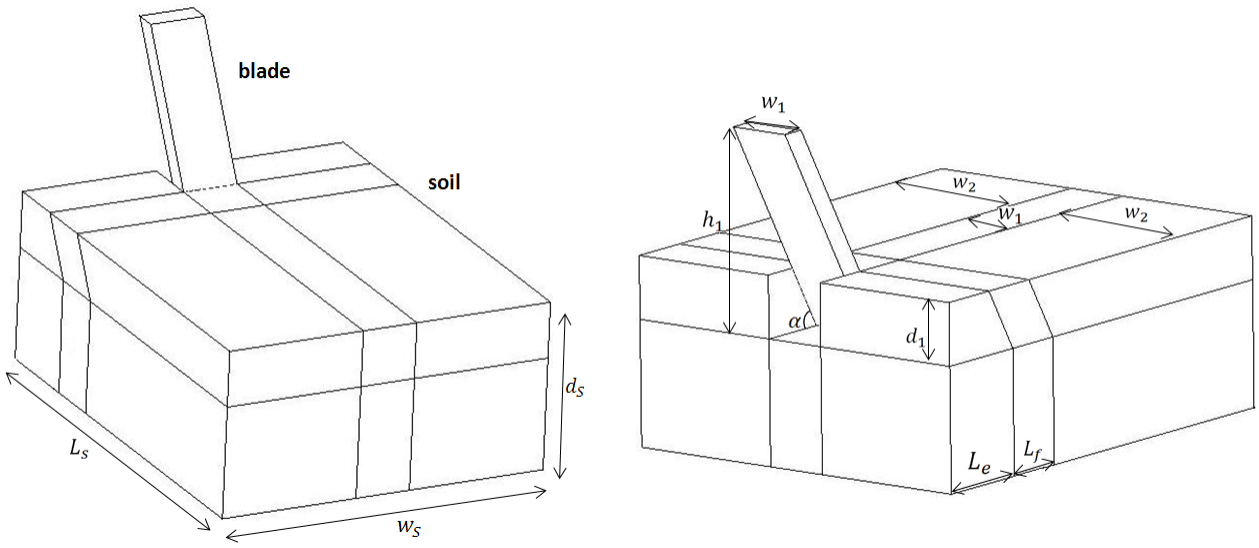

Figure 0.10: 3D soil-tool model dimensions for narrow blade

The starting point of the blade's travel inside the soil block is denoted by $L_e = 50\text{mm} + d_1 \cos\alpha$. The blade's total height is $h_1 = 100\text{mm}$, this parameter does not affect the cutting process. The ranges of $d_1 = 25\text{-}50\text{mm}$, $w_1 = 20\text{-}160\text{mm}$, and $\alpha = 30\text{-}90^\circ$ were examined.

A typical meshing pattern is indicated in Fig.3.11. Boundary conditions for such a model are as follows:

1. Bottom nodes, at $Y = 0$, are fixed.

2. Nodes on vertical boundaries parallel to the *Y*–*X* plane, at $Z = 0$ and $Z = -(2w_2 + w_1)$, are fixed.

3. Nodes on vertical boundaries parallel to the *Y*–*Z* plane, at $X = 0$ except cutting soil area are fixed.

4. Nodes on vertical boundaries parallel to the *Y*–*Z* plane and $X = L_s$ are fixed.

5. The blade is fixed in Y and Z directions in order to limit blade motion in the X direction.

The meshing shown in Fig. 3.11 (which can be considered typical) uses a total number of 3548 hexagonal elements and 392 contact elements. For comparison, the corresponding 2D model uses 408 quadrilateral elements and 36 contact elements.

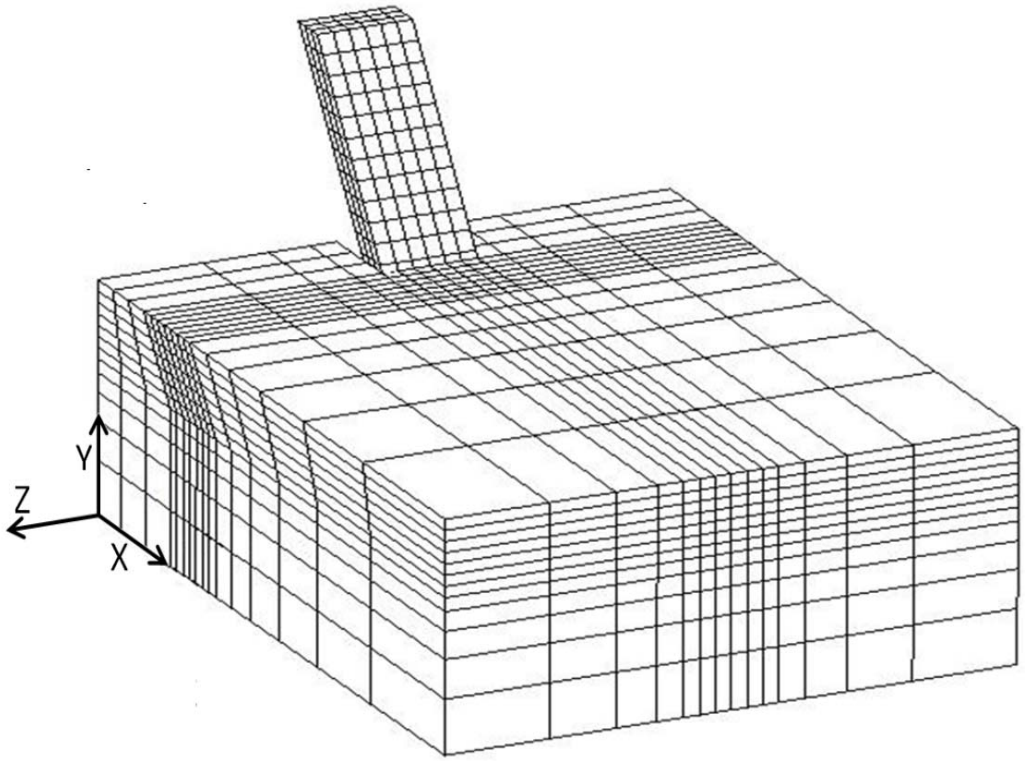

Figure 0.11: Finite element mesh for a typical 3D soil-tool interaction model

As mentioned in the previous section, the separation surfaces between soil-soil surfaces are predefined to simulate separation and motion of soil particles after interaction with blade. However in 2-D soil-blade interaction only one separation line was predefined, in 3-D interaction of soil with a rectangular blade three separation surfaces have to be predefined. As shown in Fig. 3.12, the soil is in contact with the blade on four surfaces. The soil separation takes place along surfaces 1 and 3 (the vertical cuts) and along surface 2 (the horizontal cut). These surfaces will

be referred to as the separation surfaces, and the contact elements with bonding and sliding options are used to model these connections. On surface 4, however, the soil should be allowed to slide along the blade without separation, therefore the contact elements with only the sliding option should be used there. This surface will be referred to as the sliding surface.

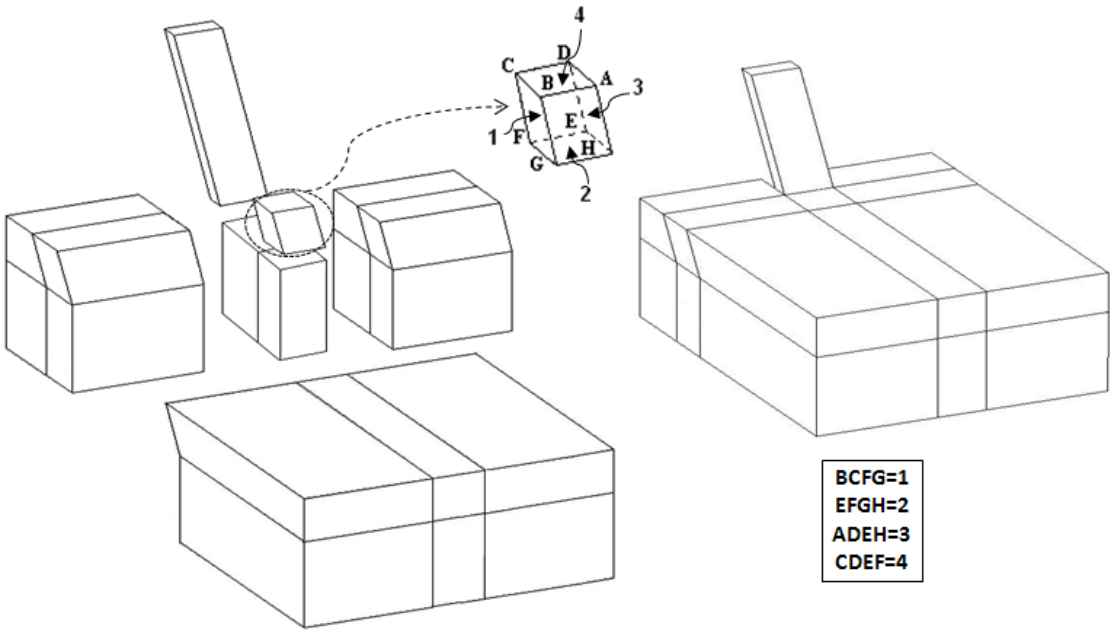

Figure 0.12: The surfaces with contact elements (bonding and sliding on surfaces 1, 2, 3, sliding on surface 4).

It should be noted that the separation surfaces are parallel to the direction of the blade's motion, while the sliding surface is parallel to the front of the blade.

1.9.1.2. Curved Rectangular blade

The second 3-D FE model is interaction between soil and curved rectangular blade. Geometry of this FE model is sketched in Fig. 3.13. The geometrical parameters L_s, w_s, d_s and h_1 are the same as first FE model. The start point of blade's travel inside the soil block is denoted by L_e =

115mm and L_f = 50mm is maximum distance blade can travel while cutting the soil (also length of contacts between upper and lower blocks of soil). The cutting portion of the blade is defined by three parameters α, α_c and d_1, where α is the angle of the blade's tip (the rake angle), and α_c is the angle of blade at the soil surface. The other parameters shown in Fig.3.14, such as α_{avg}, the average slope, β, the arc angle, and *R*, the blade's radius of curvature can be calculated from:

$$\alpha_{avg} = \frac{\alpha_c + \alpha}{2}, \qquad \beta = \alpha_c - \alpha, \qquad R = \frac{d_1}{\cos\alpha - \cos\alpha_c} \tag{3.27}$$

Table 3.2 lists the values of the above parameters used in first phase of the study. In the results section, the effects of the angles α, and α_c on the force acting on the blade are examined (which through (3.27) can be interpreted as the effect of blade's curvature).

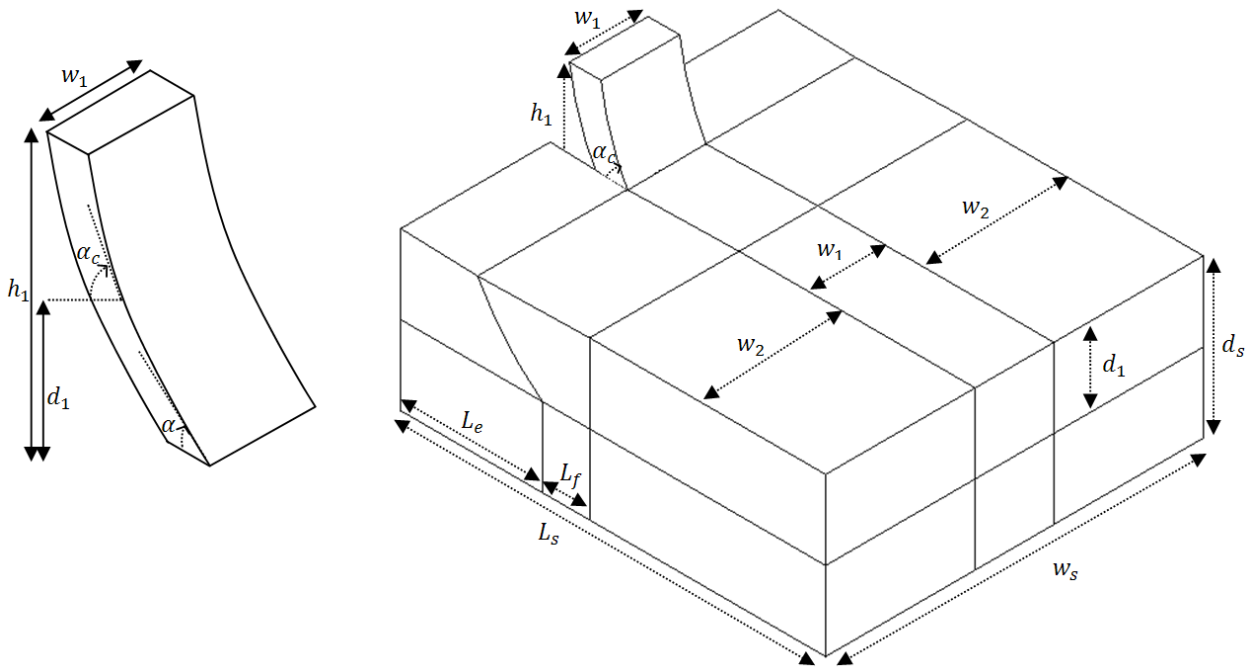

Figure 0.13: 3D soil-tool model dimensions for narrow blade

Table 0.2: Soil-tool model dimensions that used in first model analysis

$w_1(mm)$	$d_1(mm)$	$L_f(mm)$
50	50	50
$L_e(mm)$	$\alpha(^\circ)$	$\alpha_c(^\circ)$
115	60-75-90	35, 45, 60, 75, 90

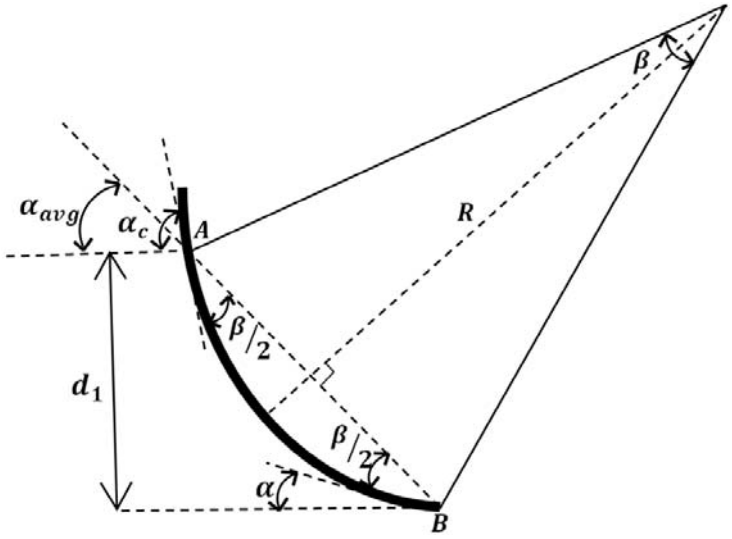

Figure 0.14: Parameters characterizing a curved blade

A typical meshing pattern is indicated in Fig.3.15 and boundary conditions of the model are the same as first FE model

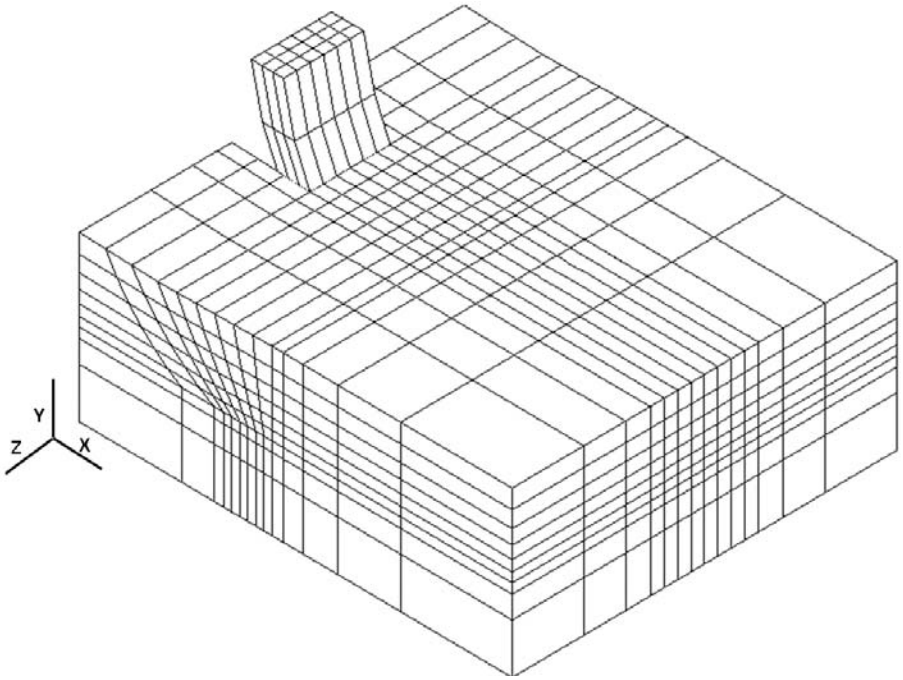

Figure 0.15: Finite element mesh for a typical 3D soil-tool interaction model

The same as first FE model, the FE model for interaction between soil and curved rectangular blade has three predefined separation surfaces (two vertical cuts and one horizontal cut) parallel to the direction of the blade's motion and one sliding surface which is parallel to the front of blade as shown in Fig. 3.16.

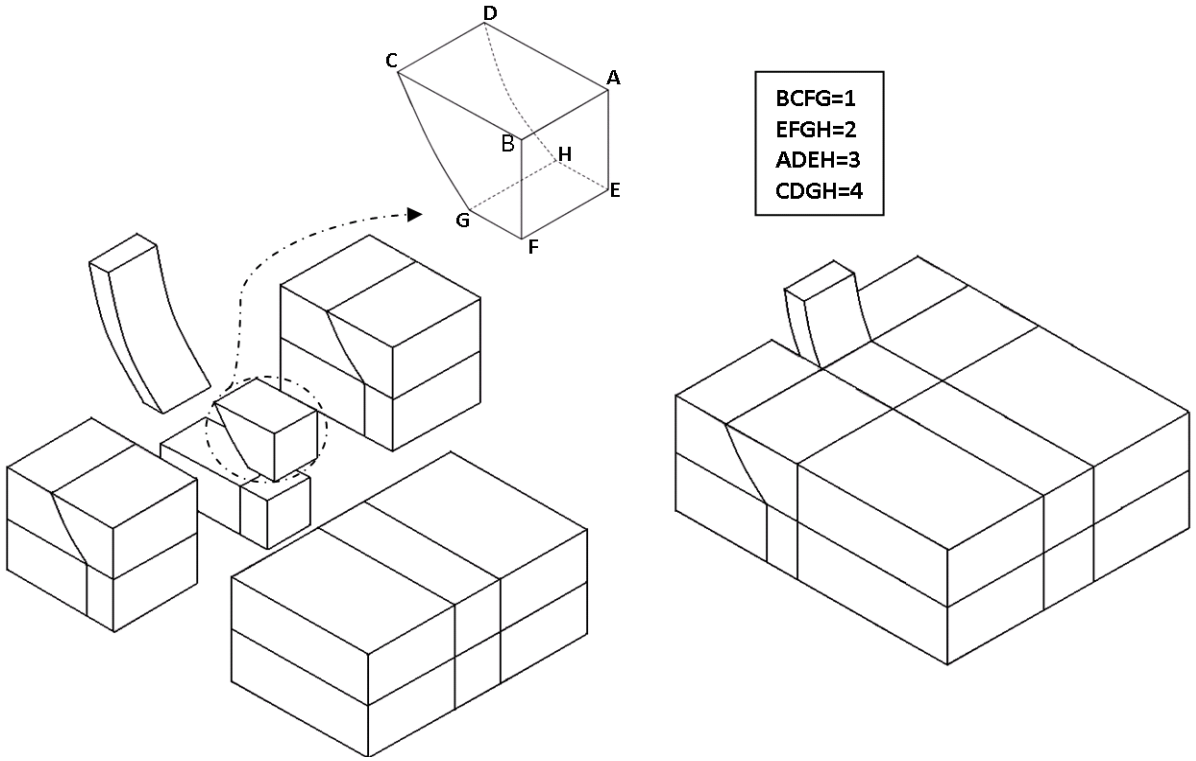

Figure 0.16: 3D Soil-blade model with contact surfaces. (1, 2, 3: contact surfaces with bonding and sliding option, 4: contact surface with sliding option)

1.9.1.3. Blades of triangular shapes

The last FE model is a general triangular model with the ability to change blade's rake angle and blade's curvature. Geometry of this FE model is sketched in Fig. 3.17. The model is parametric with several parameters defining the geometry of soil and tools same as for rectangular blade. Parameters and dimensions for the triangular blade model are almost same as the rectangular blade model. The only difference between these two models is the way of defining blade configuration. For defining the triangular blade configuration, five parameters are needed instead of four parameters that were used for rectangular blade shape modeling. The cutting portion of the blade is defined by five parameters α , α_c, α_s, w_1 and d_1, where α_s is the sharpness angle of blade. The curvature of the triangular blade is the same as the rectangular blade model which is shown in Fig. 3.17.

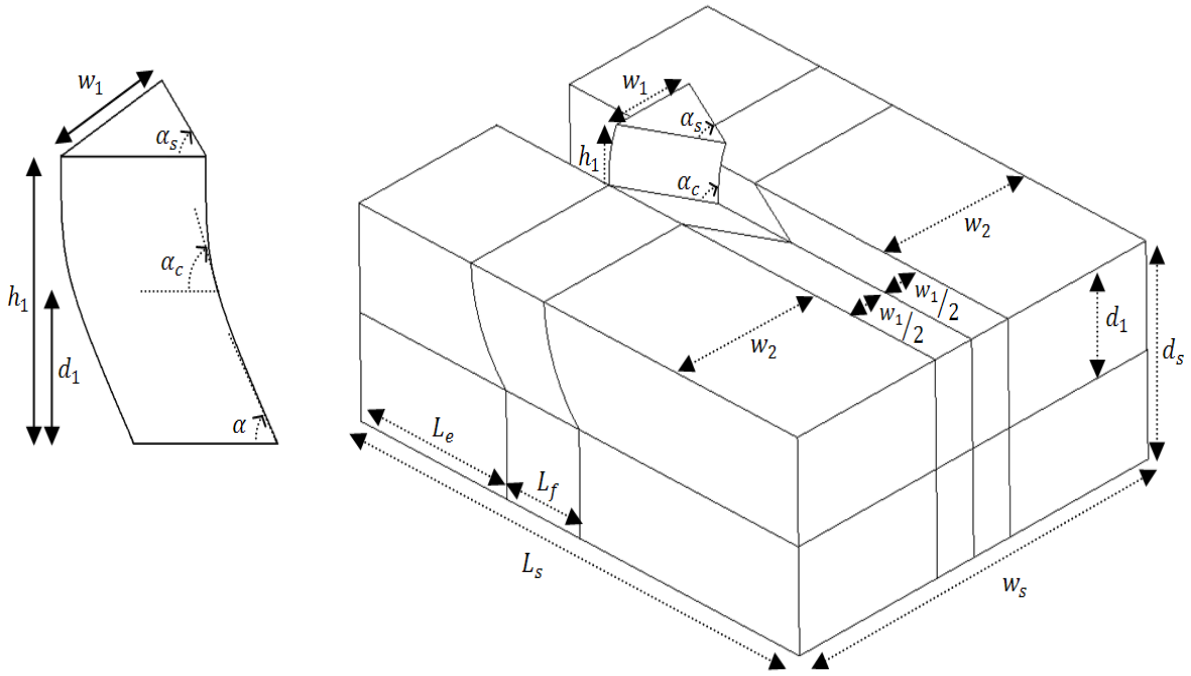

Figure 0.17: 3D soil-tool model dimensions for triangular narrow blade

Table 0.3: Soil-tool model dimensions that used in FEA

$w_1(mm)$	$d_1(mm)$	$L_f(mm)$	$L_e(mm)$
50	50	50	100

$\alpha(^\circ)$	$\alpha_c(^\circ)$	$\alpha_s(^\circ)$
45-60-75-90	45-60-75-90	30-40-52-75-90

The meshing pattern for the 3D triangular model is indicated in Fig.3.18 and the boundary conditions of the model are the same as the previous 3-D FE models.

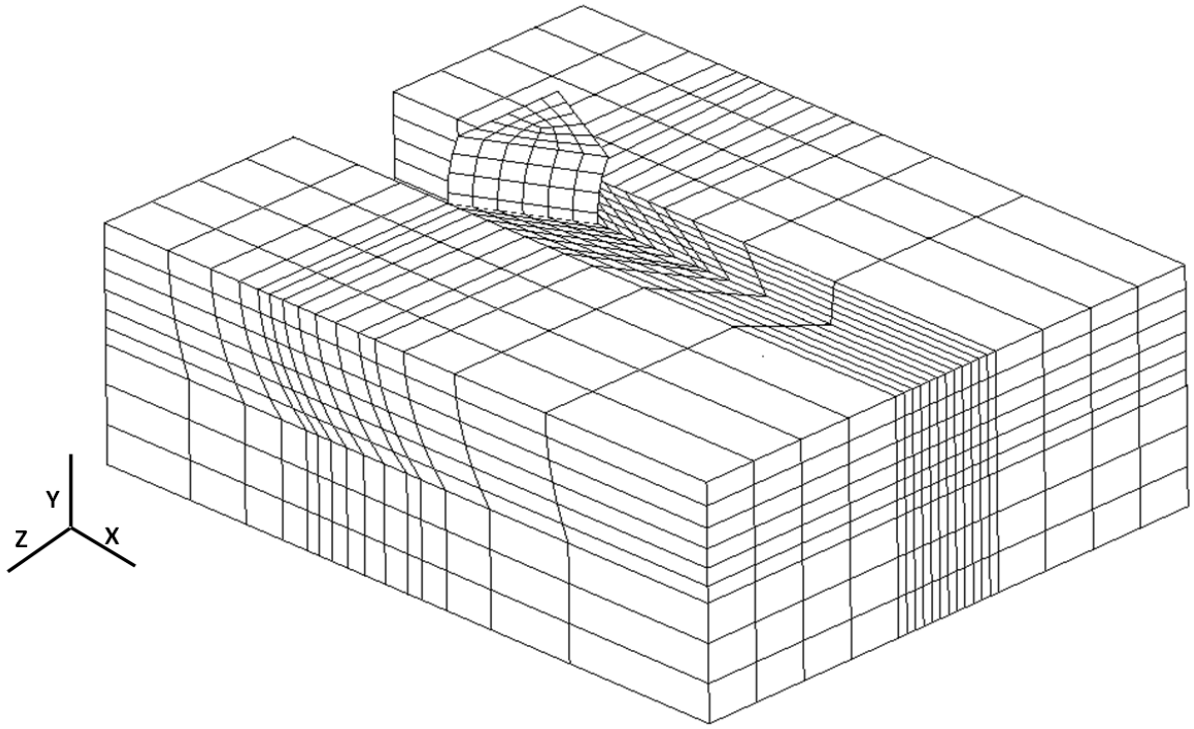

Figure 0.18: Finite element mesh for 3D soil-tool interaction model

The meshing shown in Fig. 3.18 uses a total number of 2358 hexagonal elements and 480 contact elements.

The other difference of this FE model with the previous ones is soil-blade and soil-soil contacting surfaces. Six contact surfaces are existed in this model, four bonding surfaces and two sliding. The same as the previous models, the two sliding surfaces are parallel to the front of the blade. However, based on the shape of the cut soil, four separation surfaces (two vertical and two horizontal cuts) parallel to the direction of the blade's motion are predefine as shown in Fig. 3.19

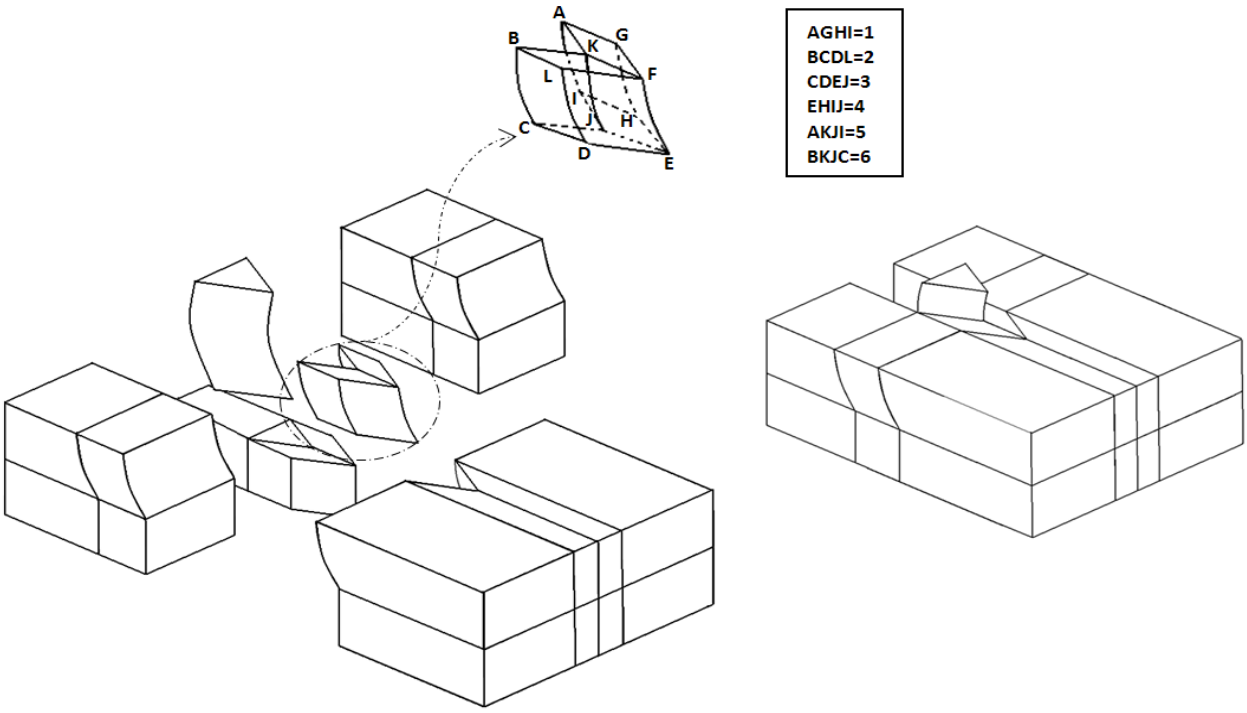

Figure 0.19: 3D Soil-blade model with contact surfaces. (1, 2, 3, 4: contact surfaces with bonding and sliding option, 5, 6: contact surfaces with sliding option)

Experimental method

Analytical and simulation models of soil - tool interaction are typically validated by experimentally measuring required forces to move the tool through the soil. In this chapter, Soil bin facility and devices engaged for my experimental procedure are presented. Load cells arrangement is discussed in detail. At the end, blades specifications and soil preparation is also explained.

1.10. Soil-bin facility

The Department of Mechanical Engineering (formerly Agriculture and Bio resource Eng.) at the University of Saskatchewan has an instrumented soil bin which was used in this research. The soil bin is 1.8 m wide and 12 m long with a movable length of 9 m. Experiments were performed using a linear monorail system in this soil bin. This monorail system, shown in Fig. 4.1 is capable of moving tools inside the soil at different speeds. There are two rails on each side of the soil bin which hold a tool carriage set by four wheels attached to the carriage at four corners. Also there is an 11.2kW electric motor equipped with speed control, electric clutch and break with the ability to change the speed from 1.2 km/h to 7.5 km/h. It should be mentioned that the carriage has a stationary control panel which is located beside the soil bin in order to control the motion of the carriage and attachments (roto-tiller, roller and sheep-foot packers) as shown in Fig.4.2.

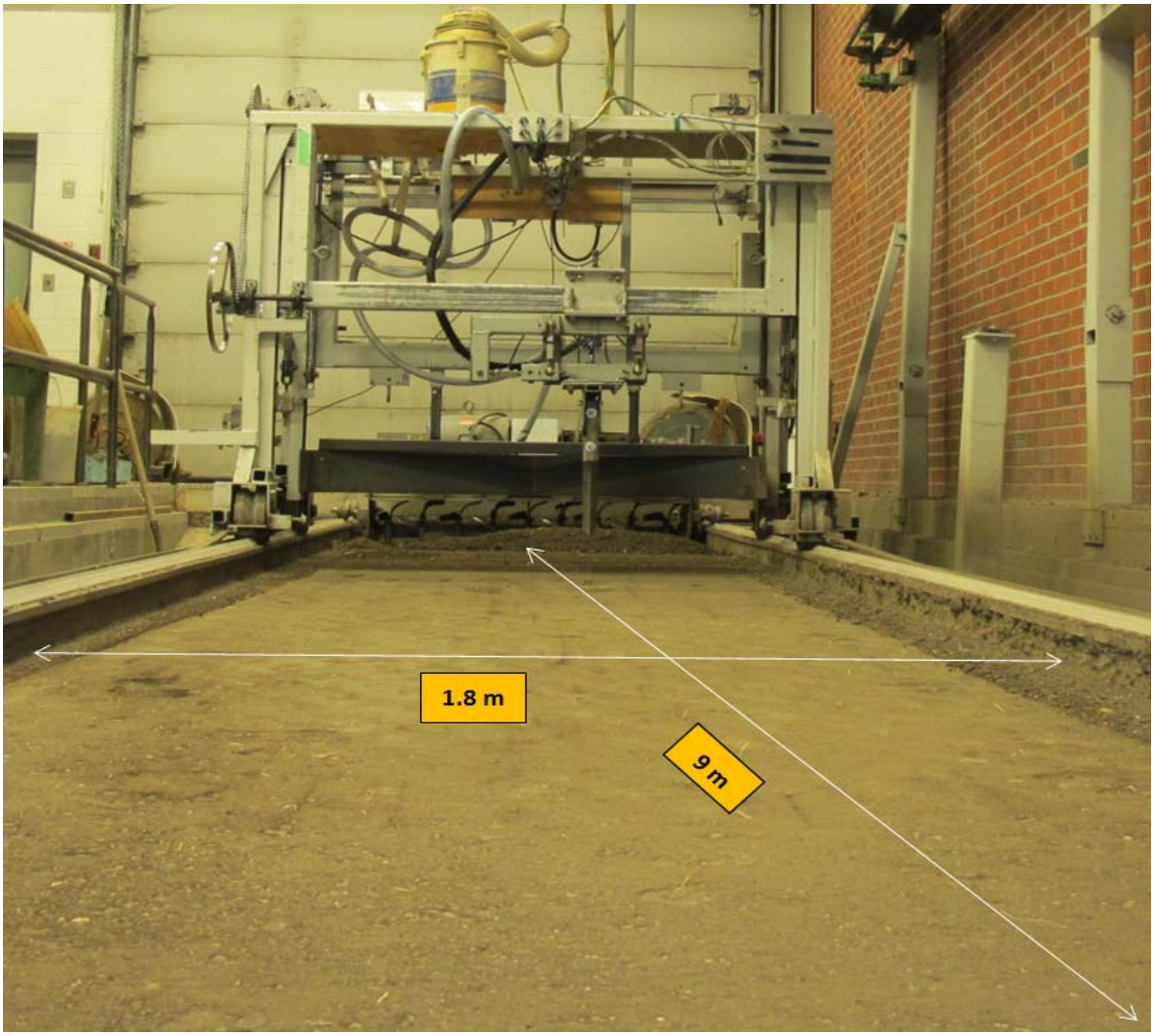

Figure 0.1: The monorail system at the University of Saskatchewan (12 m long and 1.8 m wide)

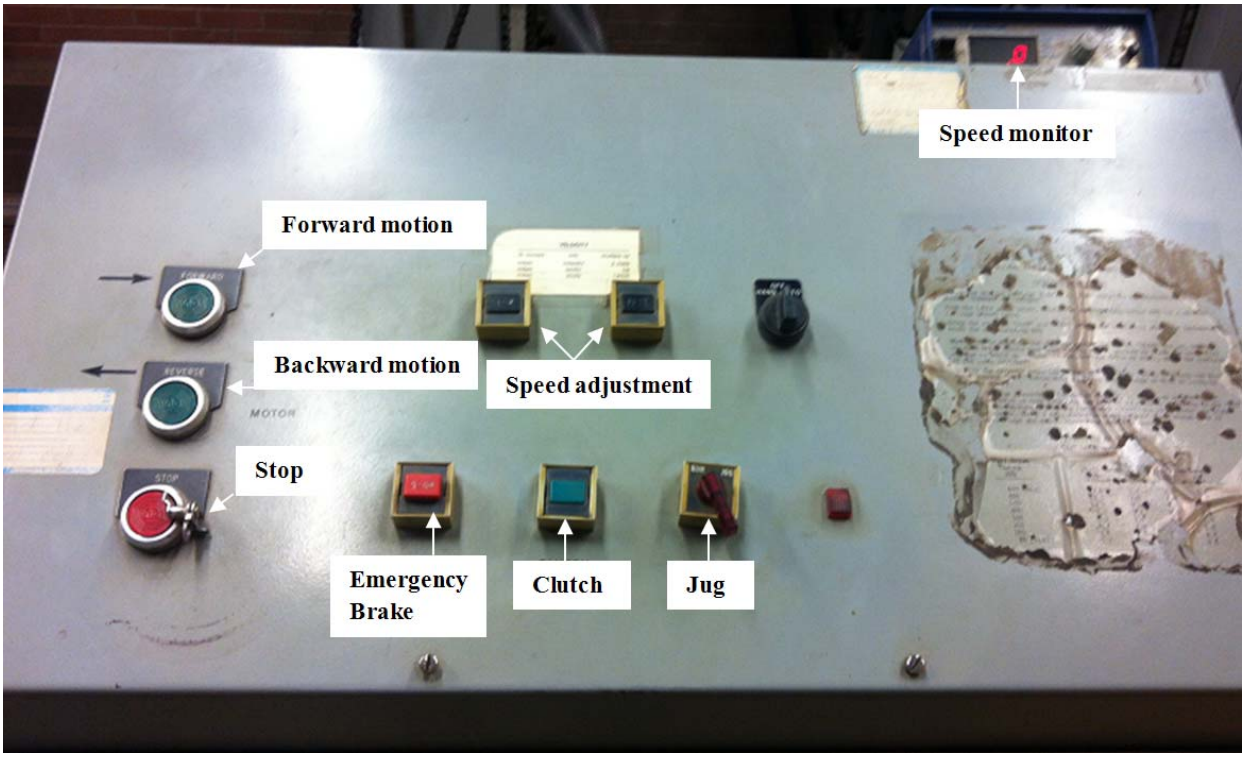

Figure 0.2: control panel for motion of carriage and attachments

As shown in Fig. 4.3(a, b), this tool carriage is equipped with six S-type load cells (SSM-1000); two horizontal to measure blade forces in direction of the blade motion through the soil, three vertical to measure the blade force in vertical direction and one side load cell to measure the lateral blade force. As [74] explained, this load cell arrangement makes it possible to measure the blade forces in three directions. During motion of the blade inside the soil, the load cells collected data at 2.5 millisecond intervals and sent them to a data recorder.

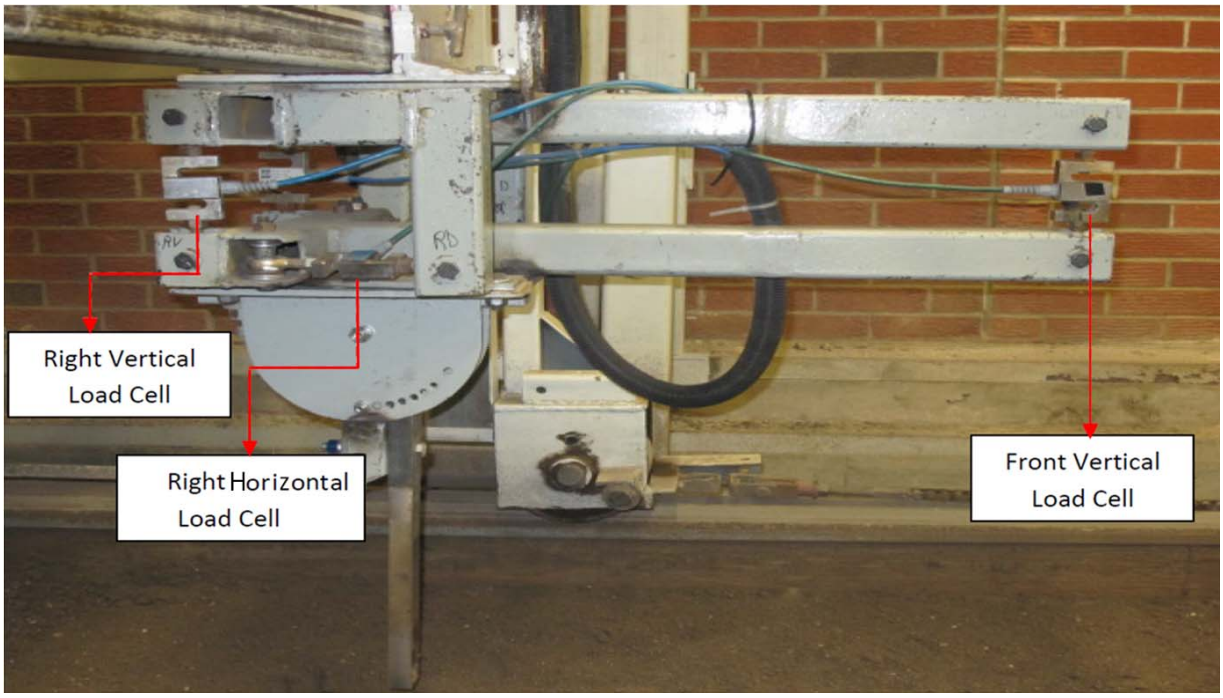

(a)

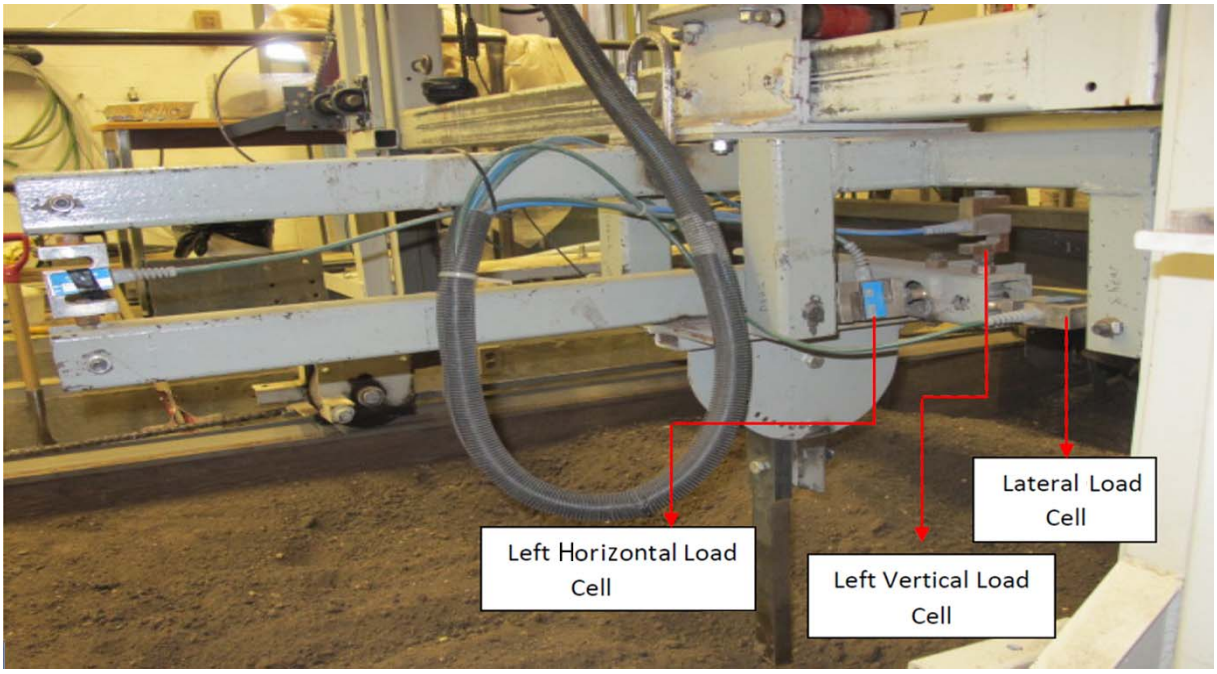

(b)

Figure 0.3: The monorail system with six S-type load cells arrangement shown in (a) and (b)

As shown in Fig. 4.4, the load cells measure the forces F_{V1}, F_{V2}, F_{V3}, F_{D1}, F_{D2}, F_{S1}. The total blade force is with the components P_X, P_Y, P_Z is applied to point A of the blade.

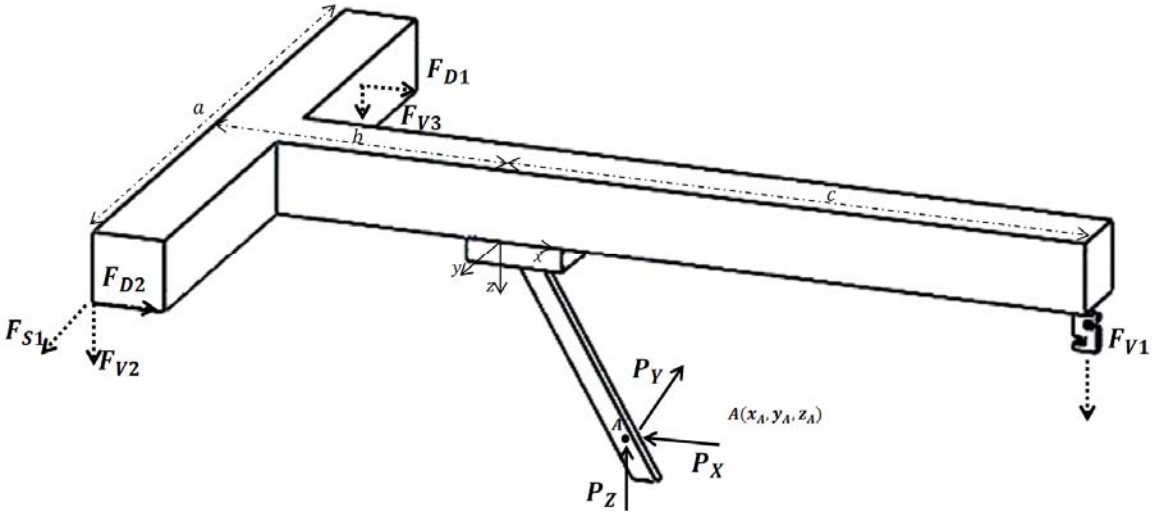

Figure 0.4: General load system of the monorail

In terms of the load cell, the three components of the blade force are

$$P_X = F_{D1} + F_{D2} \tag{4.1}$$

$$P_Y = F_{S1} \tag{4.2}$$

$$P_Z = F_{V1} + F_{V2} + F_{V3} \tag{4.3}$$

The measuring system can also provide information about location of point A.

The moment equilibrium about the x axis is

$$M_x = z_A P_Y - y_A P_Z \tag{4.4}$$

Where

$$M_x = (\frac{a}{2})(F_{V2} - F_{V3}) \tag{4.5}$$

Similarly the moment equilibrium about the y axis is

$$M_y = x_A P_Z - z_A P_X \tag{4.6}$$

where

$$M_y = b(F_{V2} + F_{V3}) - c(F_{V1}) \tag{4.7}$$

And the moment about the z axis is

$$M_z = y_A P_X - x_A P_Y \tag{4.8}$$

where

$$M_z = (\frac{a}{2})(F_{D1} - F_{D2}) - b(F_{S1}) \tag{4.9}$$

Equations (4.4), (4.6) and (4.8) in the matrix form are

$$\begin{bmatrix} 0 & -P_Z & P_Y \\ P_Z & 0 & -P_X \\ -P_Y & P_X & 0 \end{bmatrix} . \begin{bmatrix} x_A \\ y_A \\ z_A \end{bmatrix} = \begin{bmatrix} M_x \\ M_y \\ M_z \end{bmatrix} \tag{4.10}$$

The determinant of the LHS matrix is zero, which reflects the fact that the force P can be moved along the line of action without changing the moment about a point. Mathematically it means that the coordinates $x_A,\ y_A,\ ,z_A$ cannot be defined from Eq. (4.10).

However if one of these components is known, then the remaining components can be determined from the measurements. Based on the symmetric shape of the blades over the $z-x$ plane, it is reasonable to assume $y_A = 0$. Then

$$z_A = \frac{M_x}{P_Y}, \tag{4.11}$$

$$x_A = -\frac{M_z}{P_Y} \tag{4.12}$$

Substituting in the third equation results in

$$P_X M_x + P_Y M_y + P_Z M_z = 0 \tag{4.13}$$

This equation can be used to verify correctness of the measuring system.

4.2. Tools specifications

Two types of blades (rectangular and triangular cross section) were made in order to validate the FE simulation results. As shown in Figs. 4.5 and 4.6, the steel rectangular blade has 480 mm length, 40 mm width and 20 mm depth where the steel triangular blade has the same length with 50 mm depth. These blades were attached to the main frame with special holder (Fig. 4.7) that enables the blades to change their position across the soil bin width. Also this holder has the ability of changing the rake angle of blades which were used during the experiments in order to validate simulation results. To ensure the accuracy of the equipment, load cells were calibrated by the dead weight method in advance of measuring by CNH group who used the equipment before me.

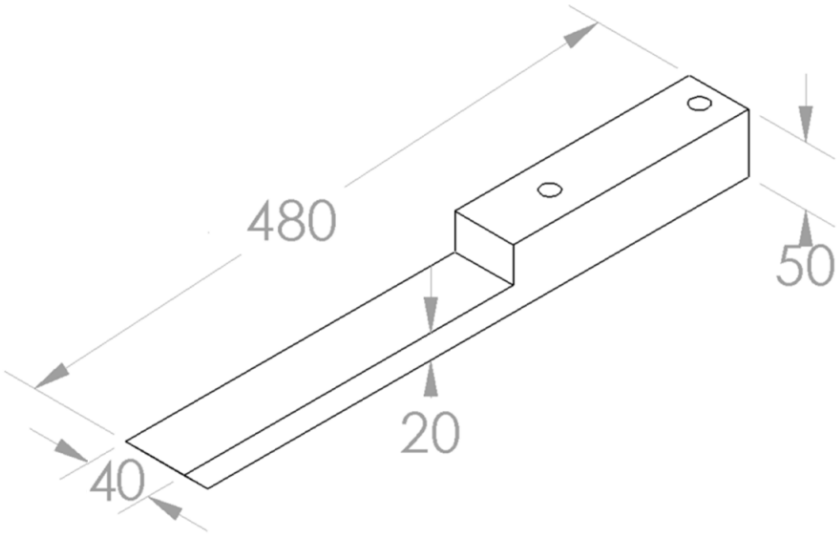

Figure 0.5: The steel rectangular blade shape which is used in experiments (units are in mm)

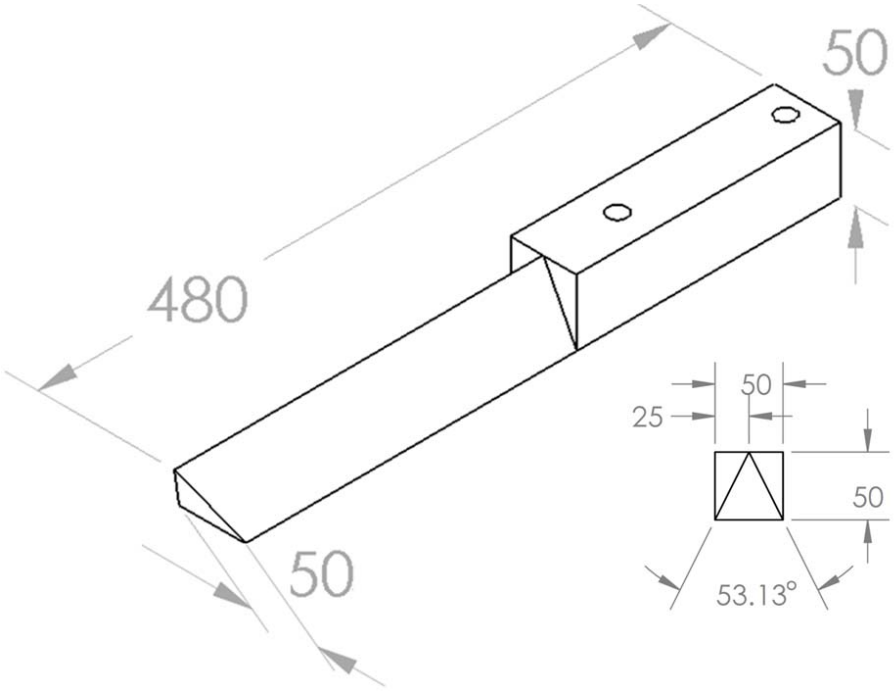

Figure 0.6: The steel rectangular blade shape which is used in experiments

As mentioned above, by using the linear monorail system the interaction speed can be managed. According to Godwin and O'Dogherty [75], the effect of blade speed on the blade force is

negligible for narrow blades if the speed is less than $\sqrt{5g(w+0.6d_1)}$; where g, d_1 and w represents gravitational acceleration and depth and width of the blade respectively. For the experiments, blades (rectangular and triangular) with $w_1 = 0.04m$ for the rectangular blade and $w_1 = 0.05m$ for the triangular blade, $g = 9.81 m/s^2$ and $d_1 = 0.05m$ for both of the blades, has the speed limit of 1.85 m/s (6.66 km/h) and1.98 m/s (7.128 km/h) respectively. All tests were performed at a speed of 0.56 *m/s* (2 km/h) in order to ignore the effect of the interaction speed and conform with theoretical results consequently.

Figure 0.7: Blade holder with the ability of changing the rake angle of blades.

The blade sizes and depth of the blades inside the soil in the experiments were identical to those used in the FE simulations. Each experiment started after placing the blade at the required depth.

4.3. Soil preparation

The preparation of soil for soil bin experiment included four steps. In the first step, water was sprayed along the soil bin by a sprinkler. Since uniformity of soil moisture is essential for this kind of experiment, the spraying was done in a way to water the entire soil bin with the same amount. In the second step, roto-tilling, dry and wet layers of soil were mixed together in order to make the moisture of the soil along the soil bin uniform.

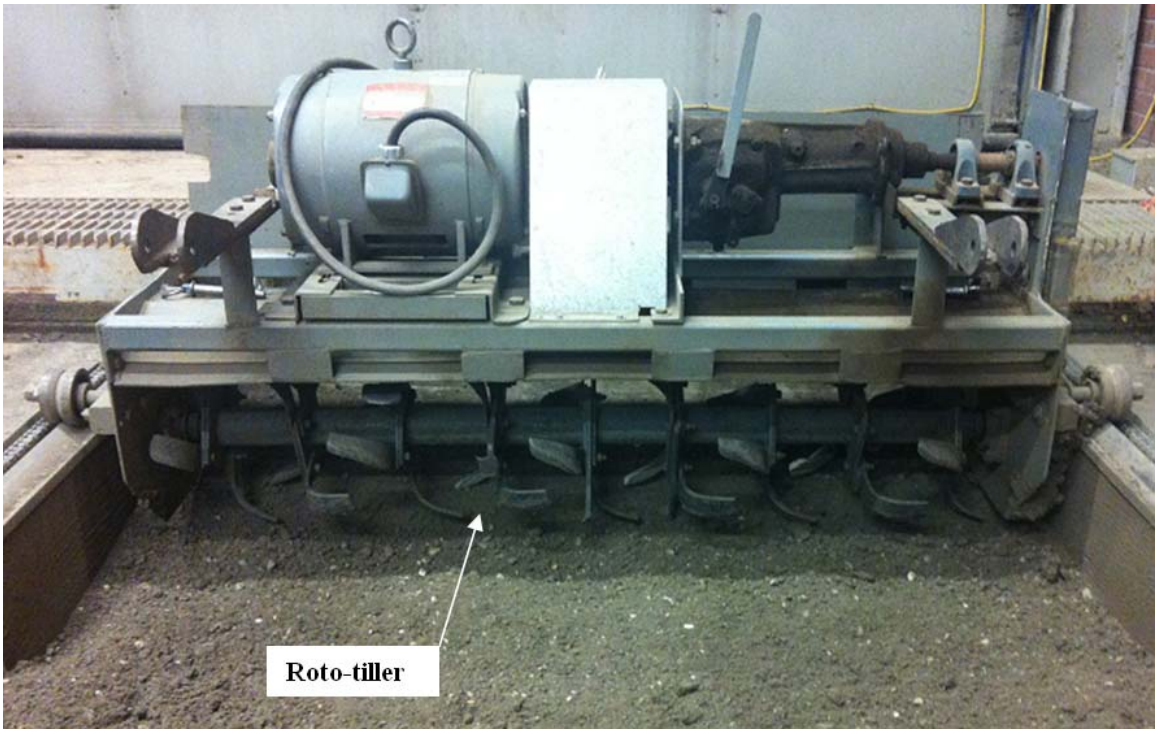

Figure 0.8: Roto-tiller used to loosen hard soil and mix dry and wet soil.

A roto-tiller, as shown in Fig. 4.8, was attached to the main frame in order to break any hard soil and mix it with wet soil. During tilling, water spraying can be continued in places with lower soil moisture. This tilling may be required to be repeated several times in order to have uniform soil

in all parts of the soil bin. After tilling, the soil was levelled by scraper blade. This blade, which has the same width as the frame, was attached to the back of the main frame with the ability to move up and down as shown in Fig. 4.9. Soil compacting is the last step of soil preparation. In this step packers (sheep-foot packer and roller packer) shown in Fig. 4.10, were attached in front of the main frame to compact the soil. It was necessary to level the soil again after using sheep-foot packer which distributed the soil before using the roller packer.

Figure 0.9: Scraper blade with the same width as the frame in order to level the soil

Figure 0.10: Sheep-foot packer and roller packer used to pack the soil

Different soil compaction levels can be obtained by varying the number of packer passes. A low compaction level can be achieved by two passes of the sheep-foot packer and four passes of the roller packer. A hard compaction level which is similar to most agricultural field conditions can be obtained by ten passes of sheep-foot packer and four passes of roller packer as Rosa [59] stated. During the experiments, a hard compaction level was used to simulate the field condition and compared with FE results. Also the soil selected for this experiment is the type of soil commonly found in Saskatchewan, which is silty clay loam (47.5% sand, 24.2% silt and 28.3% clay). The soil properties with 7% water content are given in Table 3.1 as Bankole [24] calculated.

Results and discussions

In this section the FE models and procedure proposed are tested for convergence and accuracy. The main focus is on accuracy of calculating the draft force. First the effects of the compacting strain limit and the soil internal friction angle on the calculated draft force are presented. Then the effect of meshing is discussed. Finally, the results are validated by comparing them with the formulas that for straight blades are available in the literature. Also, the FE results were validated experimentally by testing several soil blade interactions in the soil bin facility (see chapter 4). The effects of blade width, blade depth and rake angles on the blade force are also investigated. Then, the effects of curved blade and changing the shape of blade are examined.

1.11. Effect of the compacting strain limit on the draft force

The magnitude of the strain component in the direction of the blade's motion to initiate separation (refer to as the compacting strain limit, ε_c in Sec. 3.2.3) is crucial in this analysis. In particular, the draft force is affected by the choice of the magnitude of ε_c. In order to examine this, the numerical experiment was performed on the blade with $d_1 = 50mm$, $w_1 = 50mm$, $\alpha = 60^\circ$ and the soil with properties that are listed in Table.3.1 (in particular for the friction angle $\varphi = 35^\circ$). The draft forces that were calculated assuming different values of ε_c are shown in Fig. 5.1. As can be seen, the calculated draft forces increase sharply until the strain limit, ε_c is around 0.3. Then the force stays almost constant (for $\varepsilon_c \geq 0.3$) which means that further distortion of the monitored element does not have significant effects on the calculated force. It should be mentioned that the number of the load steps required in this analysis increases quite fast with an increasing value of ε_c. For example by assuming $\varepsilon_c = 0.45$ (instead of $\varepsilon_c = 0.3$), the time required to calculate the correspondent force increases by more than 40%. However, the difference between blade (draft) forces with compacting strain limit 0.3 and its constant final

value (which here corresponds to compacting strain of 0.45) is around 3% ($F = 458N$ at $\varepsilon_c = 0.45$ and $F = 446N$ at $\varepsilon_c = 0.3$). Thus for the computational efficiency and to make a balance between computational efforts and accuracy, $\varepsilon_c = 0.3$ was selected to initiate separation for this type of soil. This 3% is considered as a settling value of blade (draft) force for this analysis.

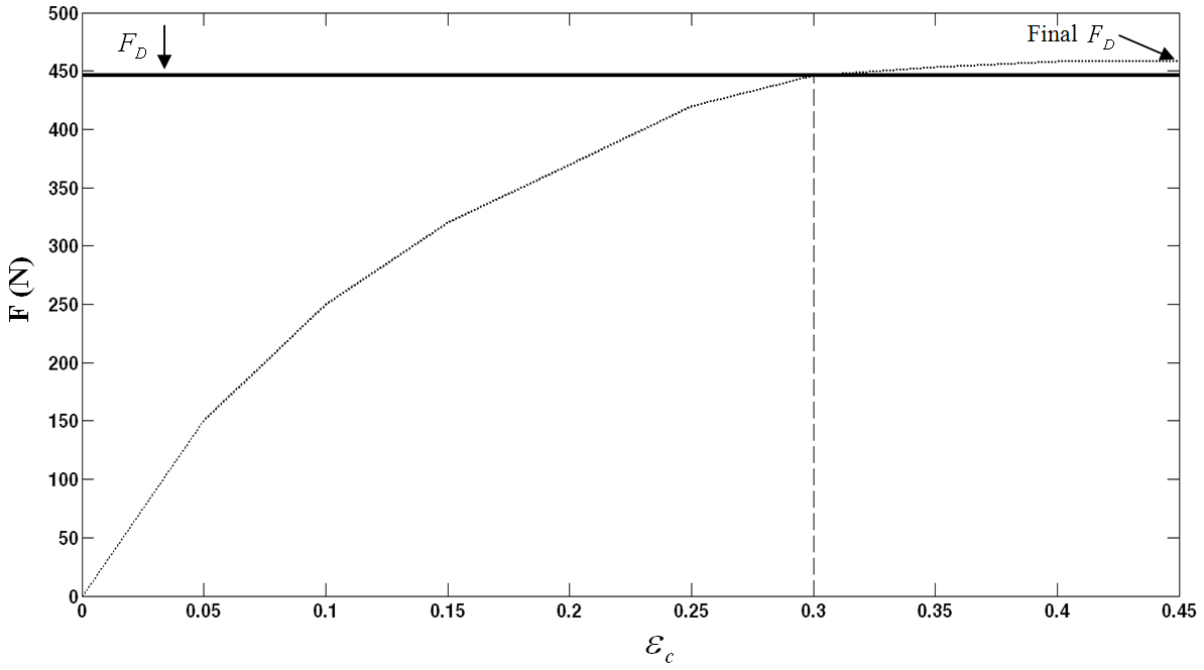

Figure 0.1: Effect of compacting strain limit on the calculated force for soil with $\varphi = 35^\circ$

1.12. Effect of soil internal friction angle on compacting strain limit

It turned out that the $F - \varepsilon_c$ curves such as shown in Fig. 5.1 are somewhat affected by the type of soil characterized by friction angle φ. In order to examine this effect, the draft force was calculated for a straight rectangular blade with $d_1 = 50mm$, $w_1 = 50mm$, $\alpha = 60^\circ$ and using the soil internal friction angles varying from 20° to 40°. For example, for the internal friction

angle $\varphi = 20^{\circ}$, the draft forces calculated for different ε_c are shown in Fig. 5.2. These forces increase sharply until for $\varepsilon_c < 0.2$ and then stay almost constant for $\varepsilon_c \geq 0.2$. The difference between forces with compacting strain limit 0.2 and 0.35 is around 3% ($F = 221N$ at $\varepsilon_c = 0.35$ and $F = 215N$ at $\varepsilon_c = 0.2$), therefore for computational efficiency $\varepsilon_c = 0.2$ should be selected in any further analysis of this type of soil. With the same procedure, $\varepsilon_c = 0.35$ was selected to initiate soil separation for the soil with $\varphi = 40^{\circ}$ as shown in Fig. 5.3.

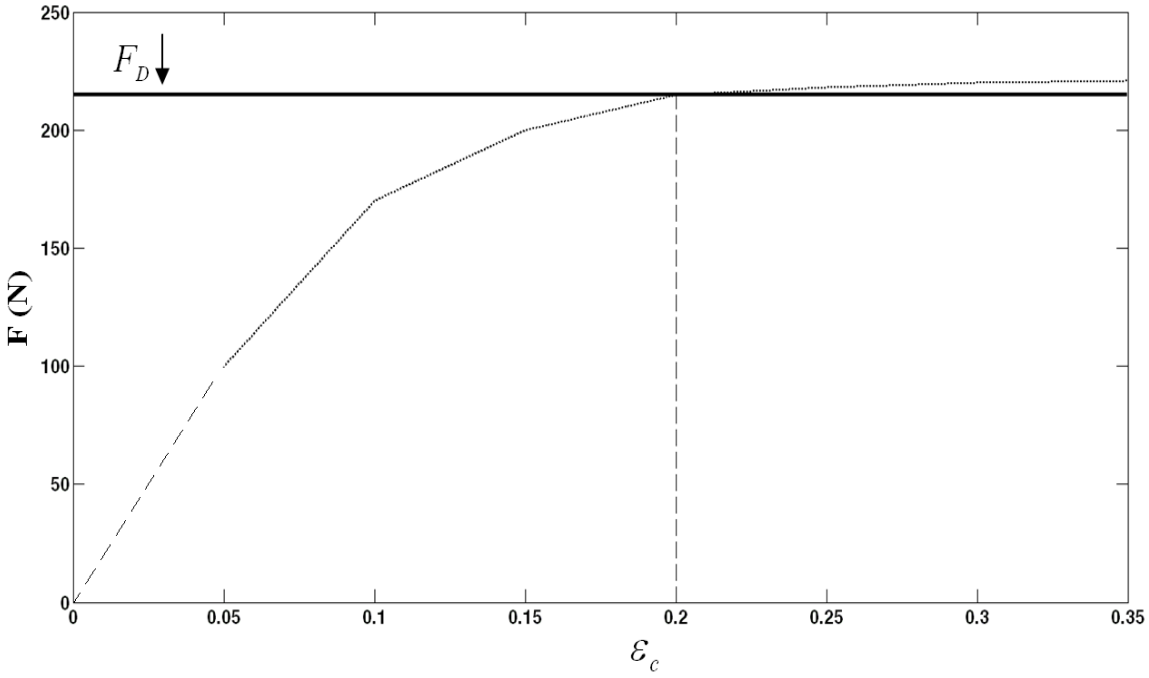

Figure 0.2: Effect of compacting strain limit on the calculated force for soil with $\varphi = 20^{\circ}$

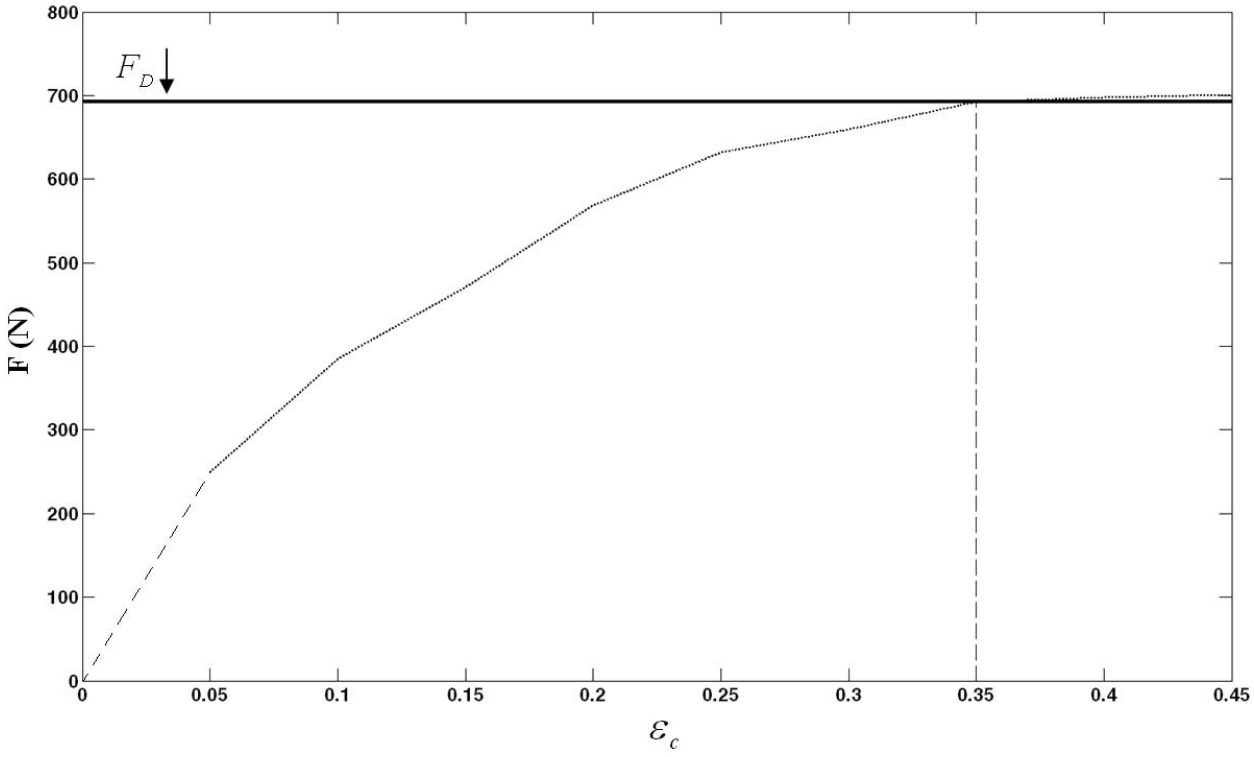

Figure 0.3: Effect of compacting strain limit on the calculated force for soil with $\varphi = 40^\circ$

This procedure was applied for several analyses with $20^\circ \le \varphi \le 40^\circ$ and the relationship between the soil internal friction angle and compacting strain limit was established as shown in Fig. 5.4. As can be seen for the soil internal friction angle analysed here, the compacting strain limit varies almost linearly within the range $0.2 \le \varepsilon_c \le 0.35$. Also it should be mentioned that the soil cohesion does not seem to have any meaningful effect on the $F - \varepsilon_c$ curve.

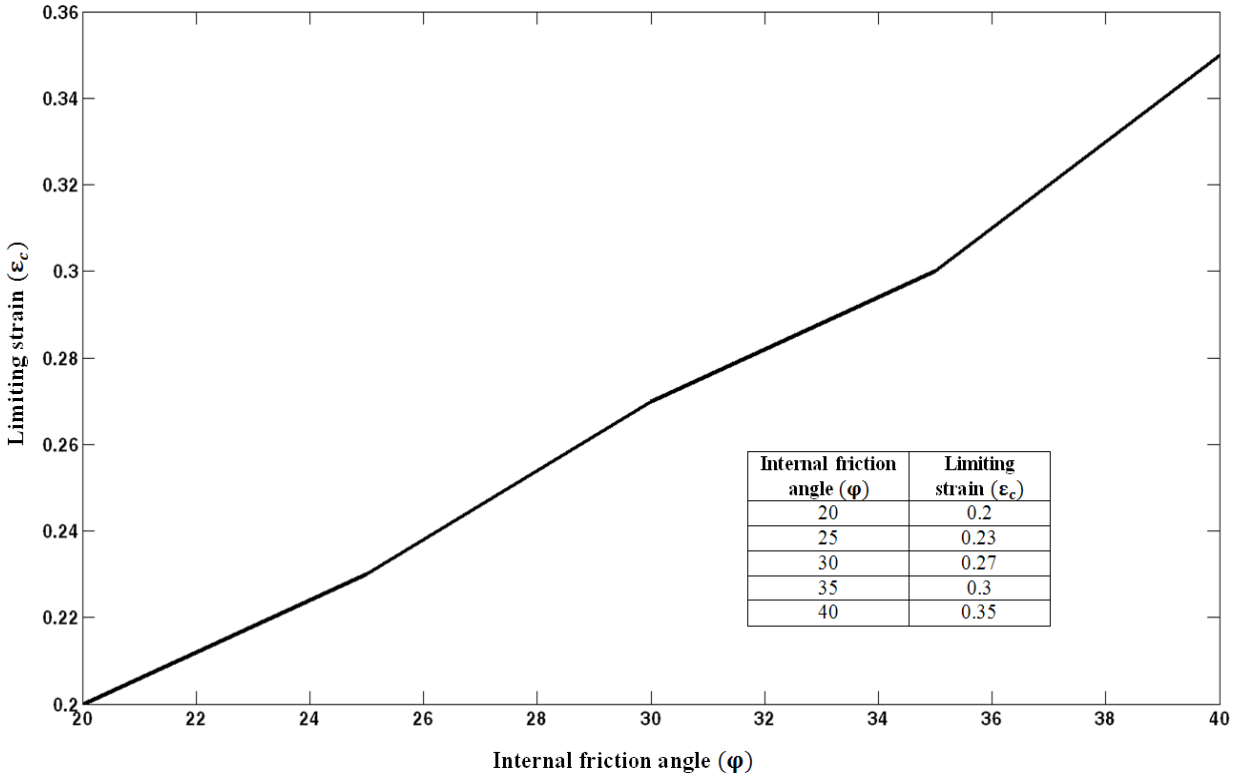

Internal friction angle (φ)	Limiting strain (ε_c)
20	0.2
25	0.23
30	0.27
35	0.3
40	0.35

Figure 0.4: Effect of soil internal friction angle on the limiting compacting strain

1.13. Effects of meshing

As discusses in Section 3.2.4 the choice of the size of elements on the separation surface in the vicinity of the blade's tip, denoted by *e* in Fig. 3.8, affects the calculated relationship between the draft force and the displacement of the blade. Typical results for the 3D soil blade interaction model with different *e* and for $d_1 = 50mm$, $w_1 = 50mm$, and $\alpha = 90^\circ$ (vertical blade) are shown in Fig. 5.5. Clearly, smaller *e* reduces the difference $F(T_i) - F(B_i)$, but also makes the mesh more dense that in turn increases the computation time.

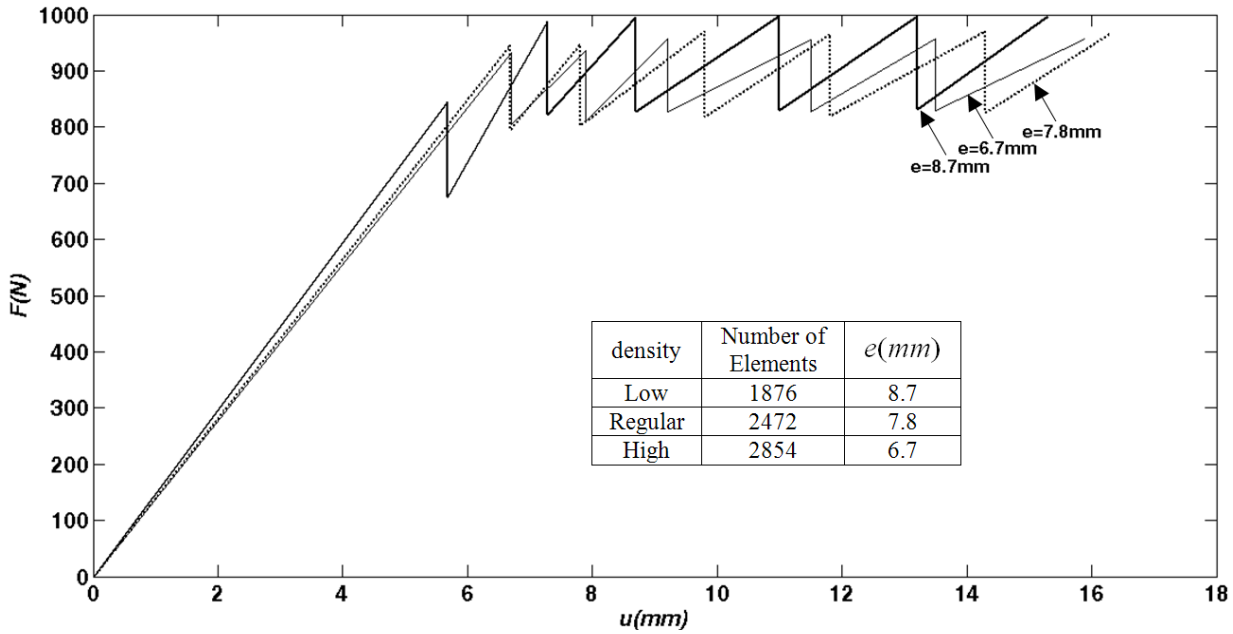

density	Number of Elements	$e(mm)$
Low	1876	8.7
Regular	2472	7.8
High	2854	6.7

Figure 0.5: The draft force *F* for different element size e (and different mesh density)

For example, if $e = 8.7mm$ (low mesh density, 1876 elements) then the calculation time to obtain the *F*-*u* plot for *u* up to 16*mm* is about 15 hours (computer with Intel core i5 4 GH processor and 3.2 GB of RAM) . If the mesh size is reduced to $e = 7.8mm$ (regular mesh density, 2472 elements) then the time increases to 19 hours, and to 22 hours if $e = 6.7mm$ (high mesh density, 2854 elements).

The effect of *e* on the average force $\overline{F} = \left[(F(T_i) + F(B_i)\right]/2$ is shown in Fig. 5.6. As can be seen, results for the regular and high mesh patterns are practically indistinguishable; therefore for computational efficiency the regular mesh density was selected for this case. For the low mesh density the force $F_D = 915N$ (see the definition in Fig. 3.7), then it drops by 2% to $F_D = 896N$ for the regular mesh density, and drops 0.3% further to $F_D = 893N$ for the high mesh density.

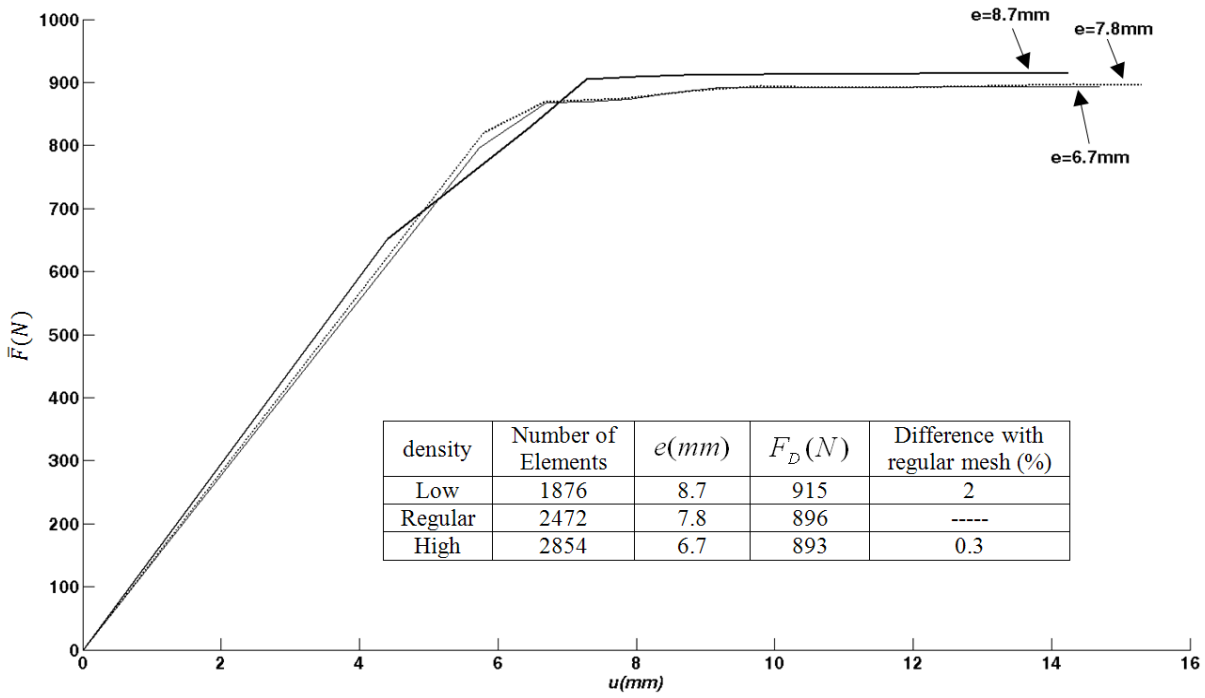

density	Number of Elements	$e(mm)$	$F_D(N)$	Difference with regular mesh (%)
Low	1876	8.7	915	2
Regular	2472	7.8	896	-----
High	2854	6.7	893	0.3

Figure 0.6: Effect of e (and the mesh density) on the average draft force $\overline{F}$.

Similar results for another 3D soil-blade interaction model with $d_1 = 50mm$, $w_1 = 50mm$, and $\alpha = 60^\circ$ are presented in Fig. 5.7 and 5.8, where e = 8.4, 7.0, 5.8 were used.

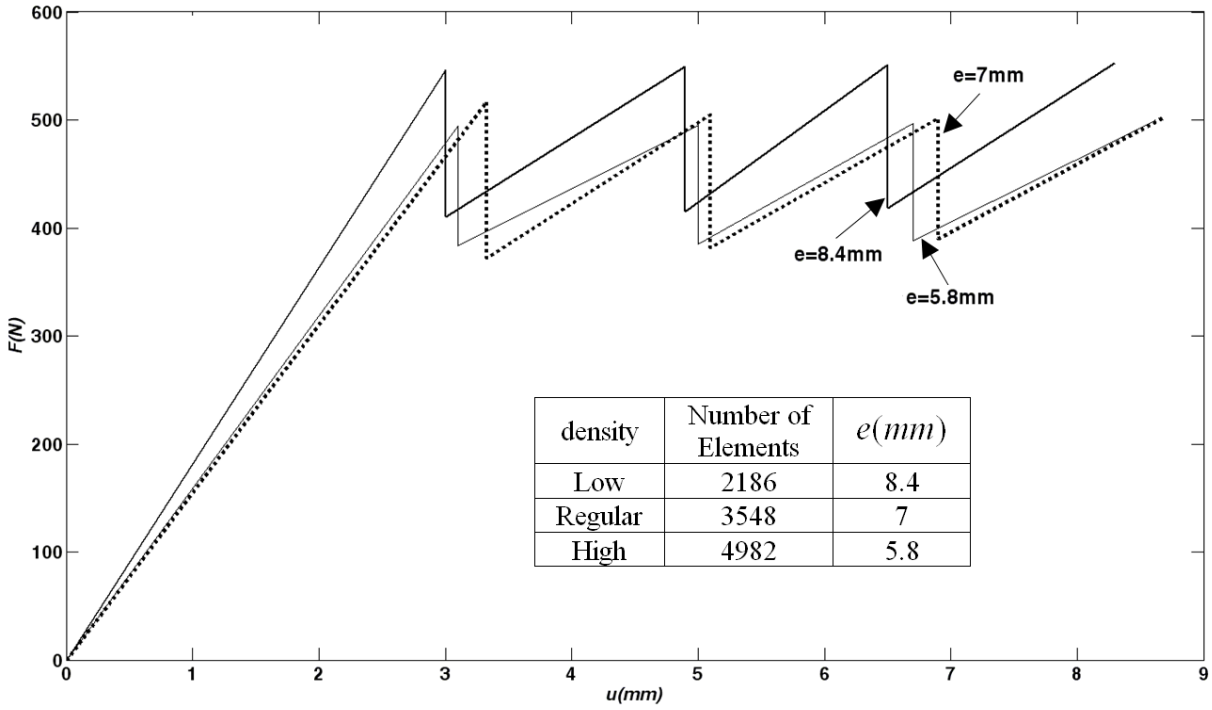

density	Number of Elements	$e(mm)$
Low	2186	8.4
Regular	3548	7
High	4982	5.8

Figure 0.7: Variation of the draft force F with element size (for $\alpha = 60^{\circ}$)

The corresponding average draft force $\overline{F}$ is shown in Fig. 5.8. For e = 8.4mm (low density meshing, 2186 elements) the draft force $F_D = 485N$. This force drops by 7.8% to $F_D = 446N$ if the mesh size is reduced to e = 7mm (regular mesh density, 3548 elements), and further by 1.3% to $F_D = 441N$ if e = 5.8mm (high mesh density, 4982 elements). The results for the regular and high mesh patterns are practically indistinguishable; for computational efficiency the regular mesh density could be selected to analyze this case.

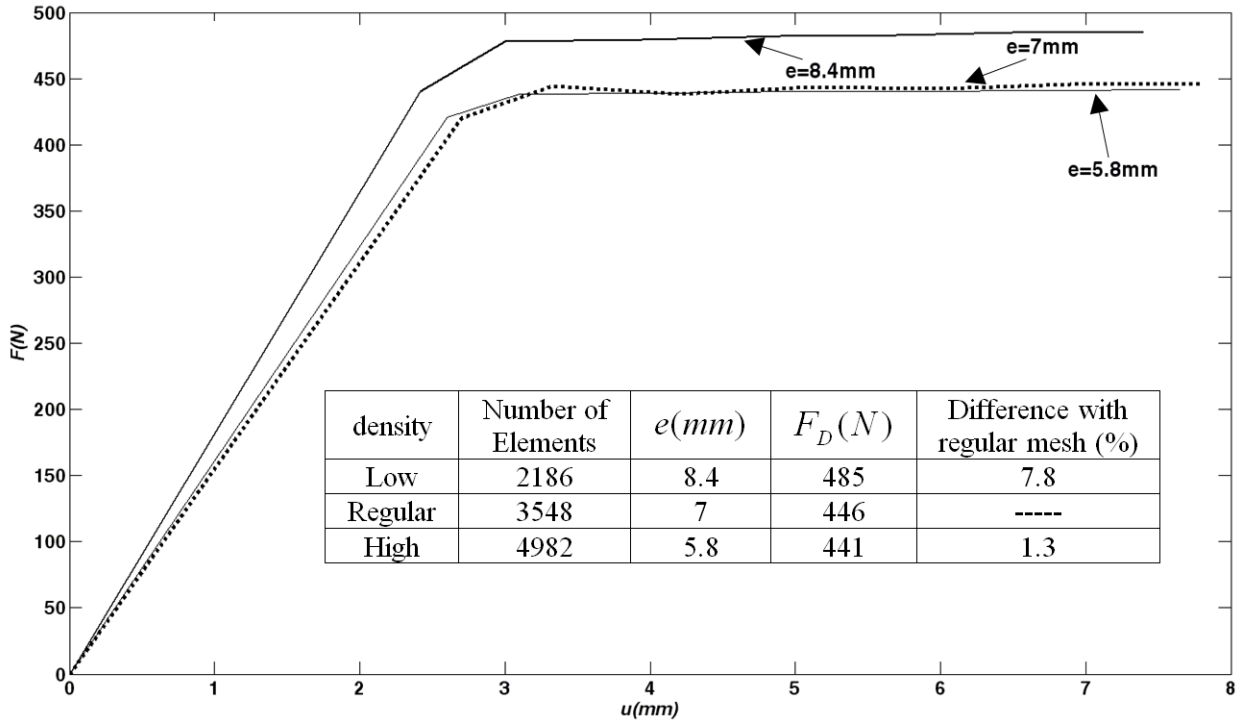

density	Number of Elements	$e(mm)$	$F_D(N)$	Difference with regular mesh (%)
Low	2186	8.4	485	7.8
Regular	3548	7	446	-----
High	4982	5.8	441	1.3

Figure 0.8: Variation of the averaged drag force $\overline{F}$ with the element size (for $\alpha = 60^\circ$).

1.14. Model verifications

1.14.1. Analytical validation

1.14.1.1. Validation of 2D model

2D elements can be used to simulate action of wide blades. In order to model separation between elements above and below separation surface, L_h, (Fig. 3.4) the nodes representing soil are connected using contact elements that allow to activate or deactivate the bonding contact between them. In this process the blade force $\overline{F}$ (output) is calculated as a function of distance traveled u (input) by the blade through the soil.

Using the procedure discussed in 3.2.4, draft force acting on the blade can be determined. A typical plot is shown in Fig. 5.9 representing blade force as the blade moves through the soil. For

this 2D typical simulation, the blade was vertical $(\alpha = 90^{\circ})$ and the required soil-blade parameters were listed in Table 3.1. The draft force is the sum of all horizontal nodal forces on the blade at a specified displacement. This force increases from zero to about 10 KN around the blade displacement of $6mm$ and stays almost constant. The average force, $\overline{F} = \left[(F(T_i) + F(B_i)\right]/2$ reaches the value of $10404N$, and is considered as the draft force F_D as obtained from the simulation.

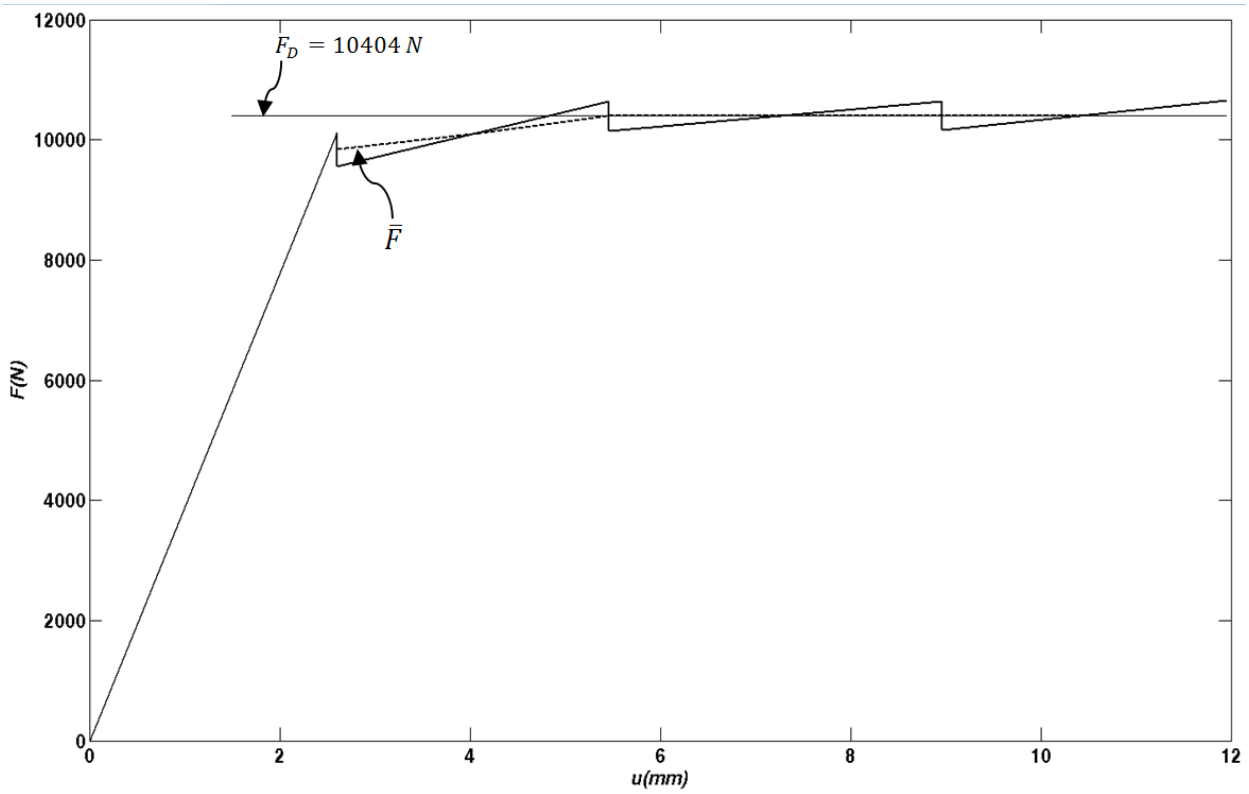

Figure 0.9: The blade (draft) force versus blade displacement for 2D blade with rake angle of 90°. Draft force produced $F_D = 10404N$

Prediction of the draft force in soil-blade interaction have been proposed by many researchers. Onwualu and Watts [46] reported that the best correlation between analytical and experimental results can be achieved by using McKeyes approach. In this study we used the McKeys

analytical approach [25] to compare forces acting on a blade with FE results for both wide and narrow blades.

He proposed the following expression for a wide blade:

$$F_D^A = (\lambda d_1^2 K_a + C d_1 K_c + Q_b d_1 K_q) w_1 \tag{5.1}$$

Where F_D^A is the total force, λ is the soil's specific weight, C is soil cohesion, Q_b is bearing pressure, d_1 is depth of blade inside soil (interaction), $K(K_a, K_c, K_q)$ are force factors for wide blade and w_1 is width of the blade which should be at least ten times of the depth of interaction $(10d_1)$ to be considered as wide blade. Force factors $K(K_a, K_c, K_q)$, depend on the soil friction angle ϕ, the blade rake angle α, angle of soil failure plane θ and soil-blade friction angle δ. The horizontal components of the total blade force F_D^A, can be derived as

$$F_{DH}^A = F_D^A \sin(\alpha + \delta) \tag{5.2}$$

In the present study, the value of Q is negligible, thus K_q in eq. (5.1) is not needed.

K_a and K_c were derived by [8] as

$$K_a = \frac{(\cot\alpha + \cot\theta)\sin(\theta + \phi)}{\sin(\alpha + \theta + \phi + \delta)} \tag{5.3}$$

$$K_c = \frac{\cos\phi}{\sin\beta \sin(\alpha + \theta + \phi + \delta)} \tag{5.4}$$

Where θ is

$$\theta = arc\cot\left[\frac{\sqrt{\frac{\sin(\alpha+\delta)\sin(\delta+\phi)}{\sin\alpha\sin\phi}} - \cos(\alpha+\delta+\phi)}{\sin(\alpha+\delta+\phi)}\right] \tag{5.5}$$

By using variables from Table 5.1 and using eq. (5.3-5.5), values of (K_a, K_c) are calculated as reported in Table 5.1.

Table 0.1: Horizontal component of K's for obtaining the blade force.

Variables	K_a	K_c
$\alpha = 90^\circ, \delta = 23^\circ, \phi = 35^\circ$	4.88	10.85

By using equation (5.1) and (5.2) and using values in Tables 5.1 and 3.1, the force on the blade can be determined as,

$$F_{DH}^{A} = \left[\sin(\alpha+\delta)(\lambda d_1^2 K_a + C d_1 K_c) w_1\right] = 10121.8N \tag{5.6}$$

The difference in the total blade force between FE result ($F_D = 10404N$, see Fig. 5.9), and analytical value $F_{DH}^{A} = 10121.8N$ is found to be about 2.7%; this can be considered as validation of the FE results.

1.14.1.2. Determining the blade force and model validation in 3D

A typical plot of the blade force calculated by the procedure presented in section 3.3.2 is shown in Fig.5.10 for 3D soil-blade interaction. This is the case with $\alpha = 60^\circ$ and $d_1 = 50mm$, and $w_1 = 40mm$, modeled by the mesh with the element size $e = 7mm$ (as discussed in Sec. 5.3). As shown in Fig. 5.10, the average force $\overline{F}$ is almost horizontal after the first iteration already, and the corresponding blade force is $F_D = 408N$.

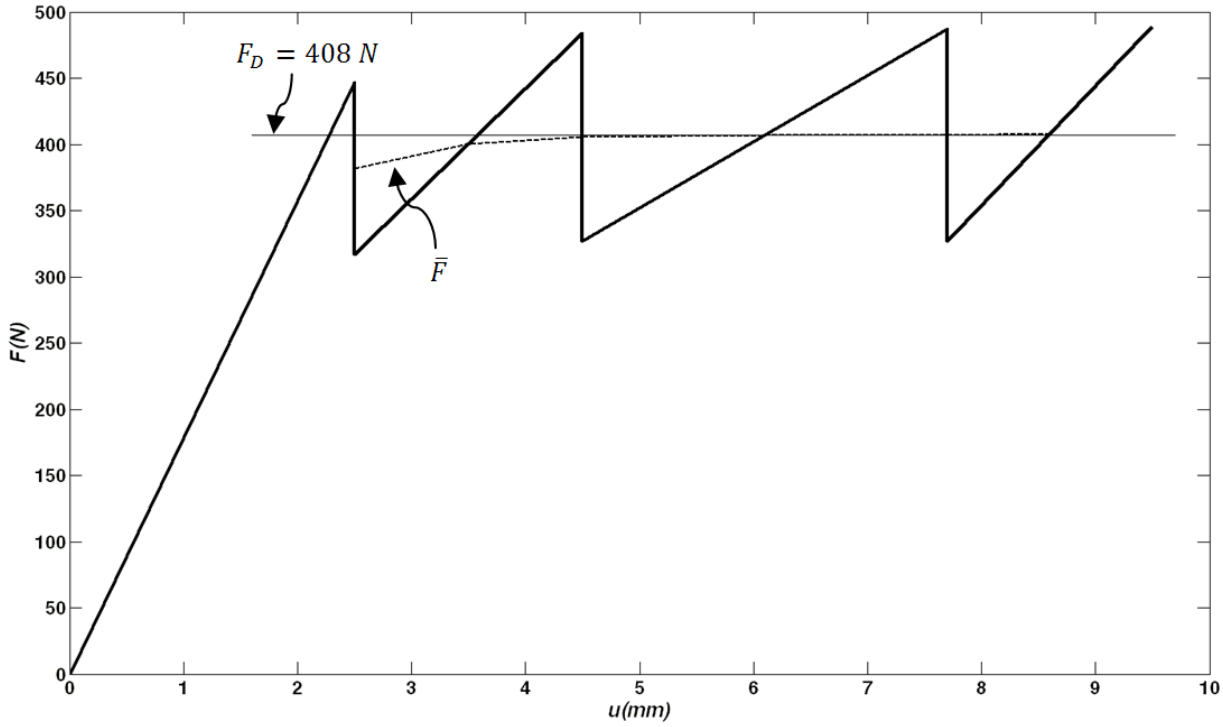

Figure 0.10: The force acting on the blade and its mean value (draft force F_D)

This force can be validated by comparing it with the analytical results. McKyes and Ali [8] proposed the following expression for a narrow blade:

$$F_D^A = (\lambda d_1^2 N_\gamma + C d_1 N_c + Q d_1 N_q) w_1 \tag{5.7}$$

Where parameters are the same as a 2D case (Eq. 5.1) except the narrow blade considers the effects of soil motion at the edges of blade that is ignored for wide blade. These factors depend on the soil friction angle, ϕ and the blade rake angle α. In the present study, the value of Q is negligible and the parameters $(N_{\gamma H}, N_{cH}, N_{qH})$ in Eq. 5.7 take the values as shown in Table 5.2. Based on negligible effects of bearing pressure on results of this research work, N_{qH} is neglected in the calculation.

Table 0.2: Soil and blade parameters that are used in the present analysis.

Rake angle $(^\circ)$	$w_1(m)$	$d_1(m)$	$\lambda(\frac{N}{m^3})$	$c(Kpa)$	$N_{\gamma H}$	N_{cH}
60	0.04	0.05	12000	20000	5.27	10.48

Therefore Eq. 5.7 takes the simplified form:

$$F_{DH}^{A} = (\lambda d_1^2 N_{\gamma H} + C d_1 N_{cH}) w_1 = 425N \tag{5.8}$$

The difference in total horizontal blade force between FE results (using regular mesh density model, $F_D = 408N$), and analytical result is found to be about 4%; this can be considered as validation of our FE results.

1.14.2. Experimental validation

1.14.2.1. Filtering and Validating results for the rectangular blade

During motion of the blade through the soil, load cells collected data at a 2.5 millisecond interval and sent them to a data recorder. The recorded signal from load cells is shown in Fig. 5.11. Based on the effect of all the higher natural frequencies of the whole monorail system, the signal was noisy. These recorded signals represent dynamic forces based on the location of load cells as shown in Fig.4.3; however FE results are based on static analysis. Therefore, these signals should be filtered to exclude all system natural frequencies (dynamic effects) which do not effect the draft force and include force frequency (static effects).These recorded signals were related to the experiment with the same rectangular blade dimension as shown in Fig. 4.5 and the rake angle $\alpha = 60^\circ$.

It should be mentioned that the filtered signal must include all forced frequencies on the blade. In order to find the filtering range, the natural frequencies of the blade attached to the monorail (with its tip inside the soil) were determined by applying Fast Fourier Transform (FFT) to two different measurements (the first signal from horizontal load cells, and the second signal using an accelerometer attached to the monorail system). These natural frequencies were excited by hitting the hammer to the blade. The frequency spectra of the system using FFT of the signals from accelerometer and from horizontal load cells are plotted in Fig. 5.12 and 5.13 respectively. As it can be seen the first two natural frequencies are about 21 and 38 Hz, respectively. Then, the spectra of frequency of the system (monorail and frame) were determined using similar measurements and FFT when the blade was moving through the soil with speed of 2 km/h and were plotted in Figures 5.14 and 5.15 using signals from accelerometer and horizontal load cells, respectively. As can be seen from these plots, the first three frequencies are about 1.5, 21 and 40 Hz. Comparing these forced frequencies with the natural frequencies (21 and 38 Hz), it can be concluded that 1.5 Hz is the forced frequency and the other two (21 and 40) are natural frequencies of the system that should be filtered out. Therefore this signal was filtered to exclude all frequencies above 2 HZ. The result is shown in Fig. 5.16 with a solid line. As can be seen, beyond the initial phase, the draft force stayed almost constant at a value of 415 N.

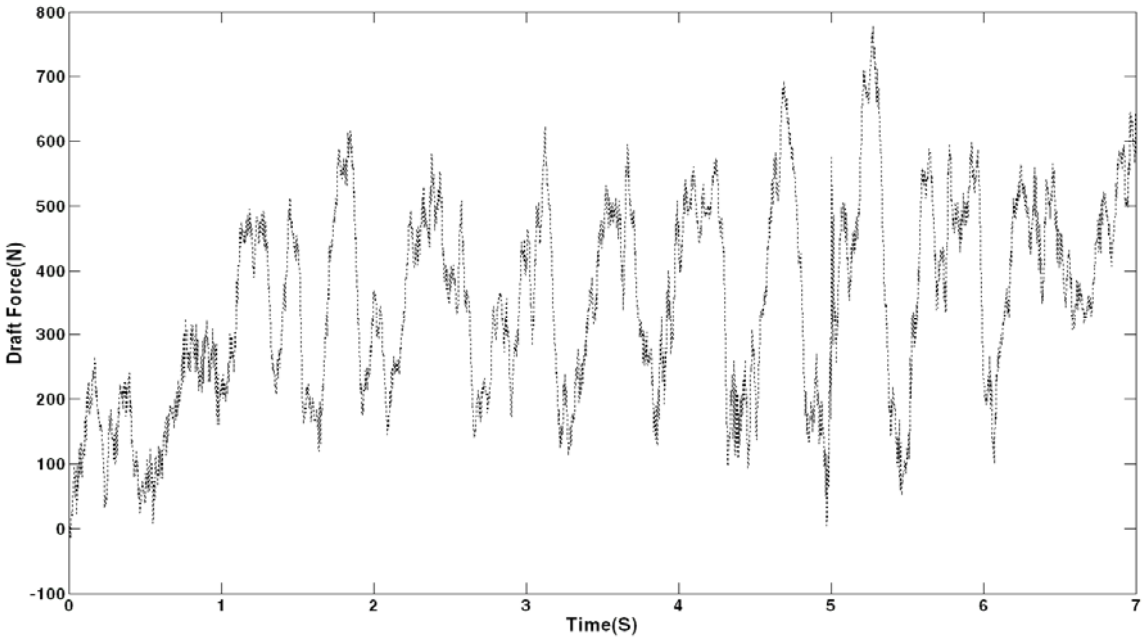

Figure 0.11: Unfiltered horizontal (draft) force on the blade when moving with 60° rake angle

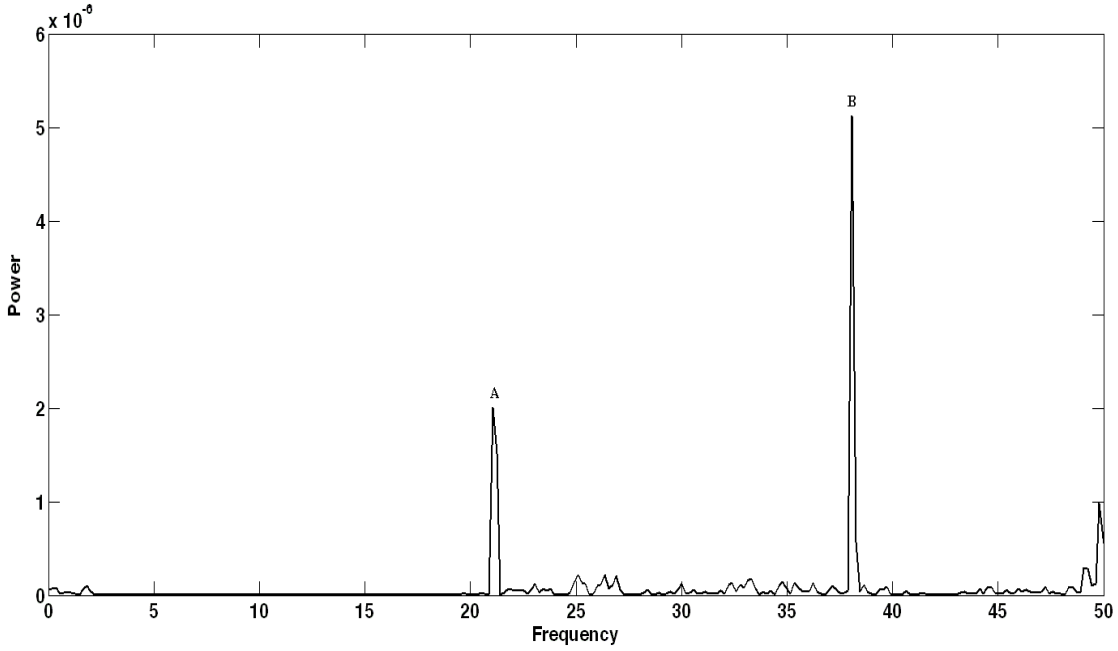

Figure 0.12: The spectrum of natural frequencies of the system (the signal from accelerometer, A=21.06, B=38.09 Hz)

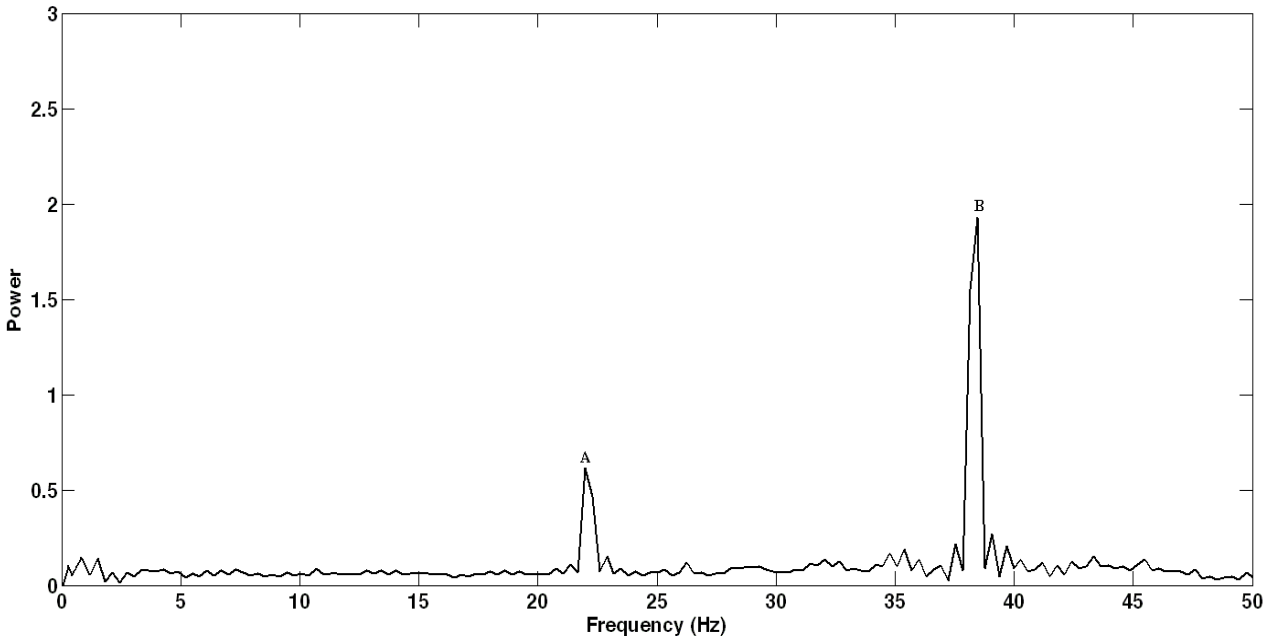

Figure 0.13: The spectrum of natural frequencies of the system (the signal from horizontal load cells, A=21.97, B=38.45 Hz)

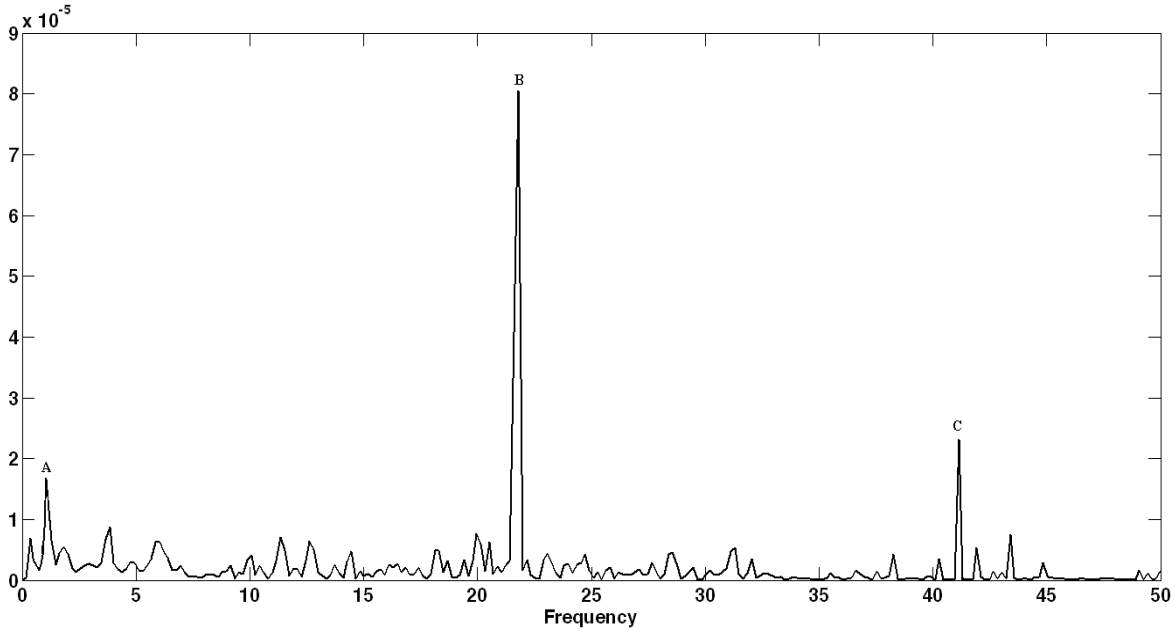

Figure 0.14: The spectrum of frequencies of the moving system (the signal from accelerometer, A=1.1, B=21.7, C=41.2 Hz)

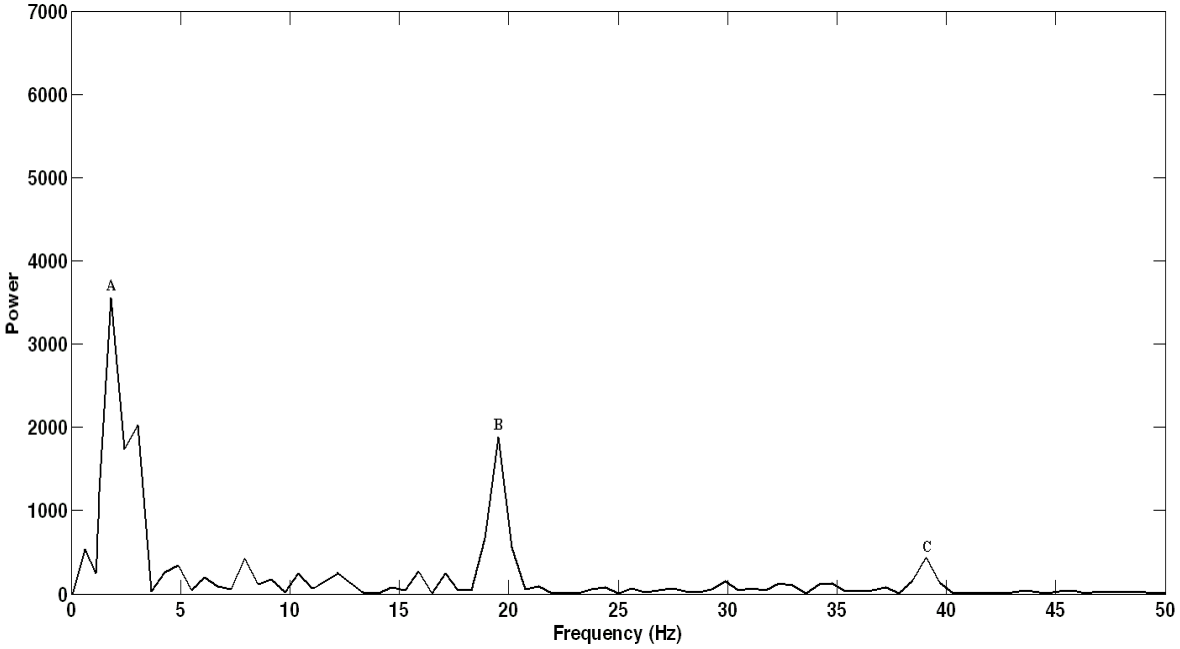

Figure 0.15: The spectrum of frequencies of the moving system (the signal from horizontal load cells A=1.8, B=19.5, C=39.0 Hz)

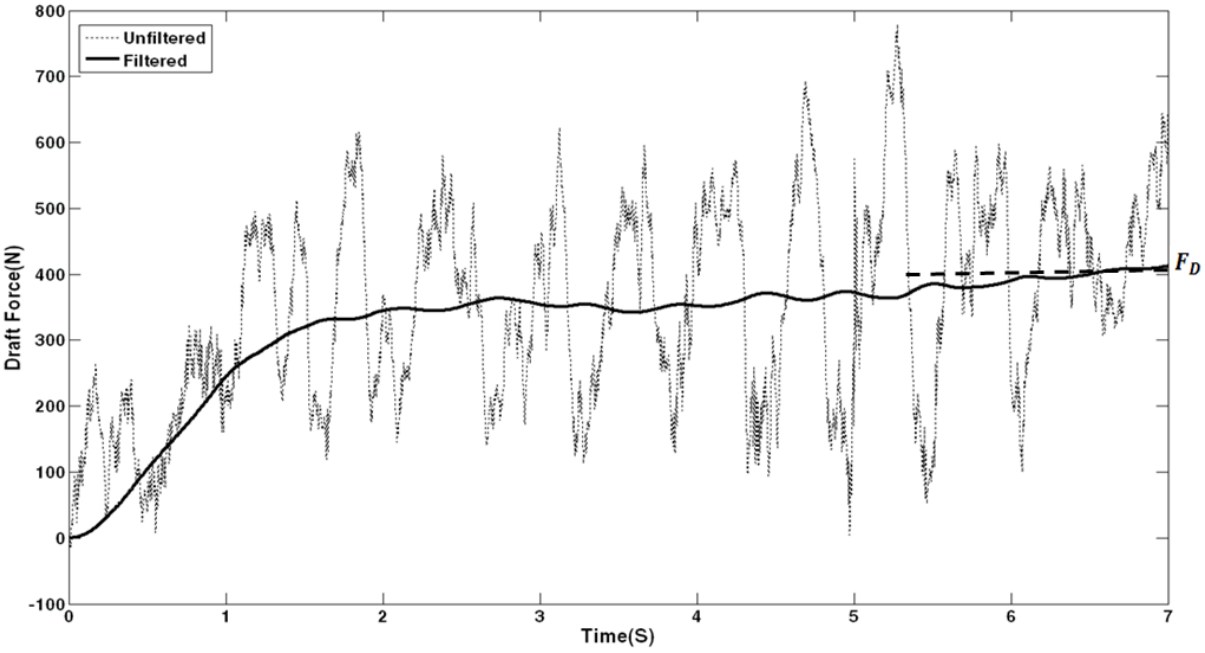

Figure 0.16: Unfiltered and filtered horizontal blade (draft) force on the blade when the blade moves through soil

The experimental results are compared with the analytical and FE results as shown in Table 5.3. The difference between analytical and experimental results is 2.3%, and the difference between FE and experimental results is 1.6% which shows good correlations between these three methods. Therefore our FE model is validated with both analytical and experimental ones.

Table 0.3: Comparing the experimental, analytical, and FE results.

$d_1(m)$	$w_1(m)$	Analytical force, $F_D(N)$	FE force, $F_D(N)$	Experimental Force, $F_D(N)$
50	40	425.0	408.0	415
Difference between analytical and experimental (%)			Difference between FE and experimental (%)	
2.3			1.6	

1.14.2.2. Validating results for the triangular blade

In order to validate the FE model for triangular blades, the draft forces of such a blade with four different rake angles $\alpha = 45^\circ, 60^\circ, 75^\circ$ and 90° are calculated. It should be noted that blades in these models are straight, which means $\alpha = \alpha_c$, and the sharpness angles in all models were $\alpha = 53^\circ$. These four cases are modeled with the element size *e* = 7.5*mm* which is obtained the same way as in Sec. 5.1. A typical plot of the blade forces calculated by the procedure presented in the previous section and the average forces plot $\overline{F}$ are shown in Figs. 5.17 and 5.18. The average forces $\overline{F}$ are almost horizontal after the second iterations already, and the corresponding draft forces are $F_D = 172N,\ 275N,\ 326N$ and $425N$ for rake angles $\alpha = 45^\circ,\ 60^\circ,\ 75^\circ$ and 90° respectively. Based on Fig. 5.18, one can conclude that a more inclined blade (with smaller rake angle α) has less draft force which is similar to the behavior of rectangular shaped blades. Since the available analytical solutions are limited to rectangular blades, these results are verified only experimentally.

Same as in the experiments for rectangular blade, all the tests were performed at a speed of 0.56 *m/s* (2 km/h). The blade size and depth of blade inside the soil in the experiments were identical to those used in the FE simulations as shown in Figs. 3.17 and 4.6. As mentioned before, each experiment started after placing the blade at the required depth $(d_1 = 5cm)$. The horizontal forces on the blade for four different blade's rake angle ($\alpha = 45^\circ,\ 60^\circ,\ 75^\circ$ and 90° plotted in Figs. 5-19) were measured by summing the results from two horizontal load cells. During motion of the blade, the load cells collected data at 2.5 millisecond intervals and sent them to a data recorder. Based on what was discussed in previous section (Sec.5.4.2.1), the recorded signal (dotted line in Figs. 5.19-5.22) was noisy because all the higher natural frequencies of the monorail system were registered; therefore this signal was filtered to exclude all frequencies above 2 Hz to eliminate natural frequencies and keep the forced frequency. As can be seen, beyond the initial phase, the blade forces in Figs. 5.19-5.22 which are shown as a solid line, stayed almost constant at values of around 181 *N*, 289 *N*, 337 *N*, and 431 *N* respectively.

The experimental results are compared with FE results as shown in Table 5.4. The difference between FE and experimental results are less than 5% in all cases that shows good correlations between these methods. It should be mentioned that by increasing compacting strain limit ε_c, the FE draft force results will increase and the difference between FE and experimental results will decrease. Also as shown in Figs.5.19- 5.22, the more inclined blade has more vibration which the error of finding average draft force will increase consequently that is shown in Table 5.4. Therefore the FE model for triangular blade is validated with the experimental method.

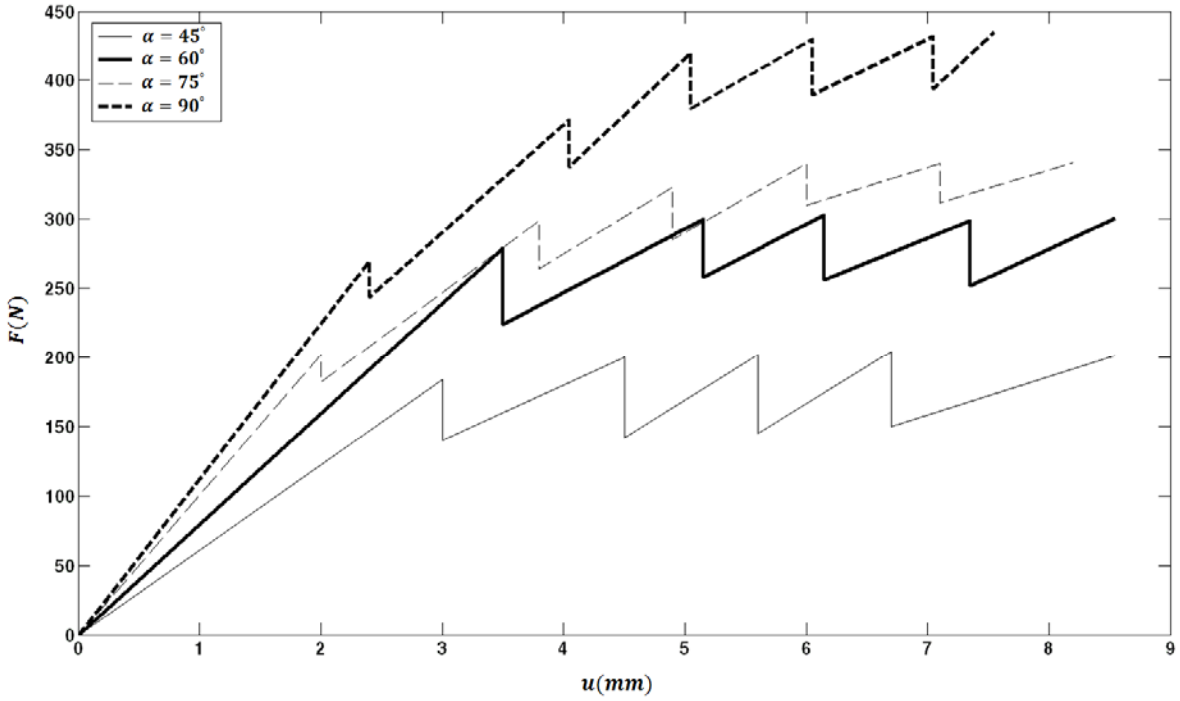

Figure 0.17: Variation of blade (draft) forces for different triangular blade's rake angles.

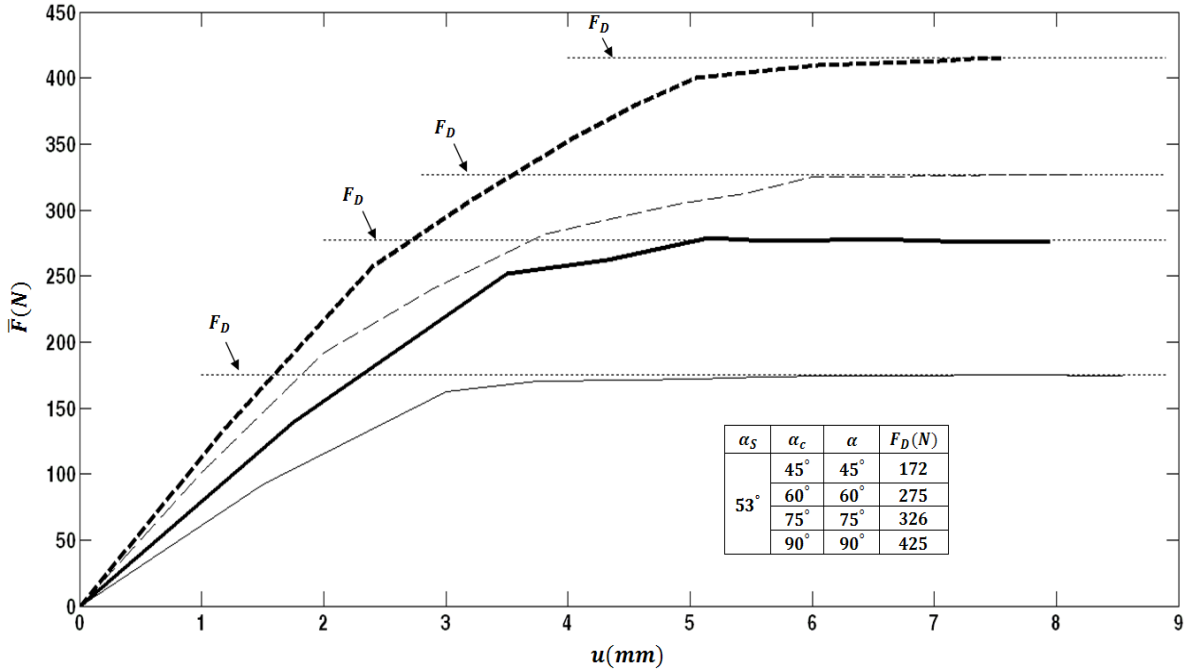

Figure 0.18: Variation of the averaged blade (draft) forces for different triangular blade's rake angles

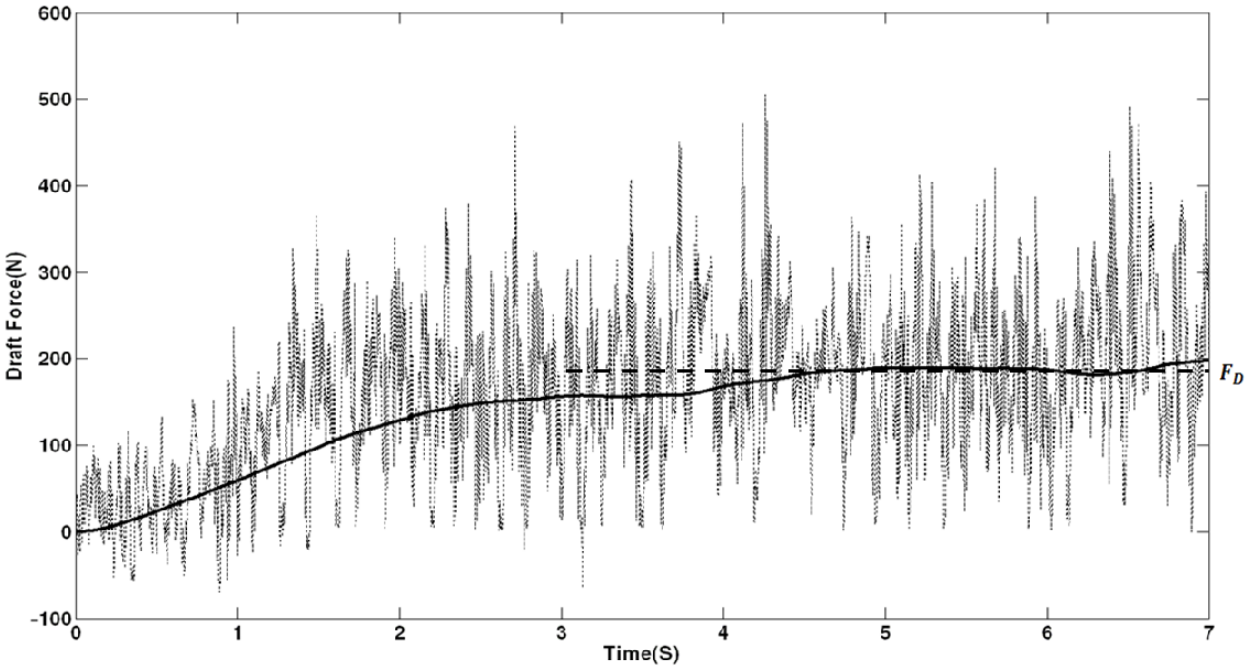

Figure 0.19: Unfiltered and filtered horizontal blade (draft) force on the blade for 45° rake angle and $\alpha_S = 53^\circ$

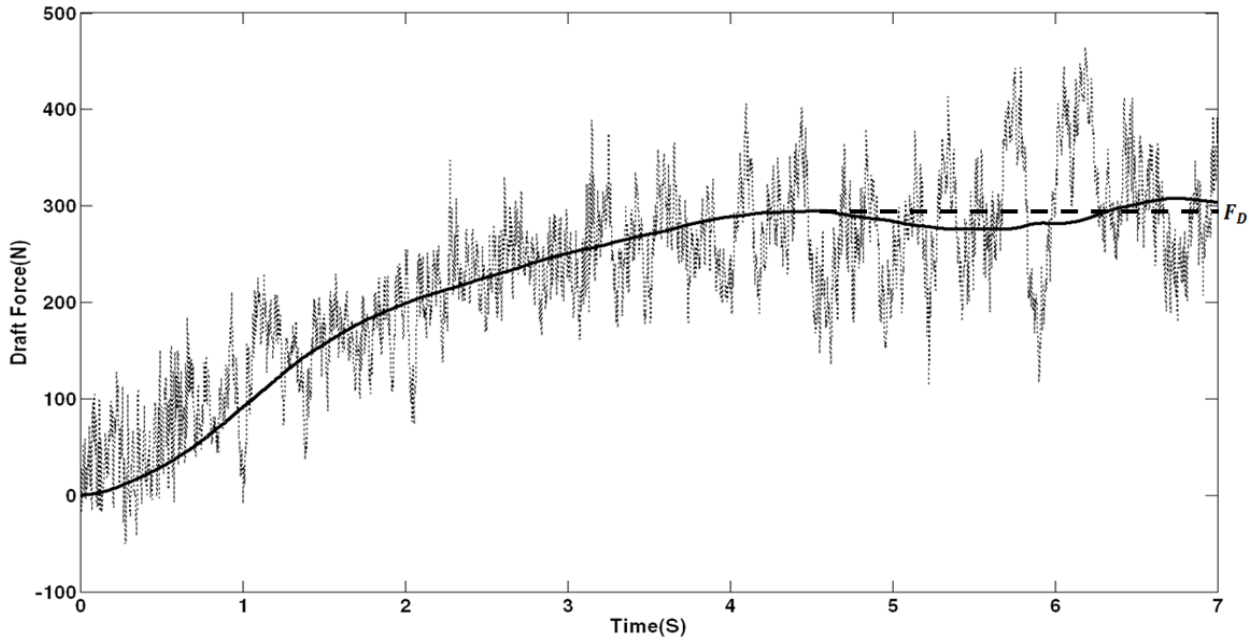

Figure 0.20: Unfiltered and filtered horizontal blade (draft) force on the blade of 60° rake angle and $\alpha_S = 53^\circ$

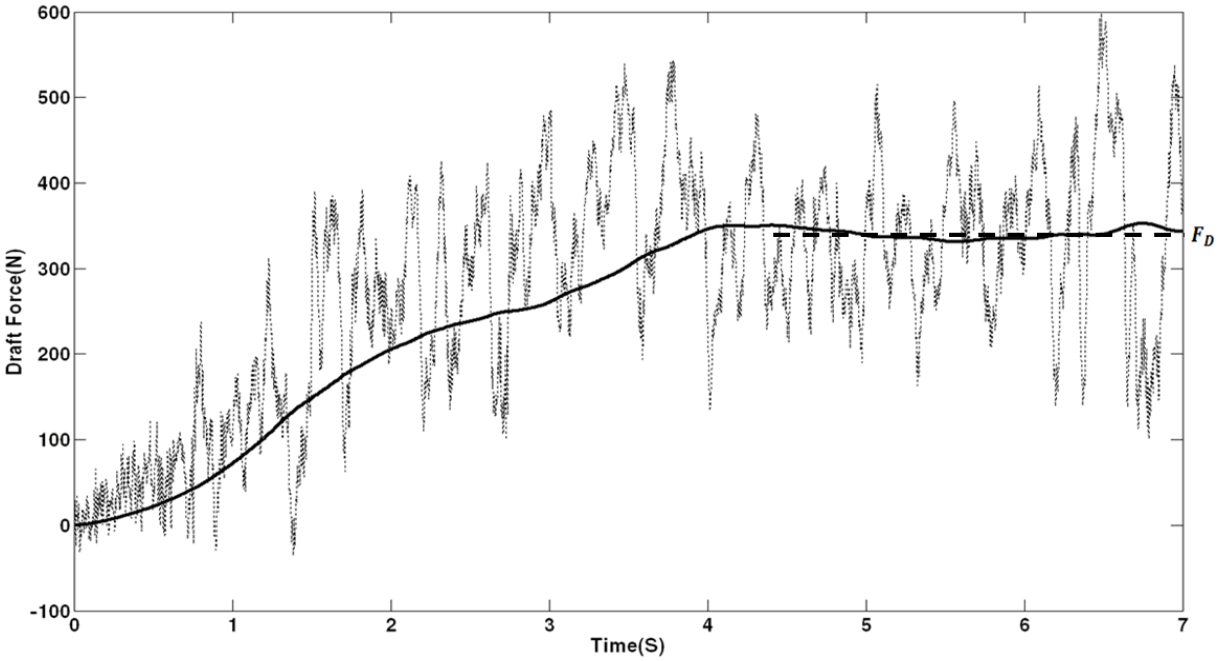

Figure 0.21: Unfiltered and filtered horizontal blade (draft) force on the blade of 75° rake angle and $\alpha_S = 53^\circ$

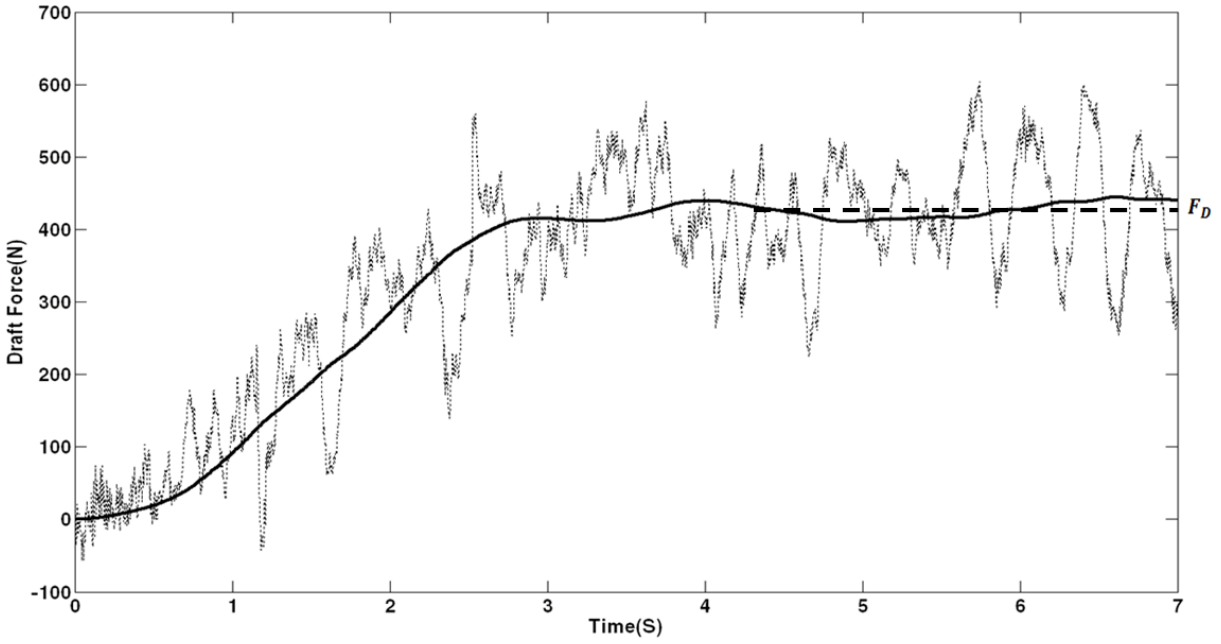

Figure 0.22: Unfiltered and filtered horizontal (draft) force on the blade of 90° rake angle and $\alpha_S = 53^\circ$

Table 0.4: Comparing the experimental and FE results.

α_S	α_c	α	FE force, $F_D(N)$	Experimental force, $F_D(N)$	Difference (%)
53°	45°	45°	172	181	4.9
	60°	60°	275	289	4.8
	75°	75°	326	337	3.2
	90°	90°	425	431	1.3

1.15. Comparison of rectangular and triangular blades

In order to compare the triangular blade with the rectangular one, FE results for the rectangular blade with the same width and depth of interaction as shown in Fig. 5.23 and listed in Table 5.5 are calculated. Results for the rectangular blade were verified analytically based on the analytical method which is limited to a straight rectangular blade, and results for the triangular blade were verified experimentally.

In Fig. 5.24, the FE draft force results of the rectangular blade are compared with analytical results. The maximum difference between these two methods is less than 5% (at $\alpha = 60^\circ$) which generally indicates good correlations. Also the FE force results for the triangular blade are compared with the experimental results for which the maximum differences between the forces are around 8%. As shown in Fig. 5.24, the difference between horizontal forces acting on the triangular blade is around half of the amount of force which acts on the rectangular blade with the same rake angle (i.e. at $\alpha = 45^\circ$, triangular blade force is $F_{DT} = 172N$ and rectangular blade force is $F_{DR} = 368N$ or at $\alpha = 90^\circ$, $F_{DT} = 425N$ while $F_{DR} = 900N$). This means that for the

same width of groove through the soil, triangular blade need much less force than the blade with rectangular shape.

The soil deformation patterns of these two shapes of blades are compared in Fig. 5.25. Also the displacements of soil in front of these two types of blades were compared in Fig. 5.26. For the rectangular blade, the soil is accumulated in front of the blade and tends to swell up in an upward direction and lateral directions with respect to its original configuration in a pattern similar to that indicated in Shmulevich et al. [26]. However for the triangular blade, the soil is pushed mostly in lateral directions and slightly accumulated in front of the blade as shown in Figs. 5.26.

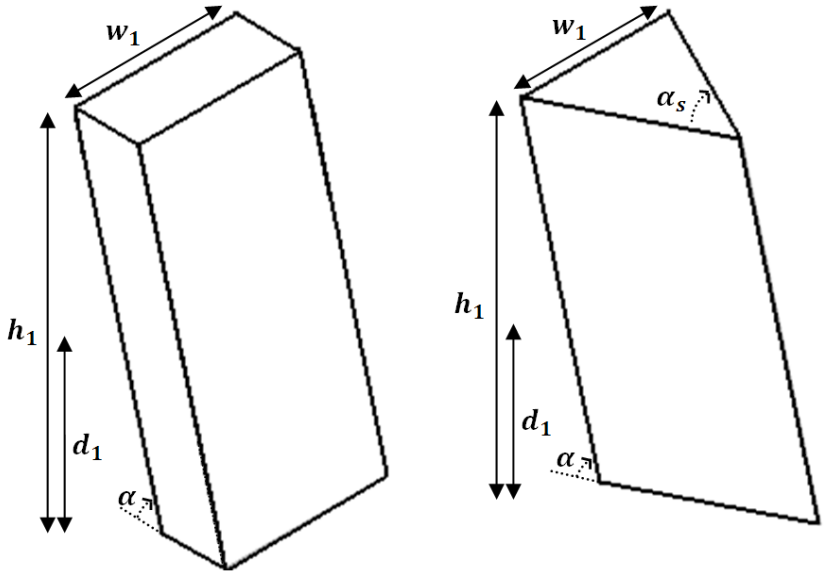

Figure 0.23: 3D model dimensions for rectangular and triangular narrow blades (these parameters are defined in Sec. 3.3.1.1 and 3.3.1.3)

Table 0.5: Blade model dimensions that are used in FEA

parameters	$w_1(mm)$	$h_1(mm)$	$d_1(mm)$	$\alpha(^\circ)$	$\alpha_S(^\circ)$
Values	50	100	50	45, 60, 75, 90	53

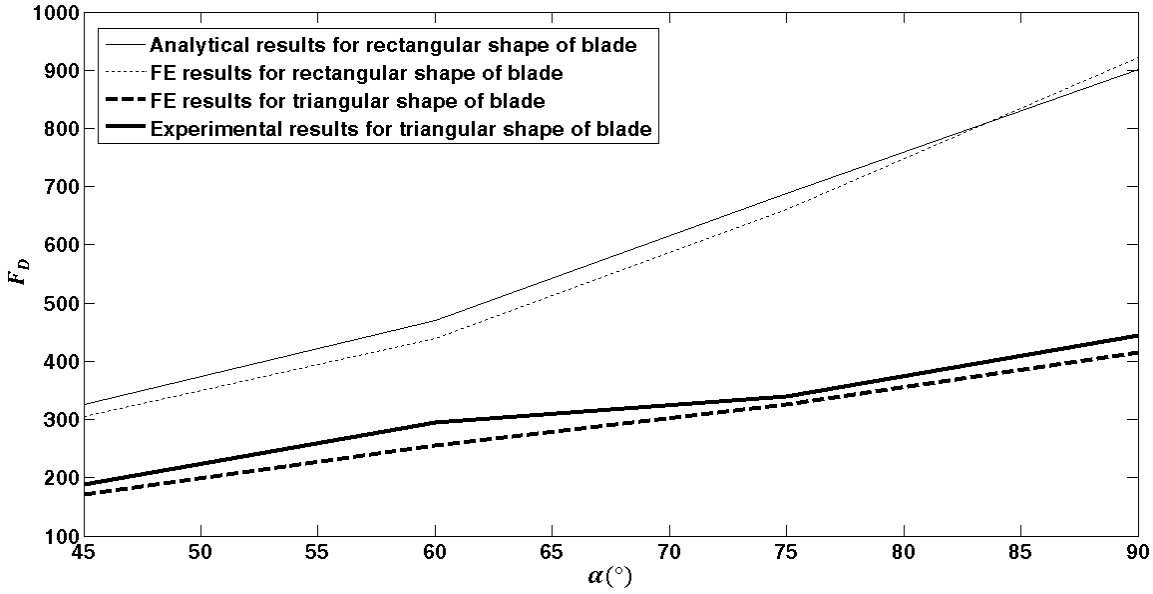

Figure 0.24: Comparing draft forces of rectangular vs. triangular blades (different blade's rake angle)

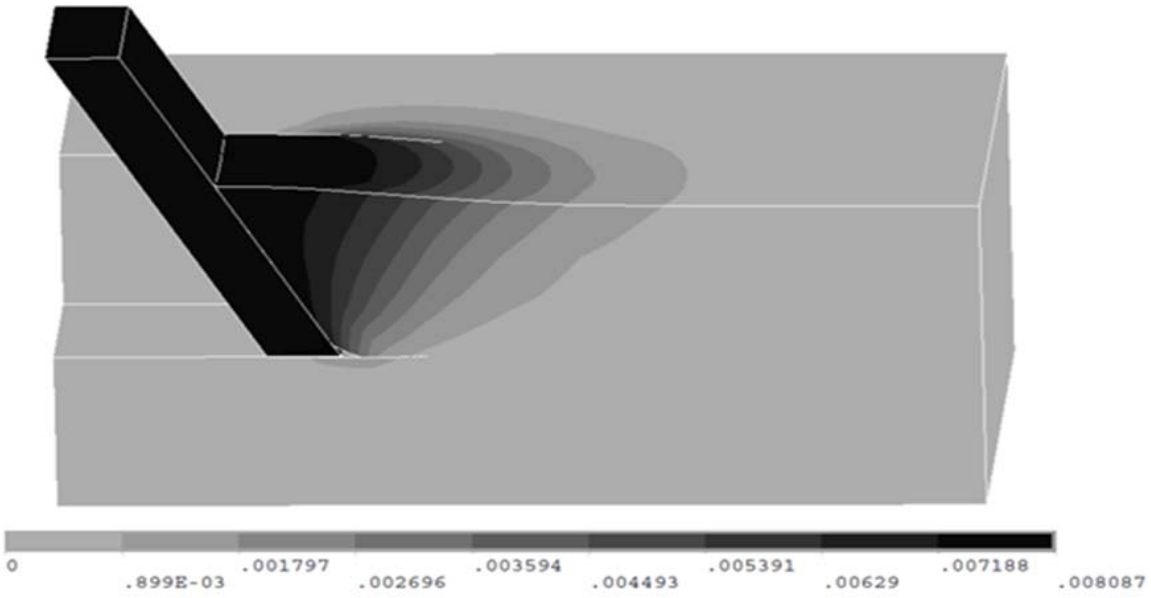

(a)

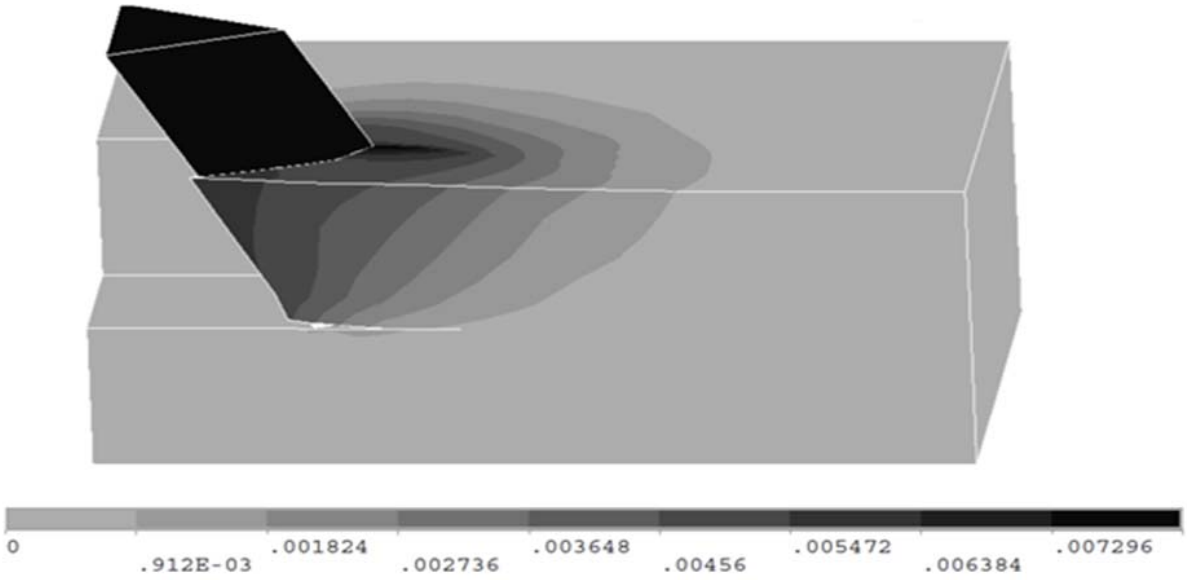

(b)

Figure 0.25: Soil deformation patterns for the rectangular (a) and the triangular (b) blades (for blade's rake angle $\alpha = 60^{\circ}, \alpha_S = 53^{\circ}$)

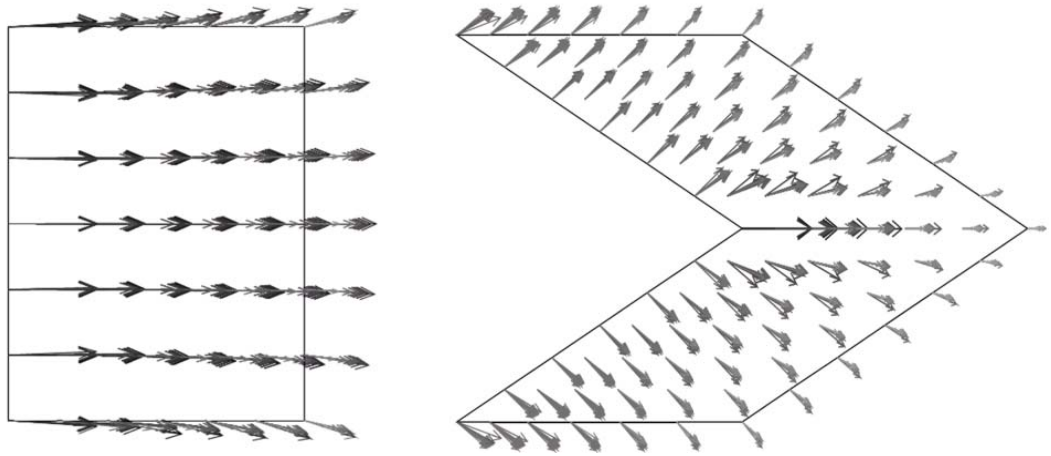

(a) (b)

Figure 0.26: Displacement pattern in soil for the rectangular (a) and the triangular (b) blades (for blade's rake angle $\alpha = 60^{\circ}$)

1.16. Effect of blade width, depth and rake angle on draft force for rectangular blades

The FE model for the rectangular blade was used to investigate the effects of the depth of blade in the soil (d_1) and width of blade (w_1) on the draft force F_D. The geometrical parameters and the results are listed in Table 5.6. Also the analytical results calculated from Eq. 5.7 are shown for comparison. As can be seen the agreement is within about 5%, which should be considered acceptable.

Table 0.6: comparing analytical and FEA results for 8 different models (blade's rake angle $\alpha = 60^\circ$)

$d_1(mm)$	$w_1(mm)$	w_1/d_1	Analytical force, $F_D(N)$	FEA force, $F_D(N)$	Percentage Difference (%)
25	6.3	0.25	90.00	87.00	3.3
25	20	0.8	105.0	109.0	3.6
25	25	1.0	116.0	121.0	4.1
25	75	3.0	231.0	242.0	4.5
50	12.5	0.25	364.0	351.0	3.5
50	40	0.8	425.0	408.0	3.9
50	50	1.0	470.0	446.0	4.8
50	150	3.0	933.0	965.0	3.3

The FE results are also plotted in Fig. 5.27. The blade force increases with increasing w_1/d_1, Also, by doubling the blade depth in soil, and keeping w_1/d_1 constant, the blade force increases

approximately 4 times (e.g. F increases from 87 N to 351 N for w_1/d_1 =0.25 when d_1 increased from $25mm$ to $50mm$).

Fig. 5.28 shows the blade's force for eight different cases with two different blade's depths. As can be seen by doubling the working depth of the blade (d_1) and keeping its width (w_1) constant the blade force triples (e.g. F increases from 142 N to 408 N for $w_1 = 40mm$ and d_1 changing from $25mm$ to $50mm$).

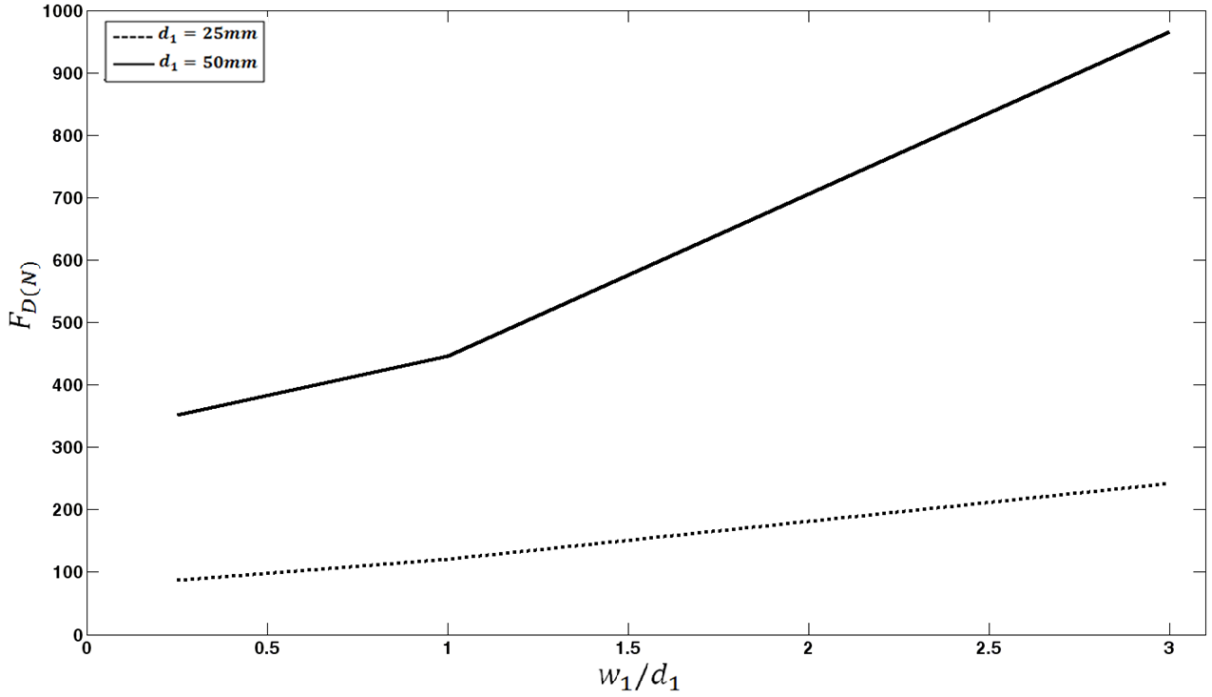

Figure 0.27: The draft force (F_D) for constant depth and different ratio w_1/d_1

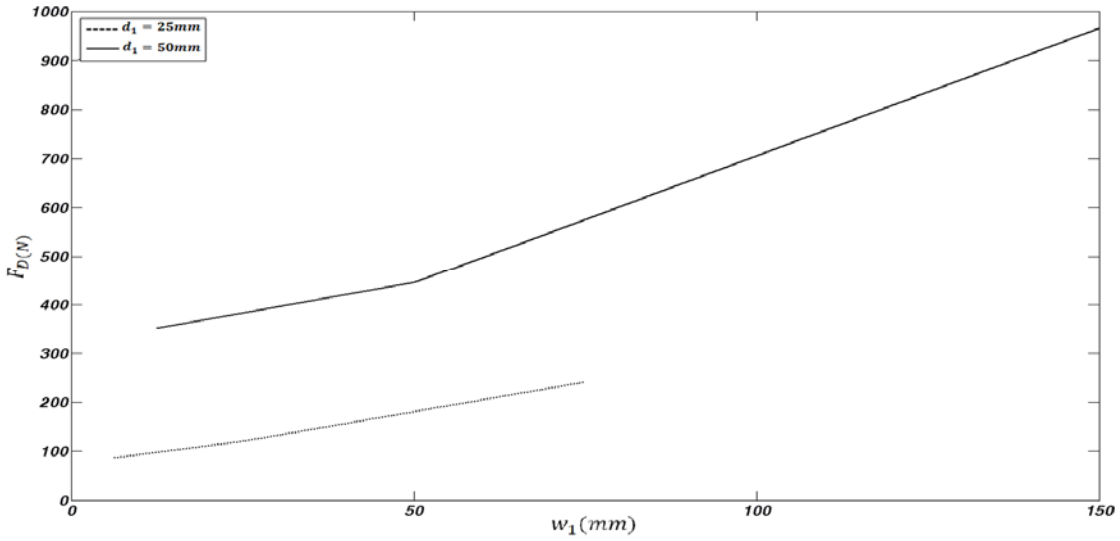

Figure 0.28: The draft force (F_D) for constant depth and differing blade width.

In order to investigate effects of the blade's rake angle on the draft force the procedure was used for $\alpha = 90^\circ$, 60° and 30° with the results listed in Table 5.7 and plotted in Fig. 5.29. By increasing the blade's rake angle, the effect of sliding between soil and blade decreases; but on the other hand the effects of compression and cohesion between soil particles increases which is resulted in increasing blade's draft force.

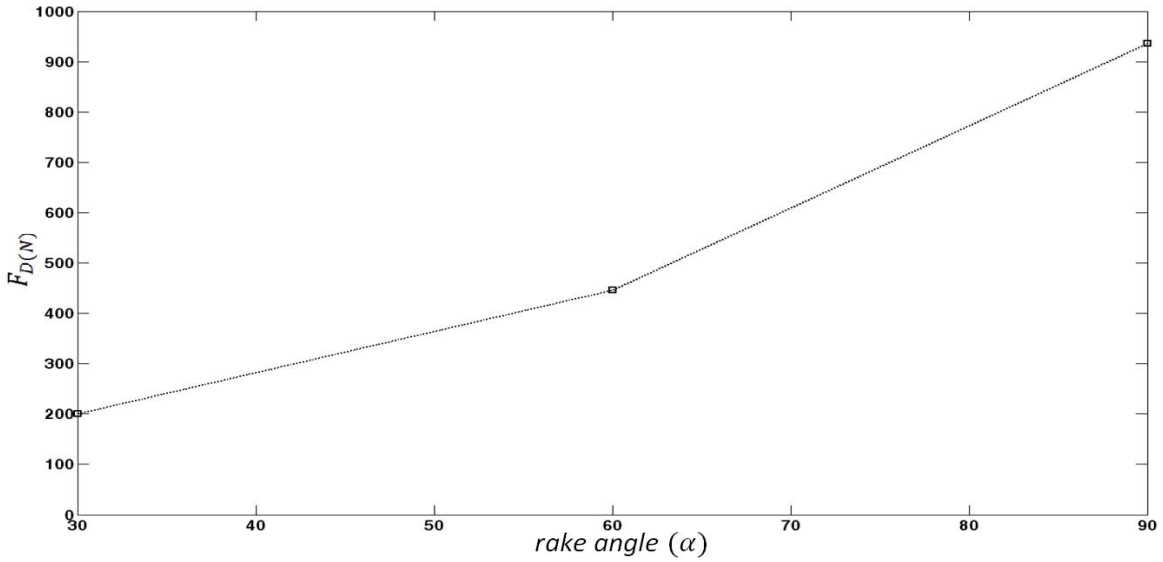

Figure 0.29: FEA results: The blade force for constant width and different rake angle.

Table 0.7: Comparing analytical and FE results for 3 different models (effect of rake angles)

$d_1(mm)$	$w_1(mm)$	$\alpha(^\circ)$	Analytical force, $F_D(N)$	FE force, $F_D(N)$	Percentage Difference (%)
50	50	90	900.0	942.0	4.4
50	50	60	470.0	446.0	4.8
50	50	30	188.0	201.0	6.4

1.17. Force results and discussion for curved shape blade

1.17.1. Effects of changing blade's radius of curvature (at a constant rake angle)

In this section, the effects of changing blade's radius of curvature (at a constant rake angle) on blade draft force for both types of blades (rectangular and triangular) are studied. For each case, three FE models with different radii of curvature are considered and the FE results are compared to investigate the effects of these changes.

1.17.1.1. Rectangular blade

Three FE models are studied in order to investigate the effects of changing the radius of curvature of the blade while keeping the rake angle constant. The shapes of curved blades are indicated in Figs. 5.30(a) - 5.30(c) and are controlled by the angle α_c that increases from 60° to 90°. As shown in Fig. 5.31 and 5.32, variation and average draft forces for these three models are obtained based on the previous FE procedure. From these figures it is obvious that by decreasing the radius (or increasing the curvature) while keeping the rake angle constant the blade force increases. It should be noted that also the blade's average rake angle α_{avg} is increasing from 60° to 75°. Fig. 5.33 depicts how this parameter affects the blade force that increases from 440 *N* to 605 *N*; a more inclined blade requires less draft force.

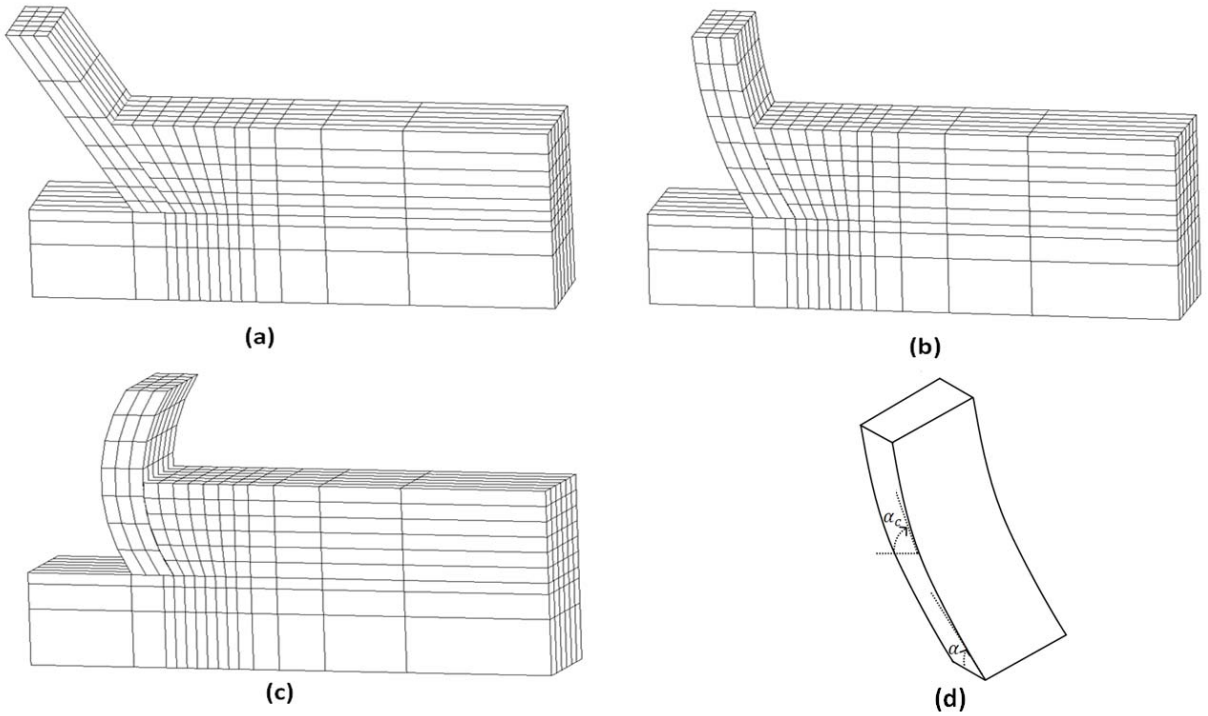

Figure 0-30: FE models for $\alpha = 60^\circ$ and differing α_c: (a) $\alpha_c = 60^\circ$, (b) $\alpha_c = 75^\circ$, (c) $\alpha_c = 90^\circ$, (d) definition of α and α_c (taken from Fig. 3.13)

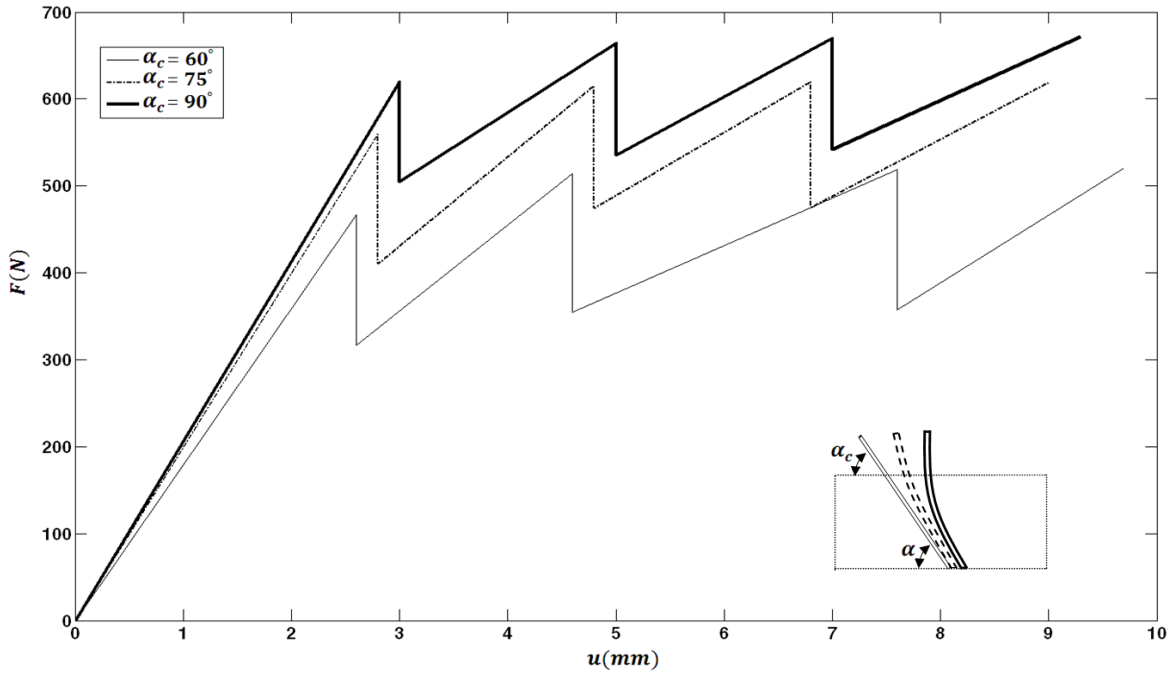

Figure 0.31: Variation of blade (draft) forces for differing α_c and the rake angle $\alpha = 60^\circ$.

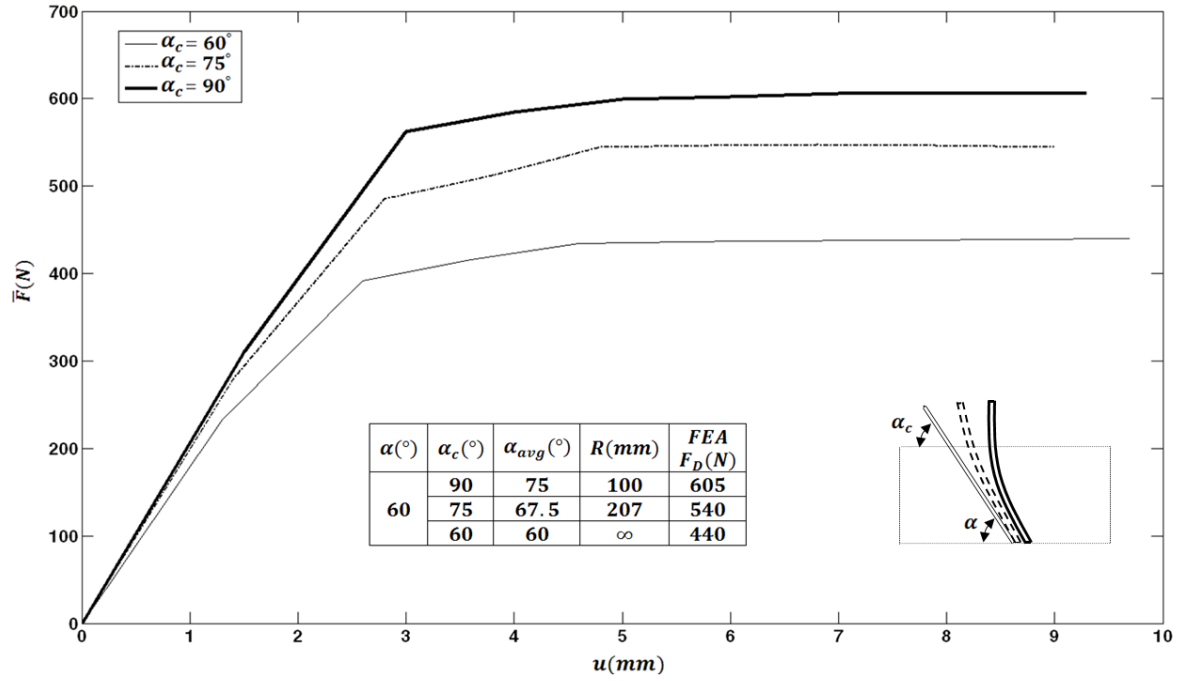

$\alpha(^\circ)$	$\alpha_c(^\circ)$	$\alpha_{avg}(^\circ)$	$R(mm)$	FEA $F_D(N)$
60	90	75	100	605
	75	67.5	207	540
	60	60	∞	440

Figure 0.32: Variation of the average blade (draft) forces for different α_c and the rake angle $\alpha = 60^\circ$

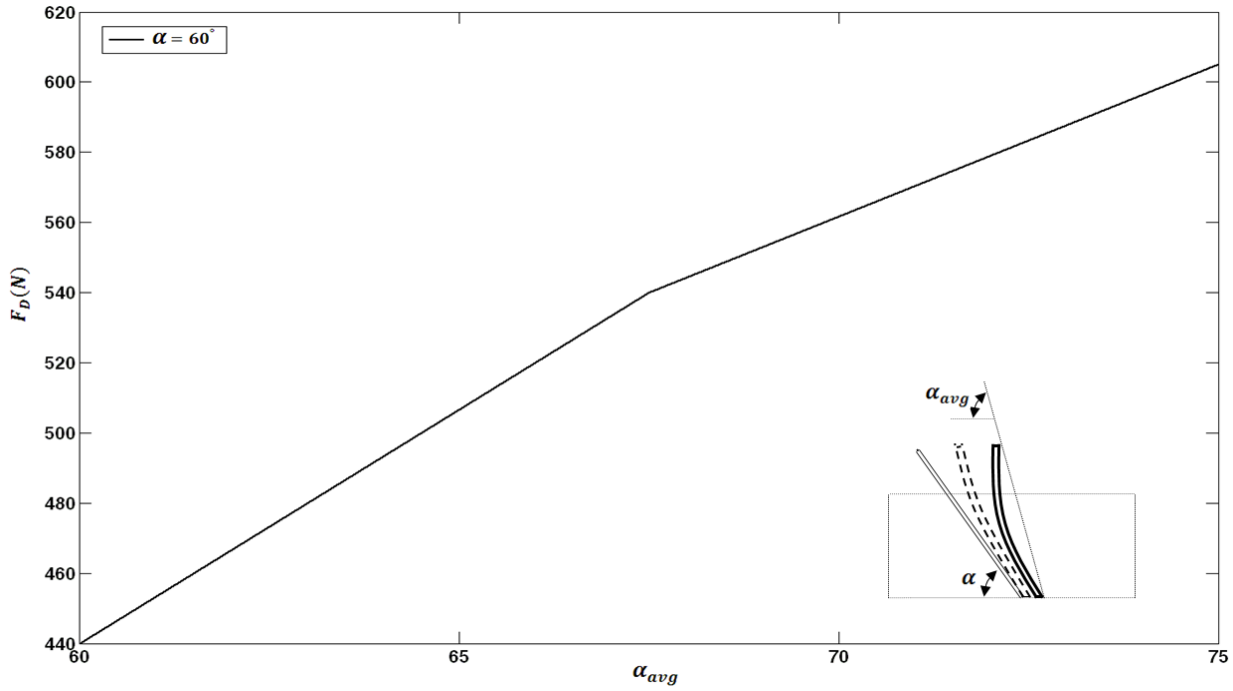

Figure 0.33: Variation of the blade (draft) forces with differing blade's average rake angles for $\alpha = 60^\circ$.

1.17.1.2. Blades of triangular shapes

Same as the rectangular case, three FE models were studied for the triangular blade in order to investigate the effects of changing the radius of curvature of the blade while keeping the rake angle constant. The shapes of curved blades as shown in Fig. 5.34 are controlled by the angle α_c that increases from 60° to 90°, while the rake angle $\alpha = 60^\circ$ is constant. From Figs. 5.35, and 5.36, it is obvious that by decreasing the radius (or increasing the curvature) while keeping the rake angle constant the blade force increases, which is similar to the rectangular blade case. Same as what is concluded from curved rectangular blades, this increase in draft force is significantly related to the blade's average rake angle α_{avg}, by increasing this angle, the draft force increase. As shown in Fig. 5.36, by increasing α_{avg} from 60° to 67.5°, the draft force

increase from 275*N* to 295*N*, and by increasing α_{avg} from 67.5° to 75°, the draft force increases from 295*N* to 326*N;* a more inclined blade requires less draft force. By comparing Fig. 5.33 for the rectangular blade and Fig 5.36 for the triangular blade, it seems that the curved force results for triangular blades are almost half of the force results for rectangular ones which mean that for the same width of groove, the triangular curved blade needs need less force than rectangular ones.

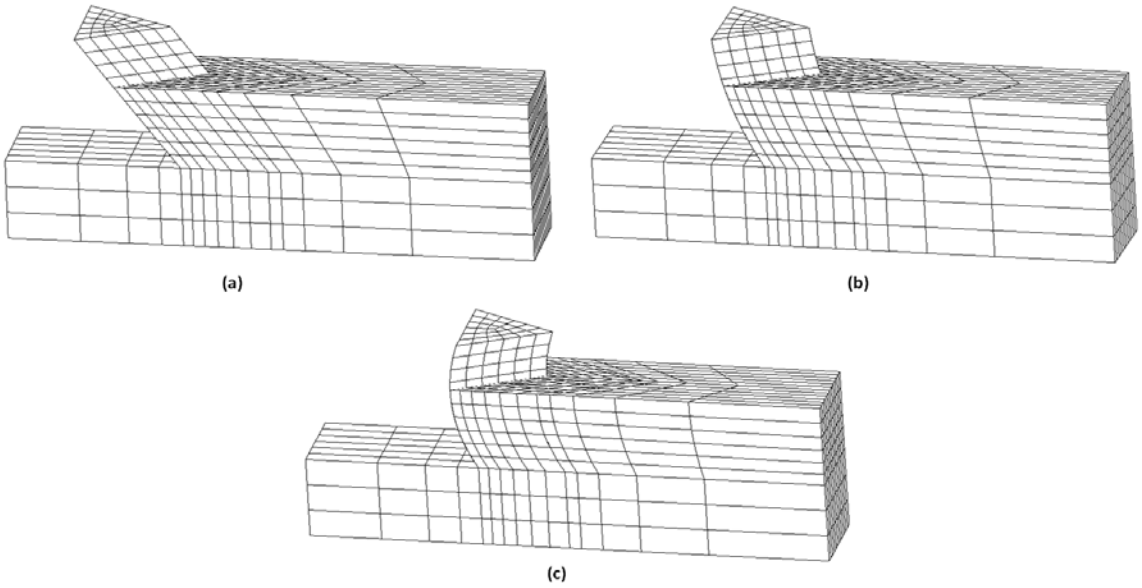

Figure 0.34: FE model for 3D soil interaction with the triangular blade while rake angle is constant, $\alpha = 60^\circ$ and blade's curvature angles are different, (a) $\alpha_c = 60^\circ$, (b) $\alpha_c = 75^\circ$, (c) $\alpha_c = 90^\circ$

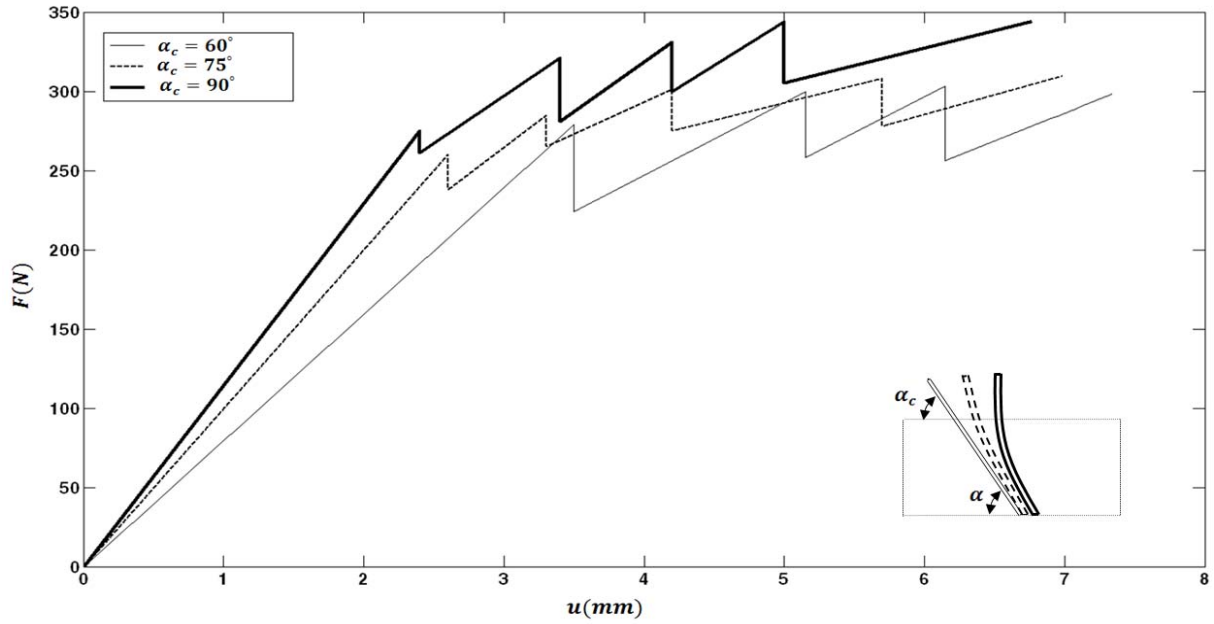

Figure 0.35: Variation of blade (draft) forces for different curvature angles α_c with constant rake angle $\alpha = 60^\circ$.

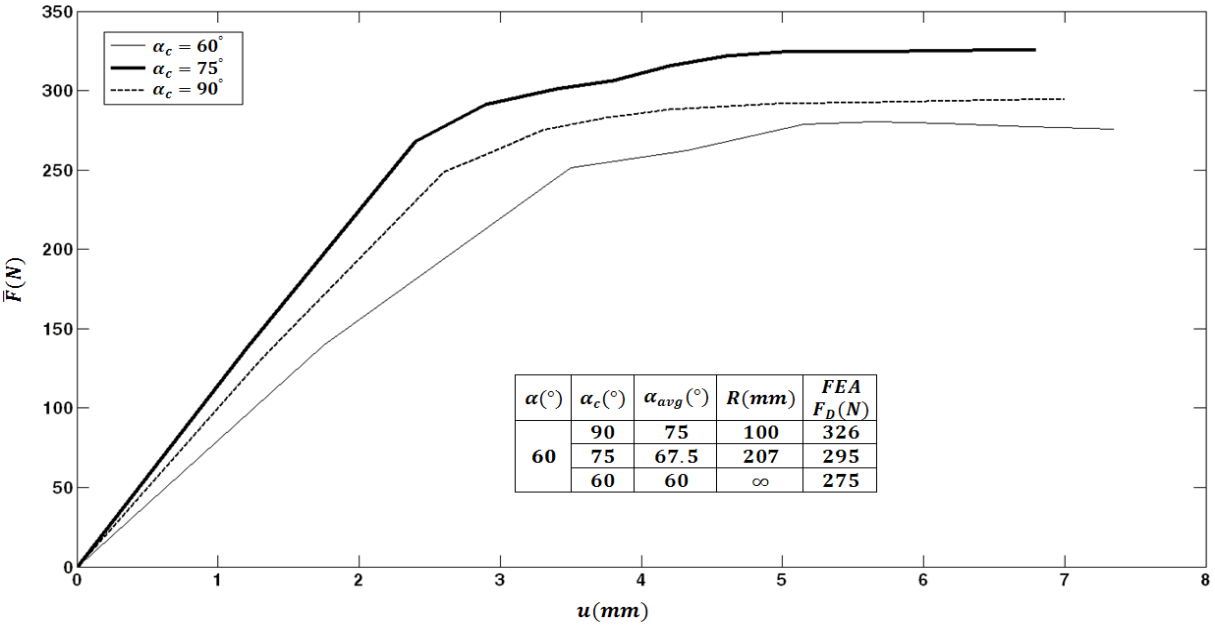

$\alpha(^\circ)$	$\alpha_c(^\circ)$	$\alpha_{avg}(^\circ)$	$R(mm)$	FEA $F_D(N)$
60	90	75	100	326
	75	67.5	207	295
	60	60	∞	275

Figure 0.36: Variation of the average blade (draft) forces for different curvature angles α_c with constant rake angle $\alpha = 60^\circ$.

1.17.2. Effects of changing blade's radius of curvature with constant α_c

In this section, the effects of changing blade's radius of curvature with constant α_c on blade draft force for both types of blades (rectangular and triangular shape blades) are studied. For the rectangular case, nine FE models, and for triangular one, three the FE models with different radius of curvature are considered. Subsequently the FE results are compared to investigate the effects of these changes.

1.17.2.1. Rectangular blade

The effects of changing rake angle while keeping the angle α_c constant are investigated using the FE models shown in Figs. 5.37, 5.38, and 5.39. Variation and average draft forces for these three models are obtained based on the discussed FE procedure and draft forces for these nine models are listed in Fig. 5.40 and listed in Table 5.8.

As shown in Fig. 5.40, by increasing the rake angle α at the angle α_c constant, the blade draft force increases in all three cases with constant α_c. Same as in the previous section, it can be explained by the increase of the blade's average rake angle, α_{avg} or by the increase in the blade's curvature. The relationship of the draft forces to the angle α_{avg} are plotted in Fig. 5.41. As shown in this figure, by increasing α_{avg} from 47.5° to 90°, the draft force increase from $268N$ to $920N$ which indicate that more inclined curved blade requires less draft force.

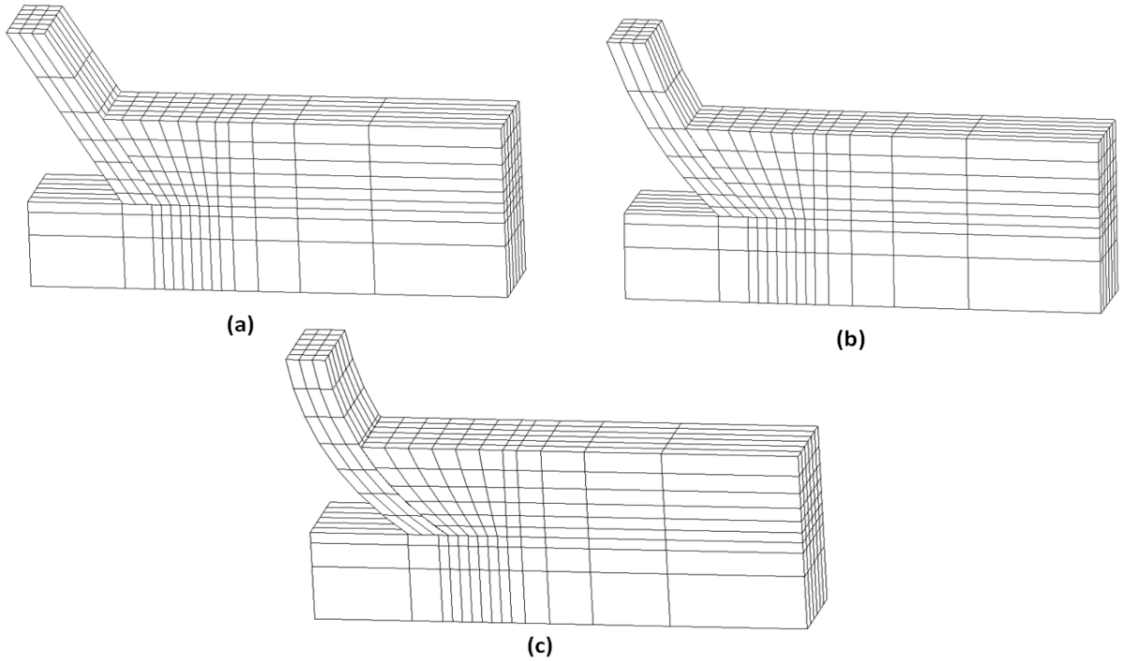

Figure 0.37: FE models for $\alpha_c = 60^\circ$ and different rake angles, (a) $\alpha = 60^\circ$, (b) $\alpha = 45^\circ$, (c) $\alpha = 35^\circ$.

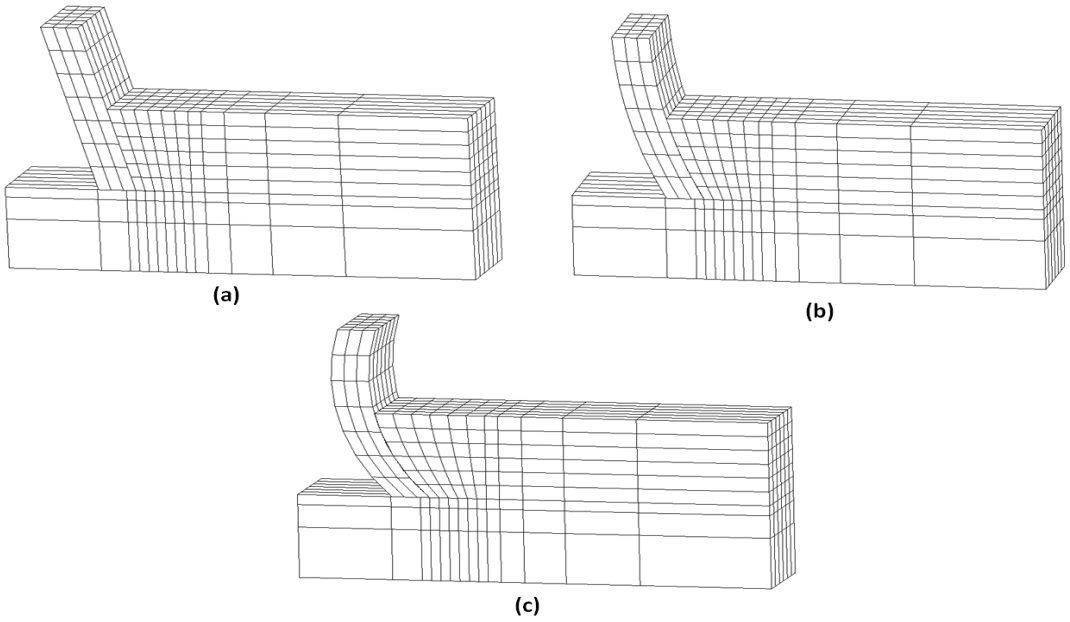

Figure 0.38: FE models for $\alpha_c = 75^\circ$ and different rake angles, (a) $\alpha = 75^\circ$, (b) $\alpha = 60^\circ$, (c) $\alpha = 45^\circ$.

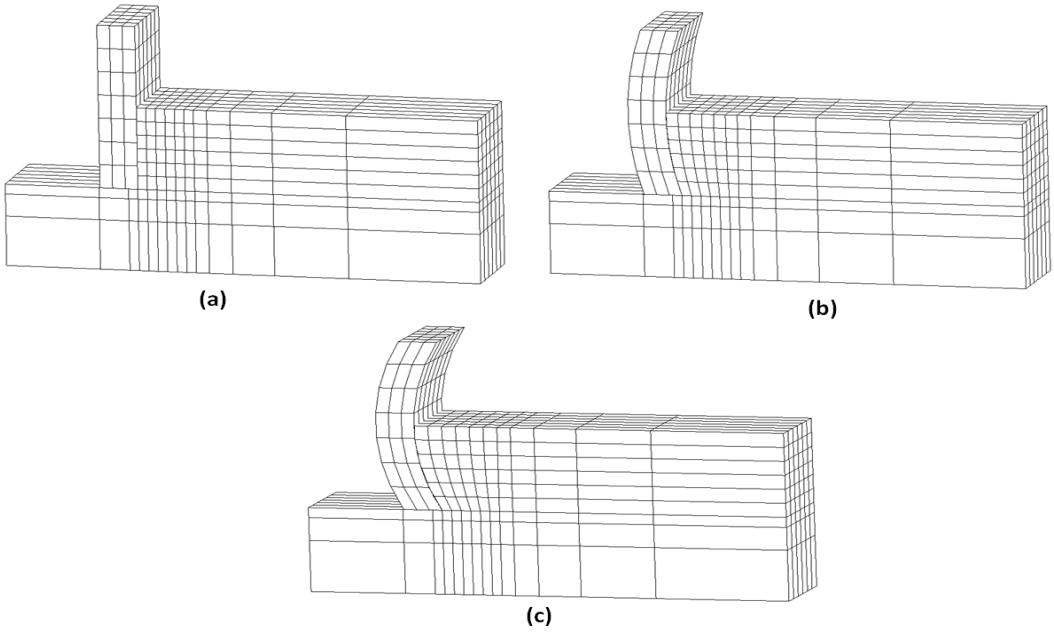

Figure 0.39: FE models for $\alpha_c = 90^\circ$ and different rake angles, (a) $\alpha = 90^\circ$, (b) $\alpha = 75^\circ$, (c) $\alpha = 60^\circ$.

Table 0.8: Draft forces F_D for nine different FE models with different rake angles (α) and three constant curvature angles (α_c).

α_c	α	$F_D(N)$ from FE models
60	60	440
	45	317
	35	268
75	75	640
	60	540
	45	440
90	90	920
	75	753
	60	640

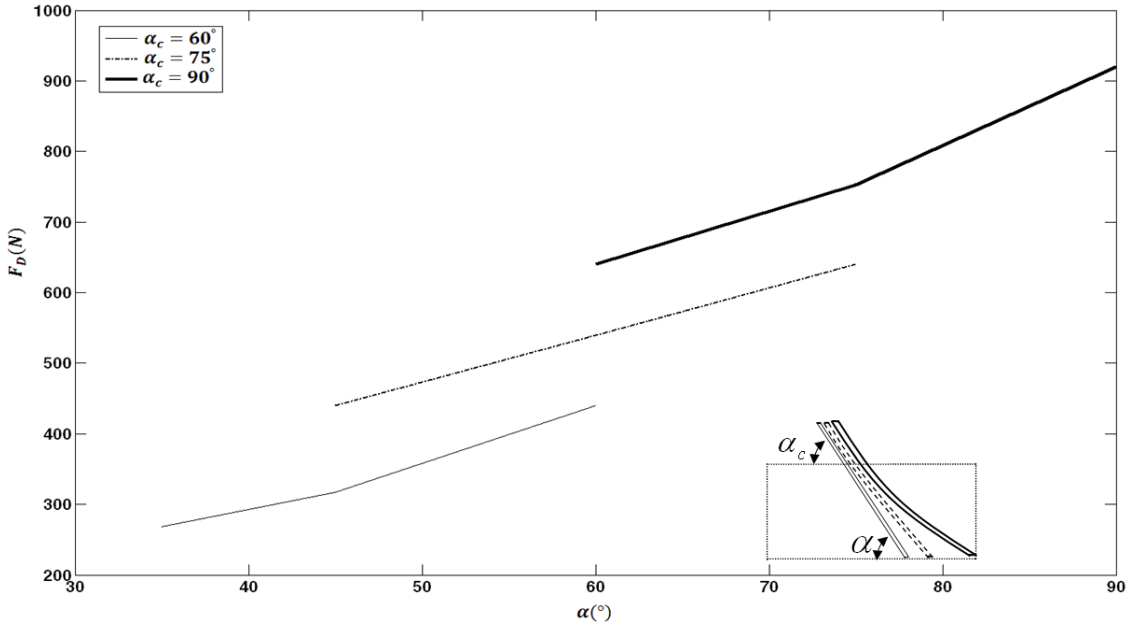

Figure 0.40: Variation of the draft force F_D with the rake angles α for different α_c.

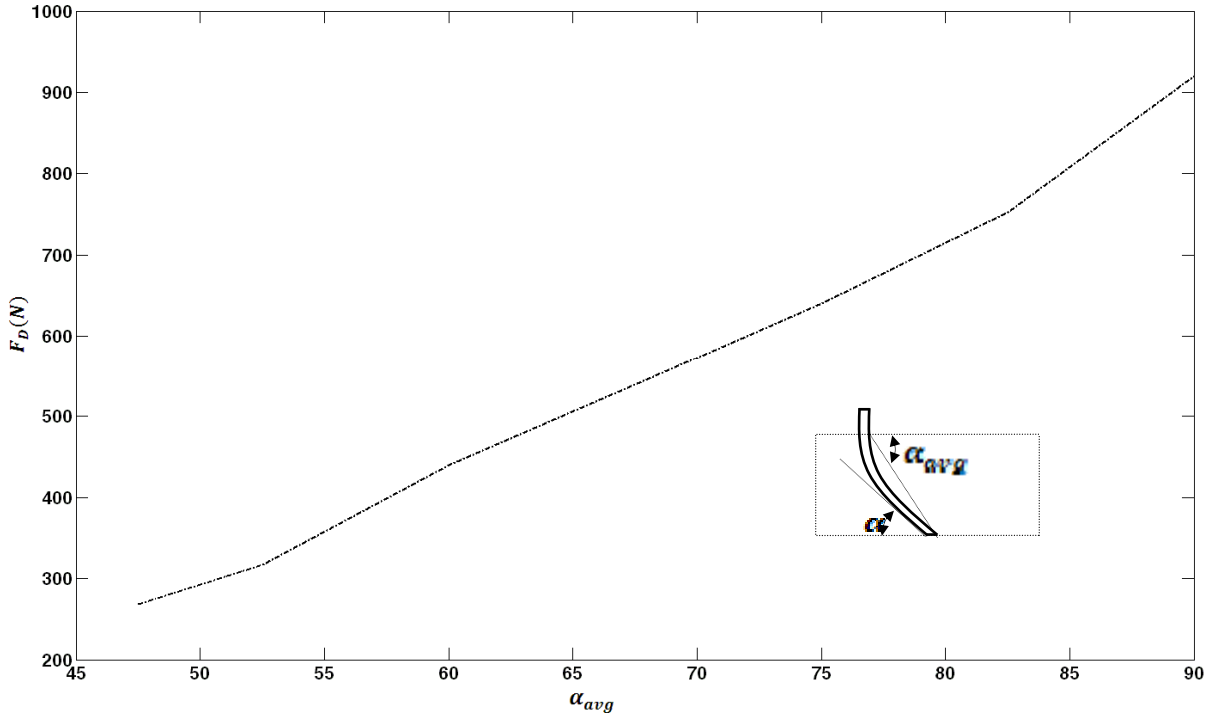

Figure 0.41: Variation of the draft force F_D with the blade's average rake angles (α_{avg})

1.17.2.2. Blades of triangular shapes

The effects of changing rake angle while keeping the angle α_c constant (in order to study the effect of changing radius of curvature) on the blade draft forces, are investigated using the FE models shown in Fig. 5.42. As shown in this figure, three FE models with different rake angles $\alpha = 60^\circ$, 45°, and 30° with same angle $\alpha_c = 60^\circ$ are simulated to increase the curvature and investigate its effect on the blade force. By decreasing the blade's rake angle, the blade's average rake angle α_{avg} decreases from 60° to 47.5°. Figs. 5.43 and 5.44 represent the FE results for blade (draft) force and averaged force acting on the blade of different rake angle α with constant curvature angle α_c. From these Figures, it is clear that by increasing the blade's curvature (decreasing the blade shape radius *R*), forces on the blades decrease with the same trend of

rectangular cases. As shown in Fig 5.44, by decreasing α_{avg} from 60° to 52.5°, the draft force (F_D) increases from 275N to 220N; and by decreasing α_{avg} from 52.5° to 47.5°, the draft force (F_D) decreases from 220N to 180N which means a more inclined blade shape has less draft force.

As shown in Fig. 5.45, draft forces of the rectangular blade are plotted based on blade's average rake angle, α_{avg} in comparison with the draft forces of the blade with the triangular shape. From this figure, it is clear that by increasing the blade's average rake angle α_{avg}, the difference between the draft forces of the rectangular blade and the triangular blade is increasing.

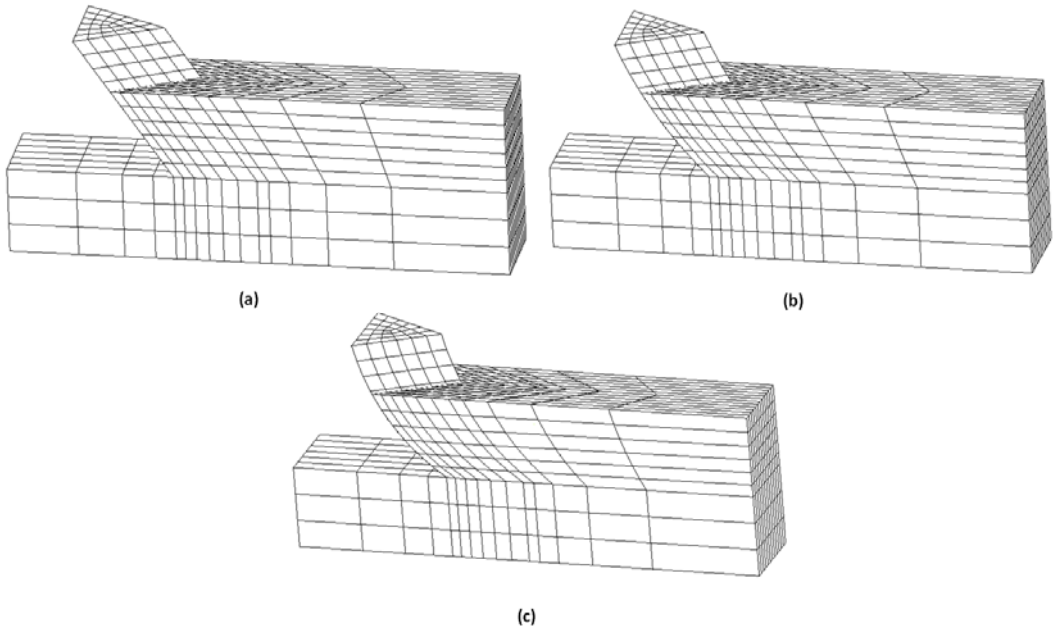

Figure 0.42: FE soil-triangular blade interaction model with three different blade's rake angles

(a) $\alpha = 60^{\circ}$, (b) $\alpha = 45^{\circ}$, (c) $\alpha = 35^{\circ}$ and constant $\alpha_c = 60^{\circ}$

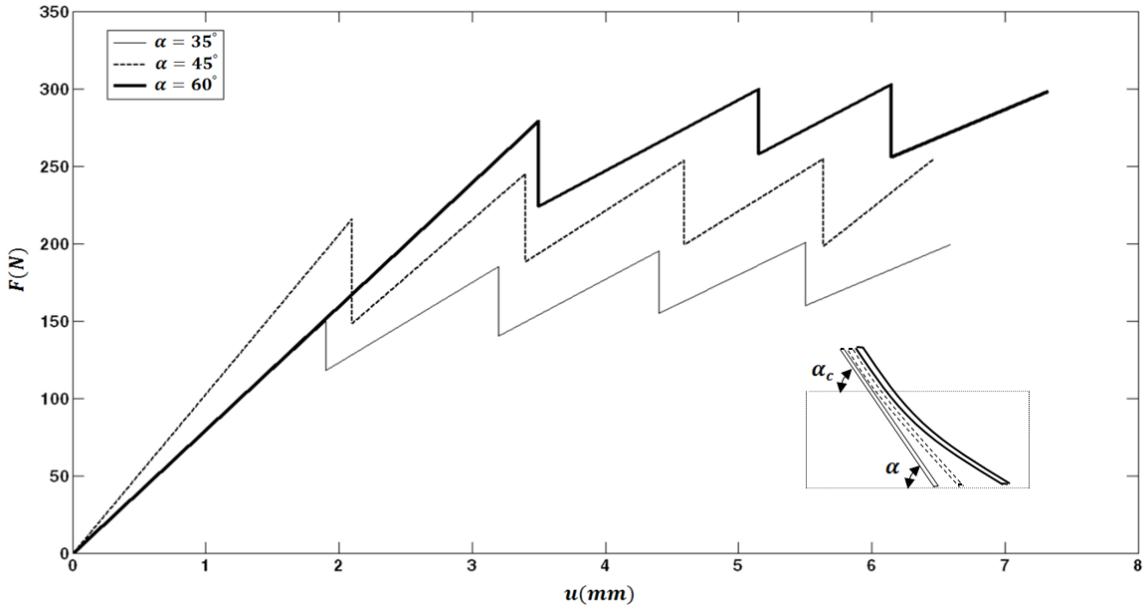

Figure 0.43: Variation of blade (draft) forces for different rake angles α with constant curvature angle $\alpha_c = 60^\circ$.

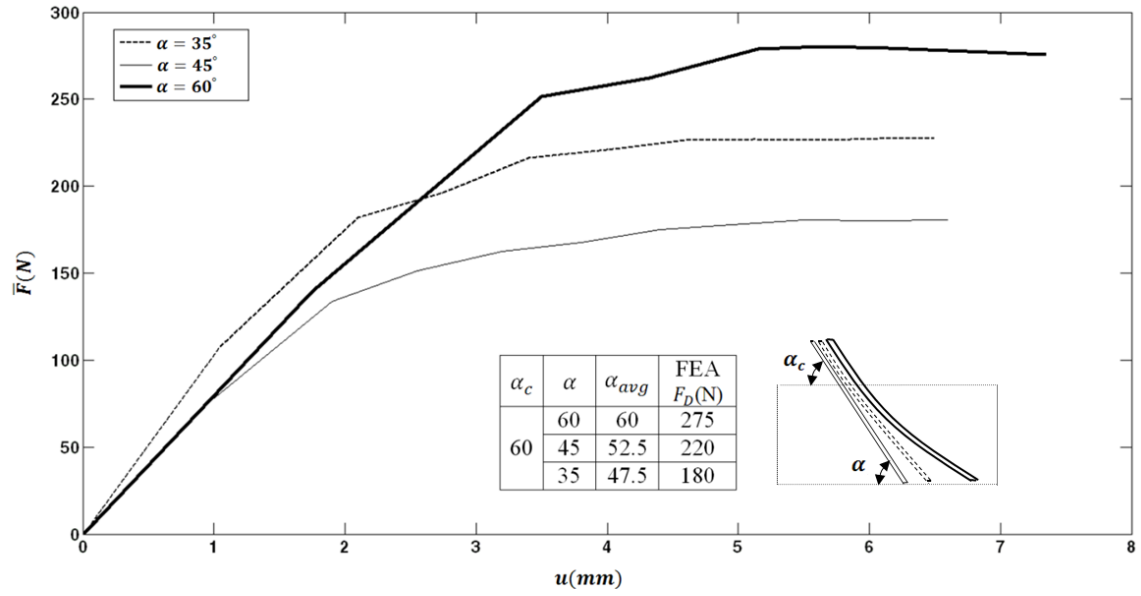

Figure 0.44: Variation of the average blade (draft) forces for different rake angles α with constant curvature angle $\alpha_c = 60^\circ$.

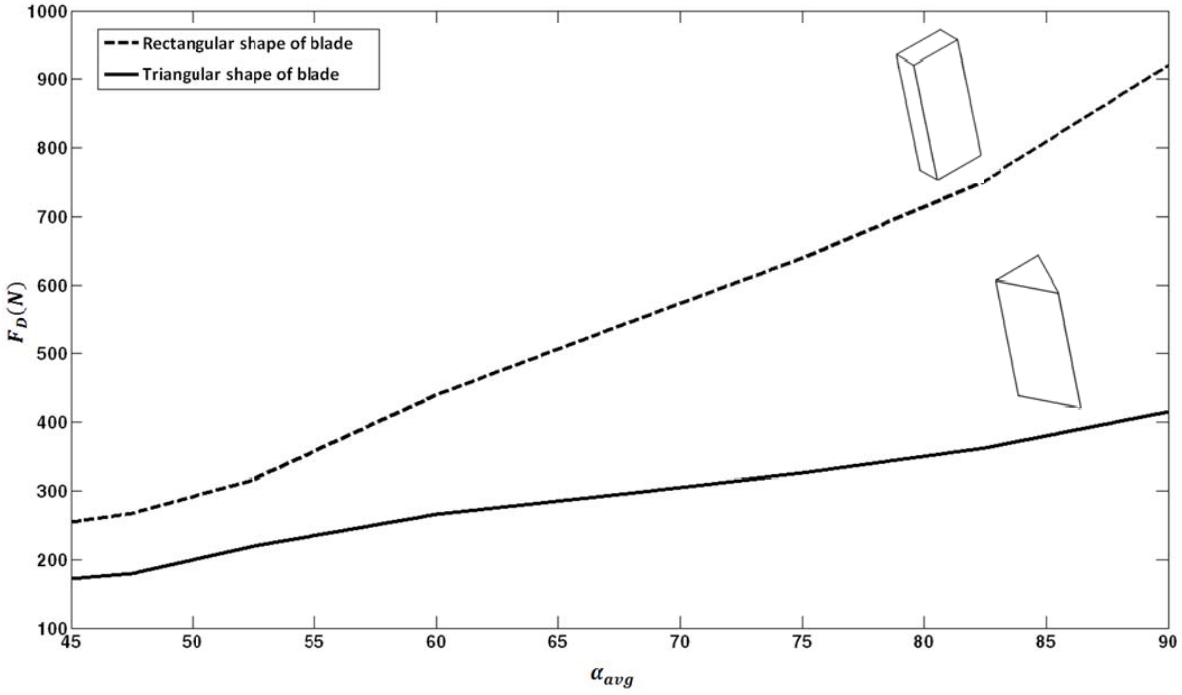

Figure 0.45: Comparing draft forces of rectangular and triangular shapes blade for different blade's average rake angles (α_{avg})

1.18. Effects of blade's sharpness on blade force in soil interaction

1.18.1. Changing blade's sharpness while keeping the blade's contact length constant

Five FE models with different sharpness angles were used in order to investigate the effects of the blade's sharpness on the blade's draft force (F_D) when keeping the contact length constant. As shown in Fig. 5.46, in order to study this effect, the interaction depth d_1, blade height h_1, blade's contact length L_s and blade's rake angle α are kept constant in all models. The only difference in these models is their sharpness angle (α_S) which varies from 30° to 90°

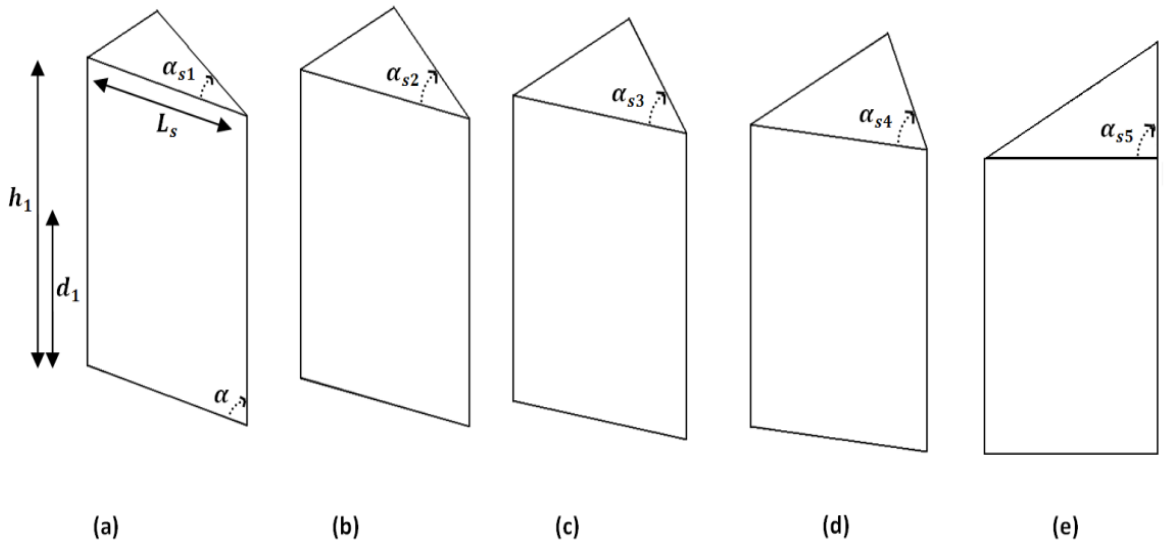

Figure 0.46: 3D model dimensions of triangular narrow blades with constant depth $(d_1 = 50mm)$, blade contact length $(L_s = 60mm)$, blade rake angle $(\alpha = 90^\circ)$, and different sharpness angle (a) $\alpha_{s1} = 30^\circ$, (b) $\alpha_{s2} = 40^\circ$, (c) $\alpha_{s3} = 53^\circ$, (d) $\alpha_{s4} = 75^\circ$, (e) $\alpha_{s5} = 90^\circ$

The FE results are given and plotted in Fig. 5.47. As expected, the blade's draft force (F_D) increases with increasing sharpness angle α_s and this increasing rate is almost constant. So by decreasing the blade's sharpness angle or in other words by increasing blade's sharpness, the average draft force decreases considerably.

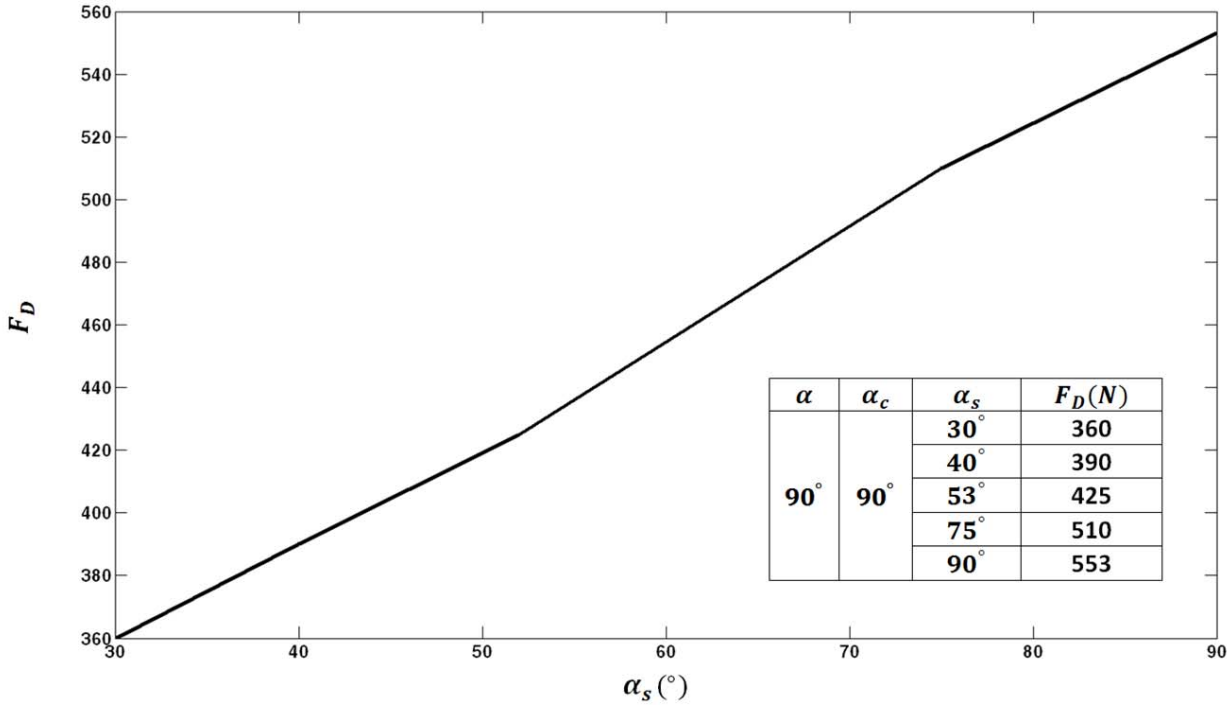

Figure 0.47: Draft forces (F_D) of the triangular blade with different blade's sharpness angles (α_S)

1.18.2. Changing the blade's sharpness while keeping blade's width constant

In order to study effects of the blade's sharpness on draft force (F_D) while the blade's width is constant (w_1), three FE models with different sharpness angles (α_S) were used. As shown in Fig. 5.48, in order to study this effect, the interaction depth d_1, blade height h_1, blade width w_1 and blade rake angle α, are kept constant in all models. The only difference in these models is their sharpness angle (α_S) which varies from 53° to 120°.

In order to examine the effects of α_s, the calculated draft force for $\alpha_s = 120^\circ$ is denoted as F_{D120° and is assumed as a reference. Then the ratios of F_D / F_{D120° for α_{si} are plotted in Fig 5.49.

It is clear from this Figure that by decreasing the sharpness angle α_S from 120° to 90° or increasing the blade's sharpness, the draft force decreasing 22% from $697N$ to $547N$. By further decreasing to 53°, the original draft force decreases 40% to $425N$; that means that for a constant width of groove, and a sharper blade, the less draft force (F_D) is applied to the blade.

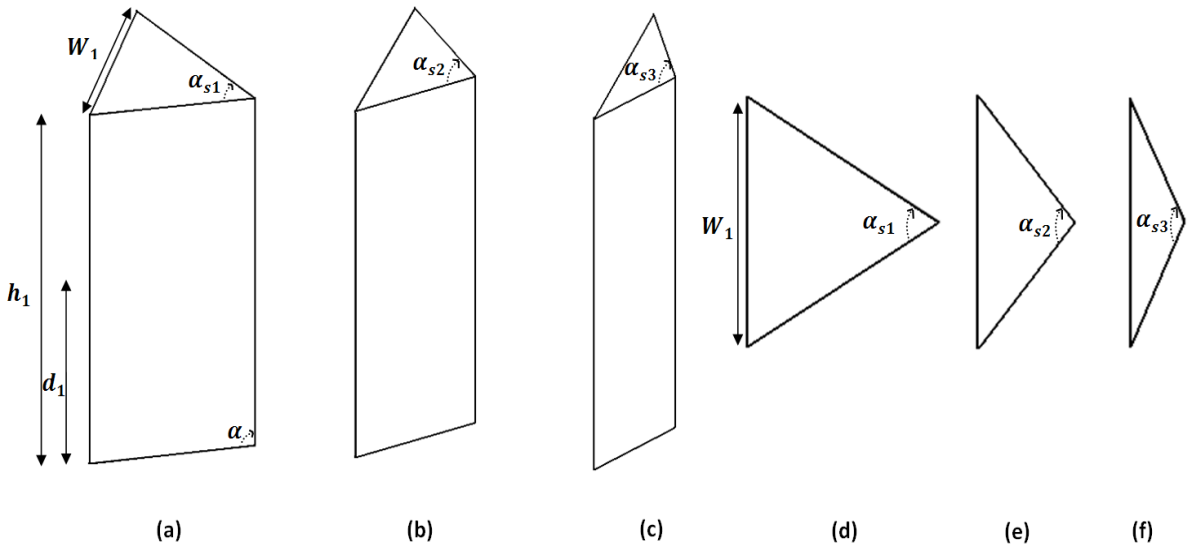

Figure 0.48: 3D model dimensions of triangular narrow blades with constant interaction depth ($d_1 = 50mm$), blade height ($h_1 = 100mm$), blade's width ($w_1 = 50mm$), blade rake angle ($\alpha = 90^\circ$) and different sharpness angle (a, d) $\alpha_{s1} = 53^\circ$, (b, e) $\alpha_{s2} = 90^\circ$, (c, f) $\alpha_{s3} = 120^\circ$. (d), (e), and (f) are top views of the triangular blades of (a), (b), and (c) respectively.

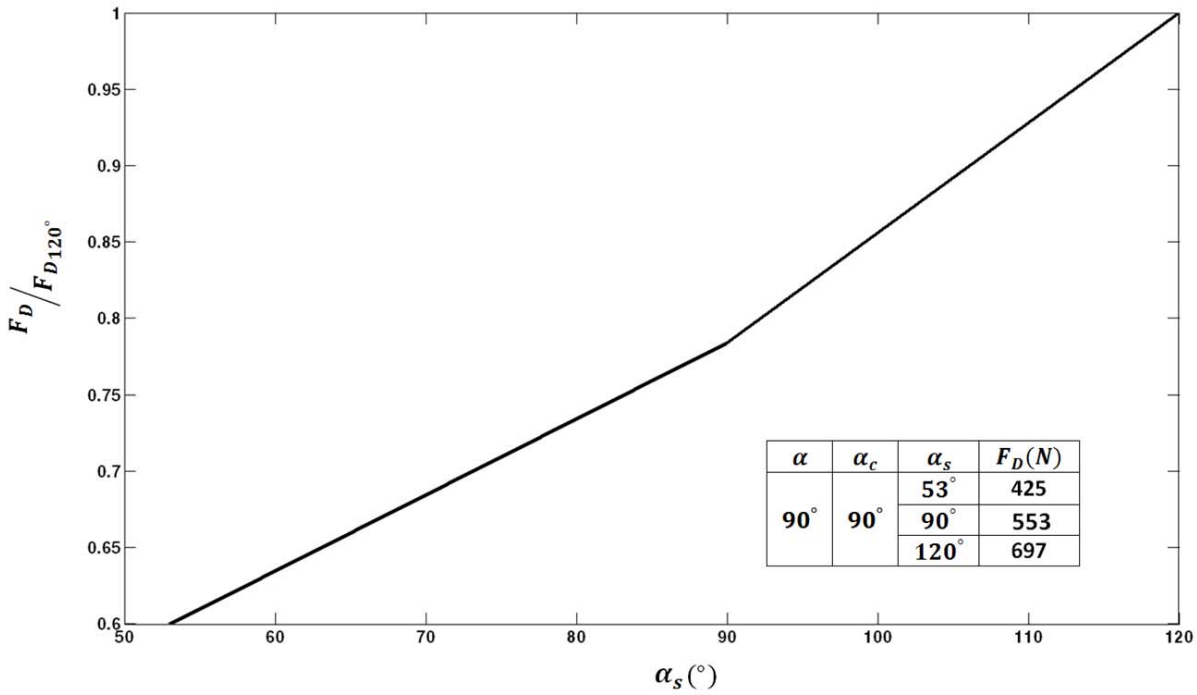

Figure 0.49: Non dimensional draft forces ratio (F_D/F_{D120°) of the triangular blade with constant blade's width and different blade's sharpness angles.

1.19. Deformation patterns

1.19.1. 2D model

It was shown that the FE model as described in the Sec.3.2.1 is capable of simulating soil-wide blade interaction. By moving the blade in the horizontal direction (about 11mm), the soil is swelled up in front of the blade as shown in Fig. 5.50. For example the maximum soil displacement upward is about 16 mm (the depth of cut soil is 50 mm) and is immediately at the blade as shown, and then decreases with the distance away from it.

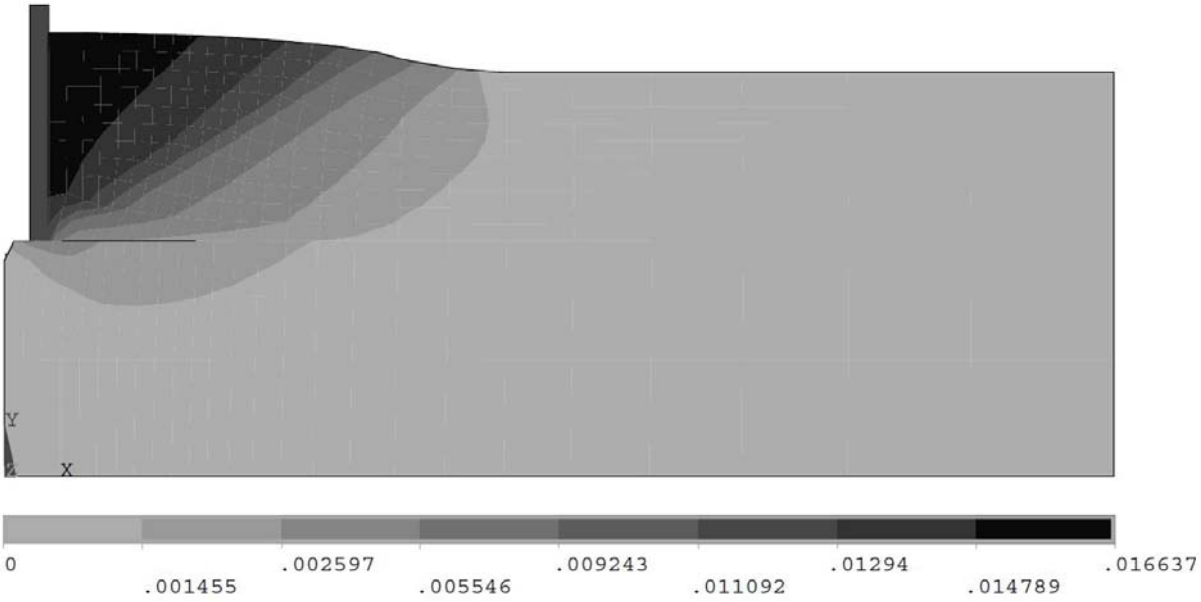

Figure 0.50: Displacement of soil for the blade with $\alpha = 90^{\circ}$.

The vector displacement plot of soil as shown in Fig. 5.51, indicates the swelled up soil in front of the blade due to the soil particles sliding upward with respect to the blade.

Fig. 5.52 shows the equivalent plastic strain of the soil. As shown, the maximum plastic strain of soil is located at the blade's lower tip (point D). The strain is decreased approximately in a line from D to B. This forms a wedge shape (triangle ABD) as also indicated in McKeyes [25]. The angle of this line with respect to horizontal line (direction of motion of the blade), is called soil plane failure angle, θ (as shown in Fig.5.52). The FEA result for this angle is $\theta = 29^{\circ}$ whereas the analytical value is about 27.5°; this is a good agreement, only 5% difference, and is support for validating our FE model.

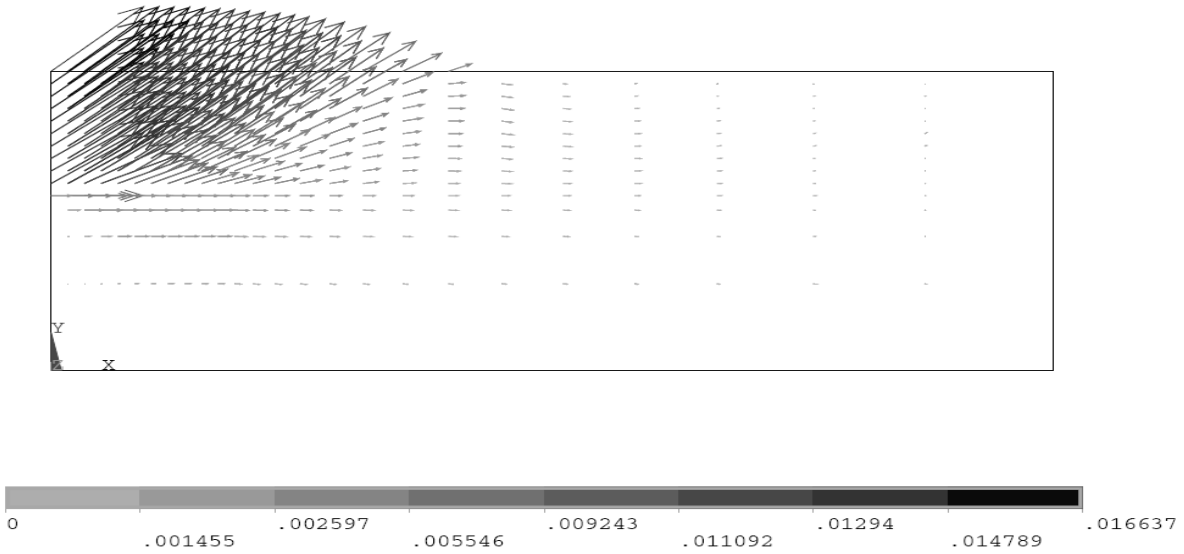

Figure 0.51: Displacement vector plot of soil

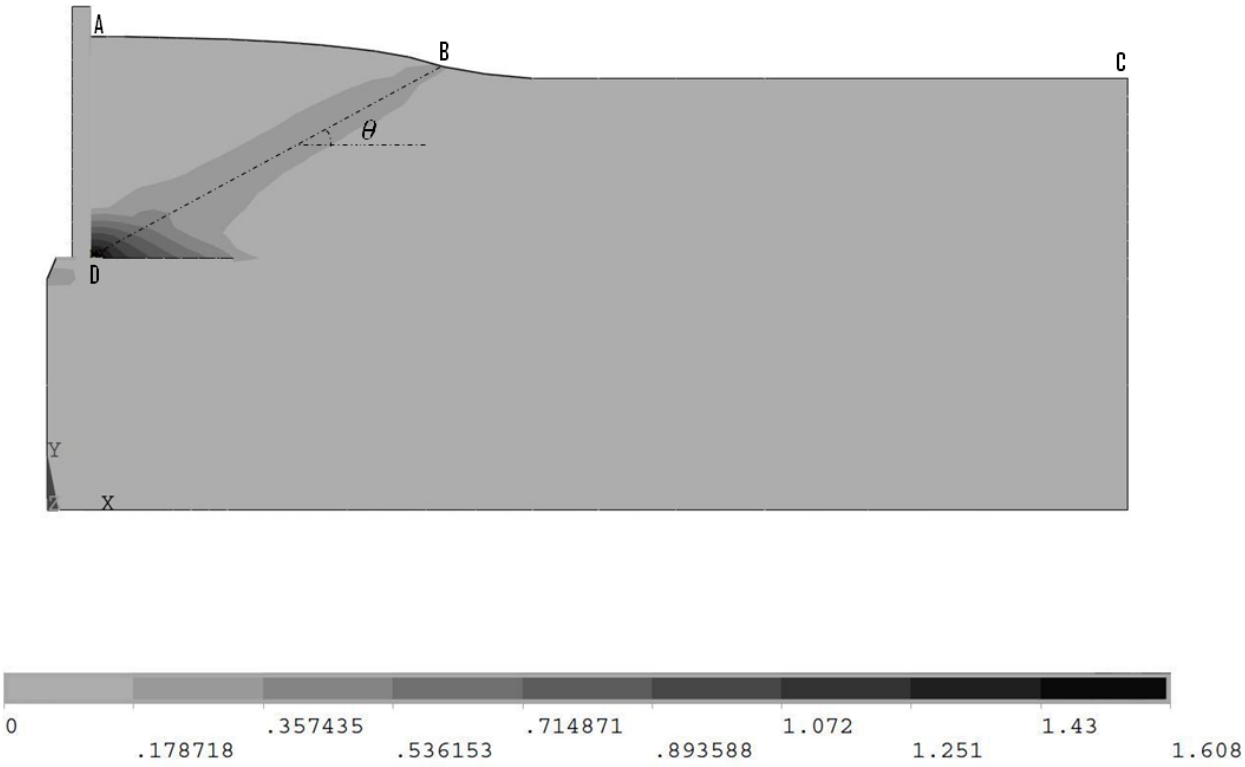

Figure 0.52: plastic strain distribution of soil in front of the blade and angle of failure plane;

A=1.608, B=0.189, C=0, D=0.0133 (FEA $\theta = 29^{\circ}$, analytical $\theta = 27.5^{\circ}$)

1.19.2. 3D model

1.19.2.1. Rectangular blade

Figures 5.53-5.55 show same deformation results for vertical rectangular blade after the blade has been moved by about 9*mm*.As shown in Fig. 5.53, by moving the blade in the horizontal direction after 16mm, the disturbed soil is accumulated in front of the blade and tends to swell in upward and lateral directions with respect to its original configuration. Observation of the FE results revealed that the failure curve could be reasonably described by a straight line, as indicated by Shmulevich et al. [26]. Also as observed in [26], by moving the blade through the soil in a horizontal direction, each layer of soil (above the separation surface) is pushed upward and the accumulated soil can be described as a convex curve; this is similar to the FE results shown in Fig. 5.54

As shown in Fig. 5.55 by moving the blade, the soil around the moving blade also goes upward to make an eliptical shape. By increasing soil accumulation, the plastic strain on the surrounding soil increases as well. The increased plastic strains based on soil accumulation are shown in Fig. 5.56 after the blade moved 16mm in the horizontal direction. As it is shown in Fig. 5.56, the maximum plastic strain is on the top of the soil adjacent to the blade; this location of maximum plastic strain is because of the soil deformation due to motion of the blade.

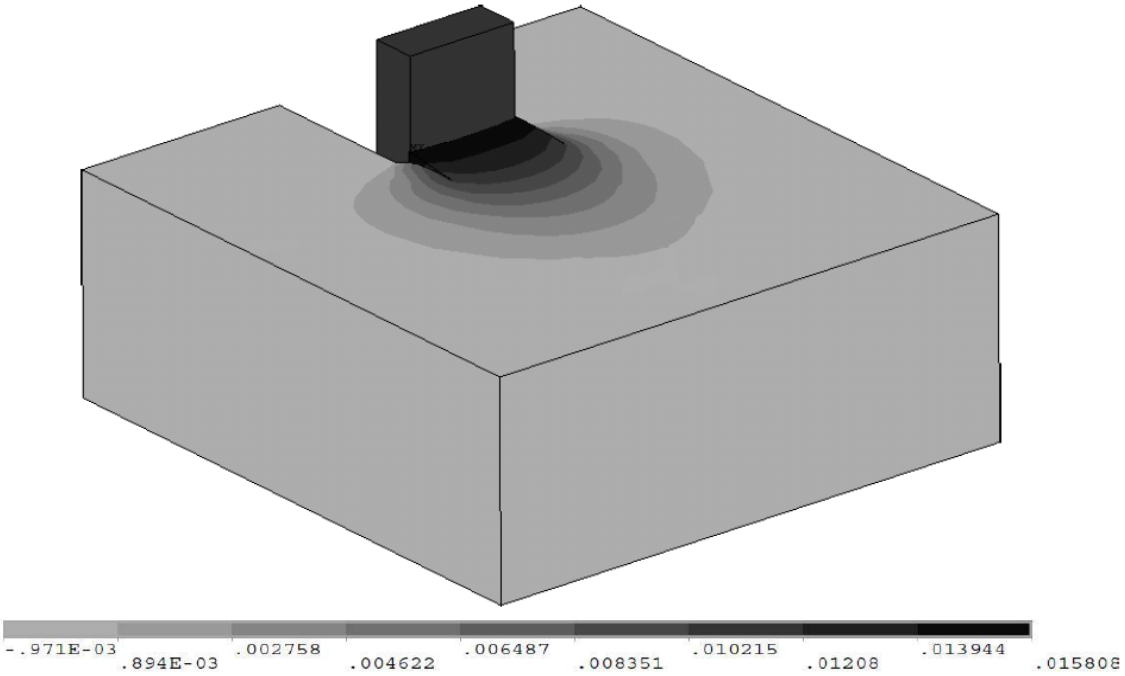

Figure 0.53: The deformed shape and the displacement of soil in the horizontal direction

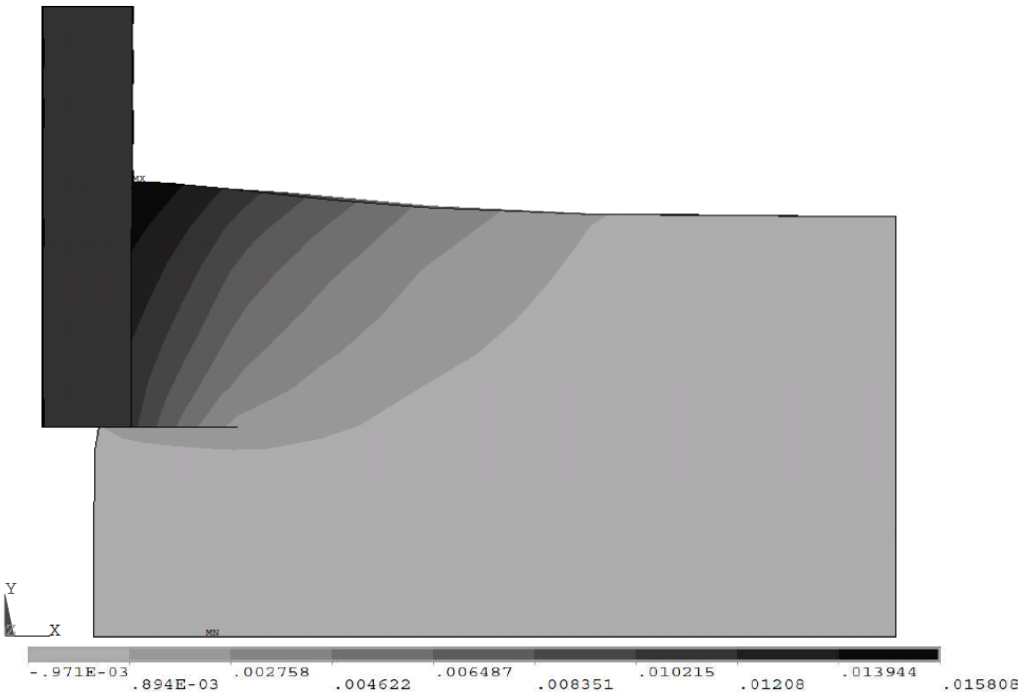

Figure 0.54: Displacement of soil (in front of the blade only)

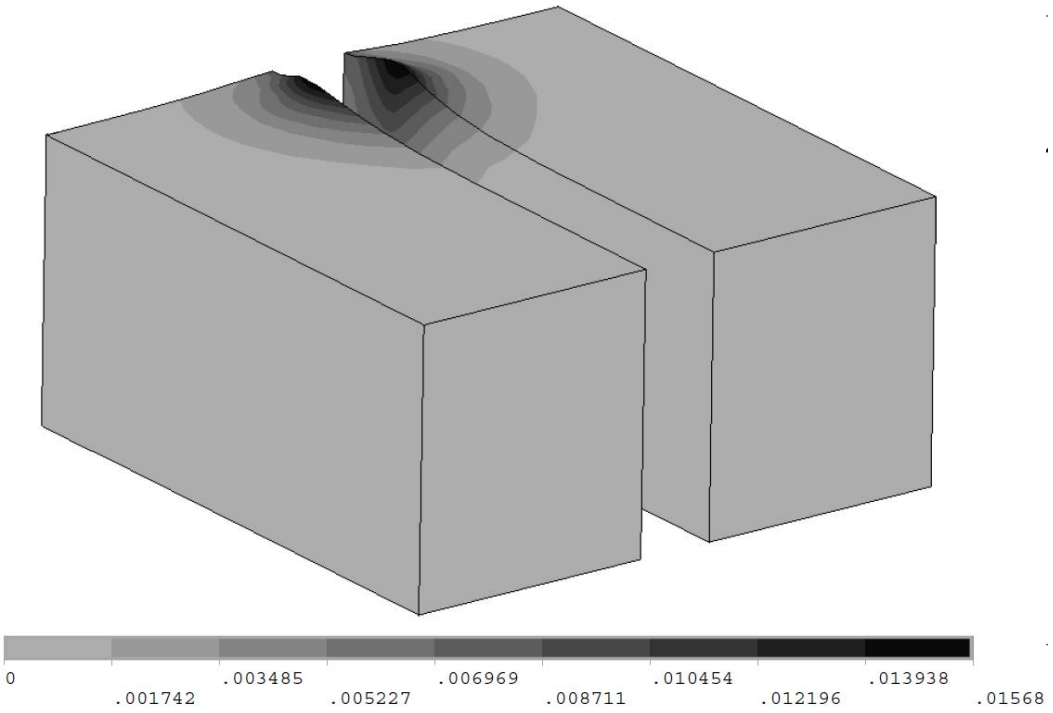

Figure 0.55: Displacement of soil without the blade (blade moved 16mm)

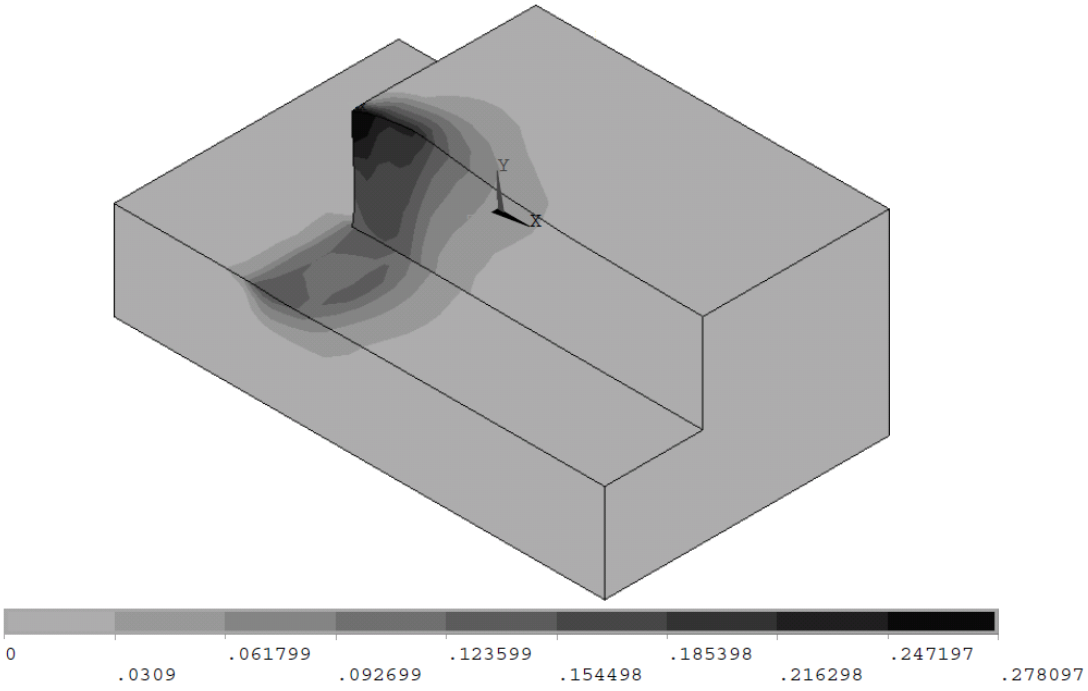

Figure 0.56: plastic strain distribution on the surrounding soil (blade moved 16mm)

As seen in Figs. 5.57 (a), (b) and 5.58 for curved rectangular blade, after 7*mm* displacement of the blade, the soil has swelled in upward and lateral directions with respect to its original configuration in a pattern similar to non-curved rectangular blade.

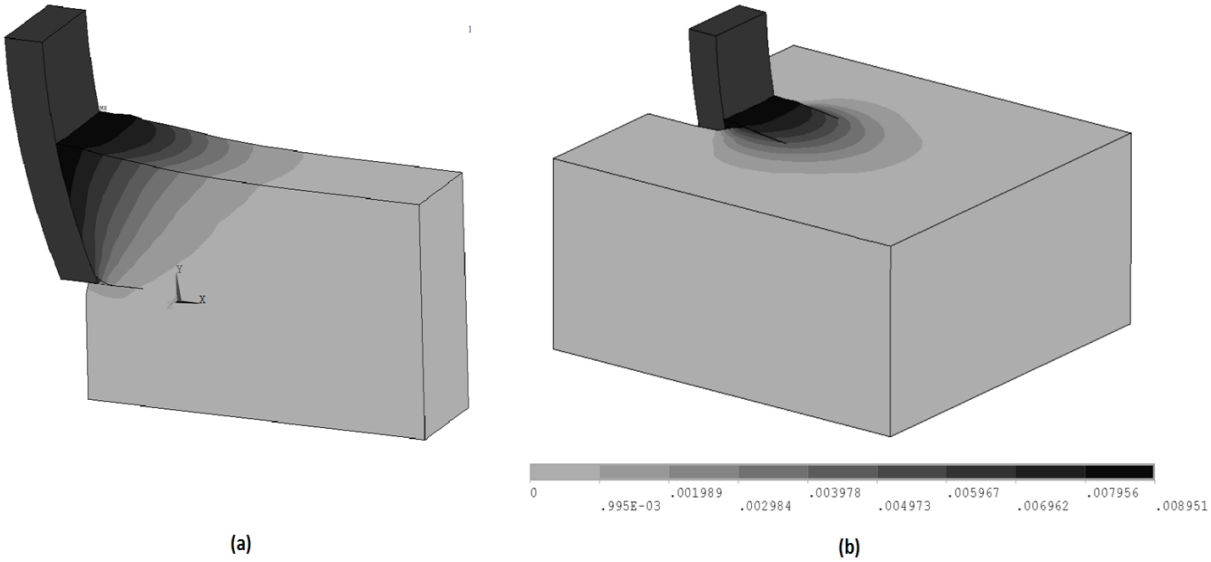

Figure 0.57: Displacement patterns of the soil at *u*=7*mm*: (a) in front of the blade, (b) at the top surface.

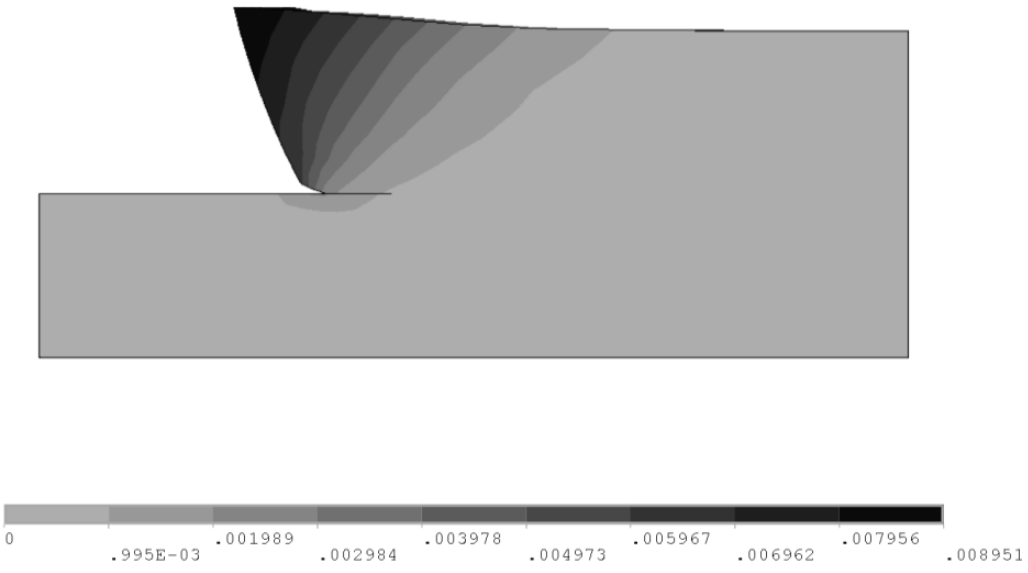

Figure 0.58: Details of displacement of soil in front of the blade at *u*=7*mm*.

1.19.2.2. Triangular blade

Figures 5.59-5.60 show same deformation results for the straight triangular blade after the blade has been moved by about 8.5*mm*. As seen in Fig. 5.59 (a) and (b), the soil has accumulated in front of the blade and tends to swell up in lateral directions with respect to its original configuration as mentioned in Sec. 5.4. Also as observed in Shmulevich et al. [26] for a rectangular blade, by moving blade through the soil in the horizontal direction, each layer of soil (above the separation surface) is pushed in upward and lateral directions and accumulated soil can be described as a convex curve; this is similar to the FE results shown in Fig.5.59(a).

Also according to Fig. 5.60, by moving the blade, the surronding soil goes upward to make an elliptical shape predicted in [26] as well.

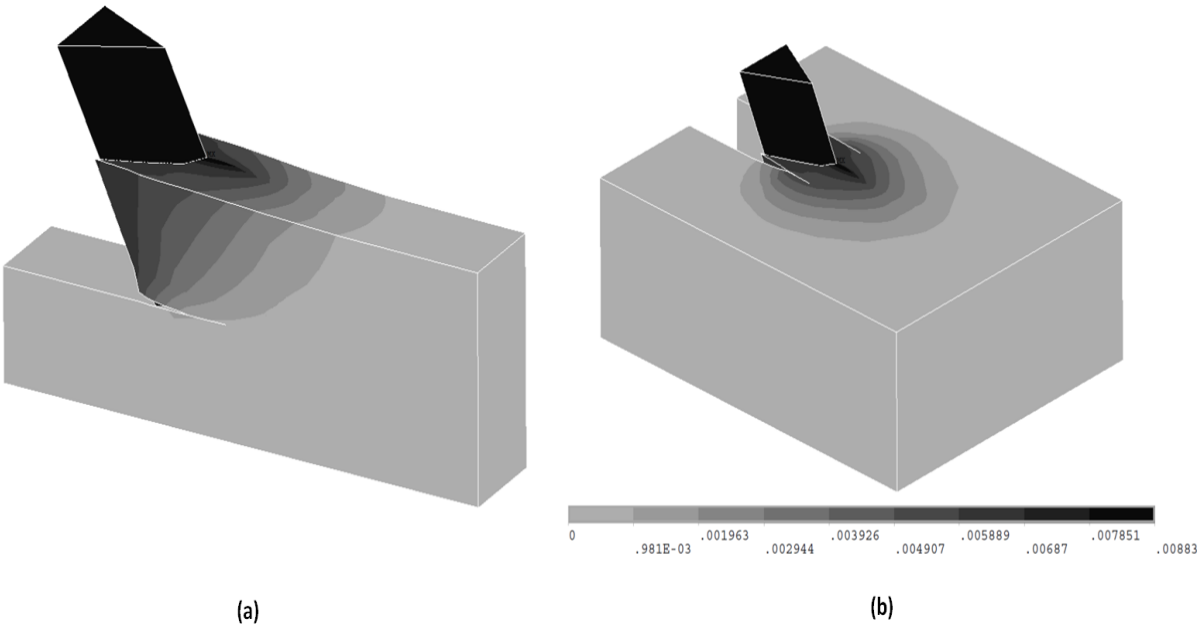

Figure 0.59: Interaction between soil and blade with $\alpha_c = \alpha = 60^\circ$ (a) Displacement of soil in front of the blade, (b) soil-blade configuration at *u*=8.5*mm*.

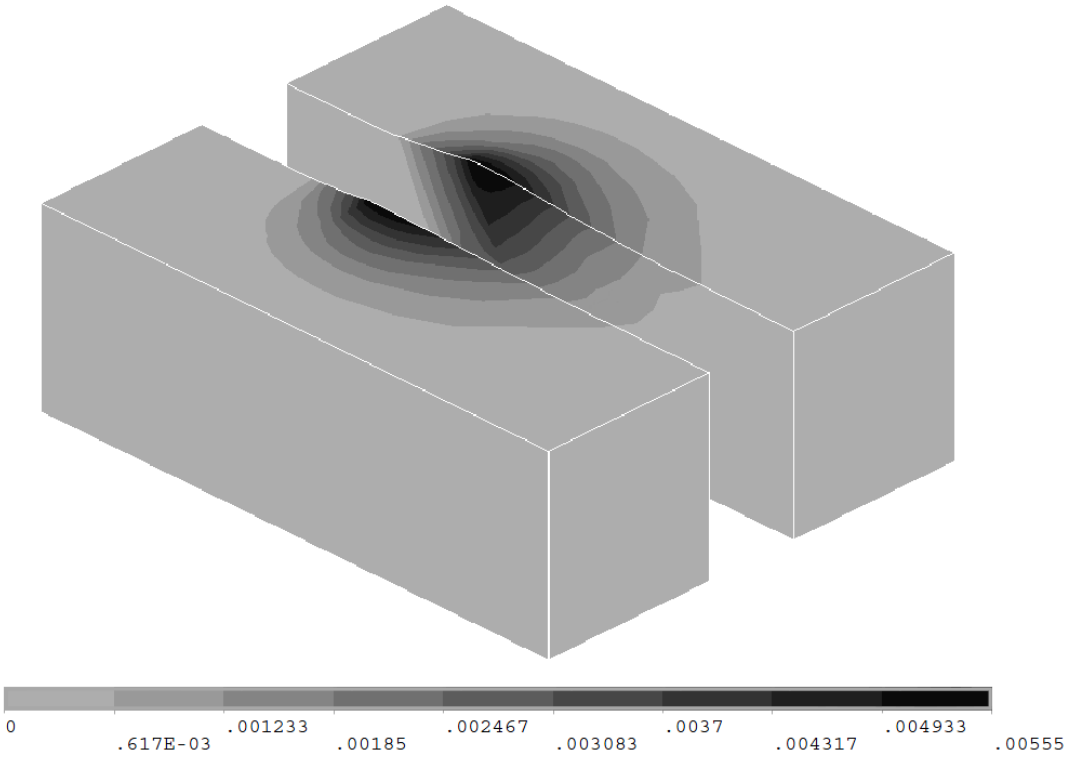

Figure 0.60: The displacement of soil with the frontal segment removed at u=8.5mm.

6. Conclusion and Future Work

6.1. Summary and Conclusion

The main objective of this thesis was to propose a simulation procedure for soil-tool interaction modeling for arbitrary blade configurations in order to show how the blade's shape affects the blade draft force. It is believed that the presented approach can be used to study the soil-tool interactions of real and more complex blade geometries and soil conditions and eventually used in developing software for optimization of tillage operations and improving design of blades used in tillage operations.

The thesis started with a literature review in the field of soil mechanics and soil interaction to study about previous research works. Then a new procedure for simulating the soil-blade interaction by the FE method was presented. The procedure combines the non-associated Drucker-Prager constitutive law with a compacting strain based separation criterion to describe the behavior of soil while being cut by the blade. Several separation and sliding surfaces were defined and utilized in the analysis. The elements on these surfaces were bonded to each other by special use of contact elements. During motion of the blade through soil, the bonding along the separation surfaces was allowed to break resulting in separation of the soil elements in front of the blade. The sliding surfaces allowed the soil to slide upward and sideways of the blade. A method of calculating the draft force that essentially eliminates the effects of 'discrete' disjoining particular nodes was proposed and tested for convergence.

First the procedure was applied on the straight rectangular blades, mainly for the purpose of validation. Effects of compacting strain limit on the draft force were studied. For the computational efficiency and to make a balance between computational efforts and accuracy,

$\varepsilon_c = 0.3$ were selected to initiate separation for the type of soil used in this research work (i.e. for $\varphi = 35^\circ$). Then the effects of soil internal friction angle, φ on the compacting strain limit, ε_c were investigated. The procedure was applied for $20^\circ \le \varphi \le 40^\circ$ with the conclusion that by increasing internal friction angle, the compacting strain limit should be also increasing almost linearly within the range $0.2 \le \varepsilon_c \le 0.35$.

In the next step, the choice of element size on the separation surface in the vicinity of blade was investigated. The effect of mesh density on the draft force for the straight rectangle blade with rake angles $\alpha = 60^\circ$ and $\alpha = 90^\circ$ were discussed and selected based on computational efficiency.

Then the simulation force results for both wide (2D model) and narrow (3D model) blades were compared with the semi-analytical formulas of the classical soil mechanics which showed good correlation between simulation and analytical results.

Plastic strain distribution of soil in front of the 2D blade model was shown. The failure plane angle of the FE model was compared with the analytical one that showed only a 5% difference, and was another check for validating our FE model. Also deformation results for the 3D vertical rectangular blade were presented that showed the accumulated disturbed soil in front of the blade and its tendency to swell in upward and lateral directions with respect to its original configuration. These FE results revealed that the failure curve could be reasonably described by a straight line, as indicated by previous analytical works. Furthermore the maximum plastic strain was on the top of the soil, adjacent to the blade.

After analytical validation, the FE force results were compared with experimental ones. The rectangular blade draft forces with several rake angles were recorded and the results for

$\alpha = 60^{\circ}$ was shown in this study. Because of sensitivity of the monorail's measuring system to all the natural frequencies, the recorded signals were noisy. Therefore these signals were filtered to exclude all those frequencies which have no effect on the force results. Natural frequencies were determined and verified by applying FFT to the signals from the horizontal load cells and the attached accelerometer. The experimental results were compared with the analytical and simulation results. The difference between the analytical and experimental results is 2.3% and the difference between the FE and experimental results is 1.6%; this shows good correlations between these three methods.

The effects of blade width, depth and rake angle on blade draft force were investigated by simulating soil-blade interaction with different blade dimensions. It was concluded that by doubling the blade depth in the soil (d_1), the blade force increases approximately 4 times when w_1 / d_1 keeps constant and approximately 3 times when blade width (w_1) remains constant. It was also demonstrated that generally by increasing the rake angle, the force increases almost linearly.

After validating the FE results for straight rectangular blades both analytically and experimentally, the rectangular curved blade was simulated in order to investigate the effects of changing the blade's radius of curvature on the draft force. These effects were studied in two different cases, with constant rake angle α and then with constant angle α_c. It was concluded that by decreasing the radius (or increasing the curvature), the blade force increases while keeping the angle α constant, and decreases when angle α_c remains constant, which in the other words means that a more inclined blade requires less draft force.

Next the soil interaction with the straight triangular blade in different rake angles was simulated. Since the analytical solution is limited to only rectangular blades, force results for triangular blade were verified experimentally. Therefore, a triangular blade with the ability of changing its rake angle was fabricated and tested in four different rake angles at the soil bin facility. After filtering the draft force signals, the difference between FE and experimental results were less than 9% in all cases that showed good correlations between these methods. Therefore the FE model for triangular blade was validated experimentally.

Then the triangular blade was compared with the rectangular one with the same width and depth of interaction. It was shown that the triangular blade draft force is around half of the amount of force acting on the rectangular blade with the same rake angle; which means that for the same width of groove through the soil, the triangular blade needs much less force than the rectangular one. Also soil distributions of these two shapes of blades were compared with each other. For rectangular blade, the soil is accumulated in front of the blade and tends to swell in upwards and lateral directions with respect to its original configuration. However for the triangular blade, the soil is pushed mostly in lateral directions and slightly accumulated in front of the blade.

After the comparison of two shapes of blades, the effects of changing the blade's radius of curvature on the draft force were also studied on the triangular blade which came to the same deduction as the rectangular blade that the more inclined blade requires less draft force.

Next, the effect of the triangular blade's sharpness on draft force was discussed. By changing the blade's sharpness, the draft forces of the triangular blade were calculated in two conditions of constant blade width and constant blade contact length. The draft force increased almost linearly with increasing sharpness angle in both conditions. As showed, by decreasing the blade's

sharpness angle or in other words by increasing blade's sharpness, the draft force decreased considerably. For a constant width of groove, the sharper the blade, the less draft force applied on the blade.

6.2. Future Work

Suggestions arising from the presented study to improve future research works are divided into the three following categories:

1) On the FE modeling with automatic strain monitoring and turn off/on contact elements on the separation line:

During the soil-blade simulation in the presented study, the strain component in the direction of the blade's motion, ε_x was monitored manually after each step until it reached the predefined compacting strain limit, ε_c. At this instant, the contact elements of the correspondent element were turned off manually to generate the separation. Surely it will improve the study if this monitoring process and activating / deactivating the contact elements are done automatically. This automation will be useful in shape optimization of blade.

2) On optimizing the shape of blade:

In the presented study, the proposed simulation procedure was applied on two common shapes of narrow blades (rectangular and triangular) and the effects of all dimensional aspects on draft force were investigated. For continuing this study and finding the best shape of blade to minimize the consumed energy during tillage, this procedure should be applied on more arbitrary shape and eventually used to develop software for shape optimization.

3) On improving the experimental instruments:

As noted earlier, the FE simulation force results were validated by tool-force measuring systems with externally located load cells. Although the results from these load cells are accurate enough to validate the simulation models, there are some suggestions to improve this system for future tillage interaction tests.

The S shape load cell, SM1000 (Super-Mini), used in the soil bin is a low-cost, yet accurate cell with a straight-through loading design. This system has two weaknesses; one is that the S-shape load cells work poorly in compression which affects the accuracy of measuring the side loads and the second is the sensitivity to natural vibrations that produce noisy signals and require filtering the force results. These two weaknesses should be resolved in order to improve accuracy of results.

Substituting S-shape load cells by low profile load cells is one way to increase precision in draft force results. Since low profile series of load cells have the advantages of moment cancellation, they are better suited to applications that may apply side loads or moment loads into the cells. Also employing instrumented tillage where load cells or strain gauges are attached to the tillage will decrease the effect of system vibration in the force result. Combination of these two suggestion methods will increase the accuracy of force results and remove all the drawbacks.

7. References:

[1] S. Davoudi, R., Alimardani, A. Keyhani, R. Atarnejad. A two dimensional finite element analysis of a plane tillage tool in soil using a non-linear elasto-plastic model. American-Eurasian J. Agric.& Environ. Sci. 3 (2008) 498-505.

[2] S. Karmakar. Modeling of soil-tool interaction in tillage. Transworld research network, India, 2008.

[3] S.R. Ashrafizadeh. Modeling of energy requirements by a narrow tillage tool. Doctoral Thesis at the University of Saskatchewan, Saskatoon, Canada, 2006.

[4] Y. Qinsen, S. Shuren. A soil–tool interaction model for bulldozer blades. Journal of Terramechanics. 31 (1994) 55–65.

[5] A.M. Mouazen, M. Nemenyi. Tillage Tool Design by the Finite Element Method: Part 1. Finite Element Modelling of Soil Plastic Behaviour. J. Agric. Engng Res. 72 (1999) 37-51

[6] UA. Rosa, D. Wulfsohn. Constitutive model for high speed tillage using narrow tools. Journal of Terramechanics. 36 (1999) 221–234.

[7] D.R.P. Hettiaratchi, A.R., Reece. The calculation of passive soil resistance. Computers and Geotechnique. 24 (1974) 280-310.

[8] E. McKyes, O.S. Ali. The cutting of soil by a narrow blade. Journal of Terramechanics. 14 (1977) 43-58.

[9] M. Abo-Elnor, R. Hamilton, J.T. Boyle. Simulation of soil-blade interaction for sandy soil using advanced 3D finite element analysis. Soil & Tillage Research. 75 (2004) 61-73.

[10] J. Su, Y. Wang. Equivalent dynamic in finite element for soil–structure interaction. Finite elements in analysis and design. 63 (2013) 1-7.

[11] L. Yu, J. Liu, X.J. Kong, Y. Hu. Three-dimensional RITSS large displacement finite element method for penetration of foundations into soil. Computers and Geotechnics. 35 (2008) 372-382.

[12] J. M. Duncan, C. Y. Chang. Non-linear analysis of stress and strain in soils. J. Soil Mech. 96 (1970) 1629-1653.

[13] D. Sheng, K.D. Eigenbrod, P. Wriggers. Finite element analysis of pile installation using large-slip frictional contact. Computers and Geotechnics. 32 (2005) 17-26.

[14] S.K Upadhyaya, U.A. Rosa, D. Wulfsohn. Application of the finite element method in agricultural soil mechanics. advances in soil Dynamics. 2 (2002) 117-153.

[15] A. J. Mao. Finite element approach to solve contact problems in geotechnical engineering. Int. J. Numer. Anal. Meth. Geomech. 29 (2005) 525–550.

[16] K. S. Kazakov. Elasto dynamic in finite elements with united shape functions for soil - structure interaction. Finite element in analysis and design. 46 (2010) 936-942.

[17] Y. Liu, C. Wang, Q. Yang. Stability analysis of soil slope based on deformation reinforcement theory . Finite elements in analysis and design. 58 (2012) 10-19.

[18] A. A. Javadi, A. Faramarzi, A. Ahangar-Asr. Analysis of behaviour of soils under cyclic loading using EPR-based finite element method. Finite elements in analysis and design. 58 (2012) 53-65.

[19] Y. Chen, L. J. Munkholm, T. A. Nyord. Discrete element model for soil-sweep interaction in three different soils. Soil & Tillage Research. 126 (2013) 34-41.

[20] J. M. Huang, J. T. Black. An evaluation of chip separation criteria for the fem simulation of machining. J. Manufacturing science and Engineering. 118 (1996) 461-469

[21] E. G. Ng, D.K. Aspinwall. Modeling of hard part machining. J. Material processing technology. 127 (2002) 222-229.

[22] A.P. Markopoulos. Finite element method in machining process. Springer, London, 2013.

[23] Ansys version 11.0: Standard user's manual, 2008. Available from www.ansys.com

[24] A. Bankole. Critical State Behaviour Of An Agricultural Soil. Doctoral Thesis at the University of Saskatchewan, Saskatoon, Canada, 1996.

[25] E. McKeyes. Soil cutting and tillage. Elsevier Science Publishing Company, New York, 1985.

[26] I. Shmulevich, Z. Asaf, D. Rubinstein. Interaction between soil and a wide cutting blade using the discrete element method. Soil & Tillage Research. 97 (2007) 37–50

[27] E. McKyes. Agricultural Engineering Soil Mechanics. Elsevier Science Publishing Company, New York, 1989.

[28] E. McKyes, J. Maswaure. Effect of design parameters of flat tillage tools on loosening of a clay soil. Soil and Tillage Research, 43 (1997): 197-206.

[29] M. Rashidi, I. Najjarzadeh, B. Jaberinasab,S. M. Emadi, M. Fayyazi. Effect of Soil Moisture Content, Tillage Depth and Operation Speed on Draft Force of Moldboard Plow. Middle-East Journal of Scientific Research 16 (2013): 245-249

[30] W.R. Gill, G.E. Vanden Berg. Soil Dynamics in Tillage and Traction. USDAARS Agricultural Handbook No. 316. U.S., Washington DC, 1968.

[31] A.J. Koolen, H. Kuipers. Agricultural soil mechanics. Berlin, Germany. Library of Congress Cataloging in Publication Data, 1983

[32] F.V. Blasio. Introduction to the physics of landslides. Springer, 2011

[33] J. Mulqueen, J.V. Stafford, D.W. Tanner. Evaluation of penetrometers for measuring soil shear strength. Journal of Terramechanics 14 (1977): 137-151.

[34] J.H. Schmertmann. Measurement of insitu shear strength. In Proceedings of the Conference on insitu measurement of soil properties, 2 (1975) 57-138.

[35] J. Shen, R.L. Kushwaha. Soil-machine interactions. Marcel Dekker INC., New York, 1998.

[36] A.R. Reece. The fundamental equation of earth-moving mechanics. Proceedings of the IMechE, 179 (1965): 16-22

[37] K. Terzaghi. Theoretical soil mechanics. J. Wiley & Sons Inc., N.Y. 1959

[38] W.J.M. Rankine. On the stability of loose earth. Philosophical transaction of the royal society. 147 (1857): 9-27.

[39] P. C. J. Payne. The relationship between the mechanical properties of soil and the performance of simple cultivation implements. Journal of agricultural engineering research, 1 (1956): 23-50.

[40] P. C. J Payne, D. W. Tanner. The relationship between rake angle and the performance of simple cultivation implements. Journal of agricultural engineering research, 4 (1959): 312-325.

[41] J.R. O'Callaghan, K. M. Farrelly. Cleavage of soil by tined implements. Journal of agricultural research, 9 (1964): 259-270.

[42] D. R. P. Hettiaratchi, A. R. Reece. Symmetrical three-dimensional soil failure. Journal of Terramechanics. 4 (1967): 45-67

[43] R. D. Grisso, J. V. Perumpral. Review of model for predicting performance of narrow tillage tool. Transactions of the ASAE 28 (1985): 1062-1067

[44] S. K. Upadhyaya, W.J. Chancellor. Tillage mechanics. Advances in Soil Dynamics. 3 (2009): 275-320.

[45] R. J. Godwin, G. Spoor. Soil failure with narrow tines. Journal of agricultural engineering research, 22 (1977): 213-228.

[46] A. P. Onwualu, K. C. Watts. Draught and vertical forces obtained from dynamic soil cutting by plane tillage tools. Soil and Tillage, 48 (1998): 239-253.

[47] R. N. Yong, A. W. Hanna. Finite element analysis of plane soil cutting. Journal of Teramechanics. 14 (1977): 103-125.

[48] L. Chi, R. L. Kushwaha. Finite element analyisis of forces on a plane soil blade. Canadian Agricultural engineering. 31 (1989): 135-140.

[49] D. Pollock, J. V. Perumpral, T. Kuppusamy. Finite element analysis of multipass effects of vehicles on soil compaction. Transaction of the ASAE. 29(1986):45-50.

[50] L. Chi, R. L. Kushwaha. Three-dimensional, finite element interaction between the soil and simple tillage tool. Transaction of the ASAE. 34 (1991): 361-365.

[51] S. László, K. Attila. A new exact integration method for the Drucker–Prager elastoplastic model with linear isotropic hardening. International journal of solids and structures, 49 (2012): 170–190.

[52] D.C. Drucker, W. Prager. Soil mechanics and plastic analysis or limit design. Quaterly of Applied Mathematics, 10 (1952): 157-165.

[53] D. Wulfsohn, B. A. Adams. Critical-state soil mechanics for unsaturated agricultural soils. In Advances in Soil Dynamics, 2 (2002): 71-116.

[54] S. K. Upadhyaya. Finite element analysis of soil-tillage tool interaction. Advances in Soil Dynamics. 3 (2009): 323-334.

[55] C. S. Desai, H. V. Phan, J. V. Perumpral. Mechanics of three-dimensional soil structure interaction. J. Eng. Mech. Division, Proc. of ASCE, 108 (1982): 731-747.

[56] Y. Liu, Z. M. Hou. Three dimensional nonlinear finite element analysis of soil cutting by narrow blades. *In Soil Dynamics as Related to Tillage Machinery Systems. Proc. of the Intl. Conf. on Soil Dynamics*, 2 (1985): 322-337.

[57] J. V. Perumpral, R. D. Grisso, C. S. Desai. A soil tool model based on limit equilibrium analysis. Trans. ASAE 26 (1983): 991-995.

[58] J. Shen, R. L. Kushwaha. Investigation of an algorithm for non-linear and dynamic problems in soil-machine systems. Computers and Electronics in Agric. 13 (1995): 51-66.

[59] U.A. Rosa. Performance of narrow tillage tools with inertial and strain rate effects. Doctoral Thesis at the University of Saskatchewan, Saskatoon, Canada, 1997.

[60] A. M. Mouazen, M. Nemenyi. Finite element analysis of subsoiler cutting in nonhomogeneous sandy loam soil. Soil and Tillage Res. 51 (1999): 1-15.

[61] S.K. Upadhyaya, W.J. Chancellor, J.V. Perumprai, D.L. Wulfsohn, T.R. Way. Advances in soil dynamics. American Society of Agricultural and Biological Engineers. 3 (2009).

[62] K. Chandon, R.L. Kushwaha. Soil Forces on Deep Tillage Tools. In: AIC Meeting CSAE/ESGR. Program Saskatoon, Saskatchewan, 2002.

[63] A. P. Onwualu. An extended octagonal ring dynamometer for measurement of forces on a simple tillage tool. Nigerian Journal of Technology. 21 (2002): 46-59

[64] R. J. Godwin, A. J. Reynolds, M. J. O'Dogherty, A. A. Al-Ghazal. A triaxial dynamometer for force and moment measurements on tillage implements. J. Agric. Eng. Res. 55(1993) 189-205.

[65] Y. Chen, N.B. McLaughlin, S. Tessier. Double extended octagonal ring (DEOR) draba dynamometer. Soil and tillage. Res. 93(2007) 462-471.

[66] G. Girma. Multicomponent dynamometer for measurement of forces on plough bodies. J. Agric. Eng. Res. 42 (1989): 85-96.

[67] R. Berntsen, B. Berre, T. Torp, H. Aasen. Tine forces established by a two-level model and the draught requirement of rigid and flexible tines. Soil and Tillage Res. 90 (2006): 230-241.

[68] J. L. Glancey, S. K. Upadhyaya, W. J. Chancellor, J. W. Rumsey. An instrumented chisel for the study of soil-tillage dynamics. Soil and Tillage Res. 14 (1989): 1-24.

[69] V. I. Adamchuk, M. T. Morgan, H. Sumali. Application of a strain gauge array to estimate soil mechanical impedance on-the-go. Trans. ASAE 44 (2001): 1377-1383.

[70] P. Andrade-Sanchez, S.K Upadhyaya, B. Jenkins, J. Agüera. Evaluation of a capacitance based soil moisture sensor for real-time applications. Trans. ASAE 47 (2004): 1281-1287.

[71] E. Chukwu, C. G. Bowers. Instantaneous multiple-depth soil mechanical impedance sensing from a moving vehicle. Trans. ASABE 48 (2005): 885-894.

[72] S. O. Chung, K. A. Sudduth, J. W. Hummel. Design and validation of an on-the-go soil strength profile sensor. Trans. ASABE 49 (2006): 5-14.

[73] K. J. Bathe. Finite Element Procedures. Prentice Hall, (1996)

[74] R. A. Kepner, R. Bainer, E.L. Barger. Principles of farm machinery Westport, CT. The Avi publishing Co. (1972)

[75] R.J. Godwin, M.J. O'Dogherty. Integrated soil tillage force prediction models. Journal of Terramechanics. 44 (2007): 3-14

Appendix A

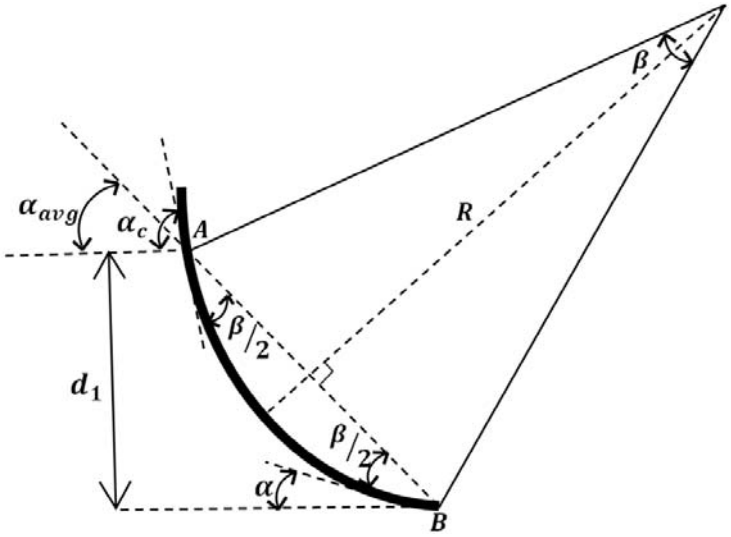

Figure A.1: Parameters characterizing a curved blade

$$\alpha_{avg} = \alpha_c - \frac{\beta}{2} \tag{1}$$

$$\alpha_{avg} = \frac{\beta}{2} + \alpha \tag{2}$$

$$\alpha_{avg} = \frac{\alpha_c + \alpha}{2} \tag{3}$$

$$\beta = \alpha_c - \alpha \tag{4}$$

$$AB = 2R\sin(\frac{\beta}{2}) \tag{5}$$

$$d_1 = AB\sin(\frac{\beta}{2} + \alpha) \tag{6}$$

$$d_1 = 2R\sin(\frac{\beta}{2}) \times \sin(\frac{\beta}{2} + \alpha) \tag{7}$$

$$d_1 = 2R\sin(\frac{\beta}{2}) \times \left[(\sin(\frac{\beta}{2})\cos(\alpha)) + (\cos(\frac{\beta}{2})\sin(\alpha)) \right] \tag{8}$$

$$d_1 = 2R \times \left[(\sin^2(\frac{\beta}{2})\cos(\alpha)) + (\sin(\frac{\beta}{2})\cos(\frac{\beta}{2})\sin(\alpha)) \right] \tag{9}$$

$$\cos(\beta) = \cos^2(\frac{\beta}{2}) - \sin^2(\frac{\beta}{2}) = 1 - 2\sin^2(\frac{\beta}{2}) \tag{10}$$

$$\sin(\beta) = 2\sin(\frac{\beta}{2})\cos(\frac{\beta}{2}) \tag{11}$$

$$d_1 = 2R \times \left[\cos(\alpha)(\frac{1-\cos(\beta)}{2}) + (\frac{\sin(\beta)\sin(\alpha)}{2}) \right] \tag{12}$$

$$d_1 = R \times \left[\cos(\alpha) - \cos(\alpha)\cos(\beta) + \sin(\beta)\sin(\alpha) \right] \tag{13}$$

$$d_1 = R \times \left[\cos(\alpha) - \cos(\beta + \alpha) \right] \tag{14}$$

By combining Eqs. (14) and (4), one arrives at:

$$d_1 = R \times \left[\cos(\alpha) - \cos(\alpha_c) \right] \tag{15}$$

$$R = \frac{d_1}{\cos(\alpha) - \cos(\alpha_c)} \tag{16}$$

Appendix B

In order to verify experimental results and decrease experimental error, at least four tests were performed on each blade with the same conditions (same rake angle, width, depth and speed) during the experimental procedure as shown in the Fig. B.1.

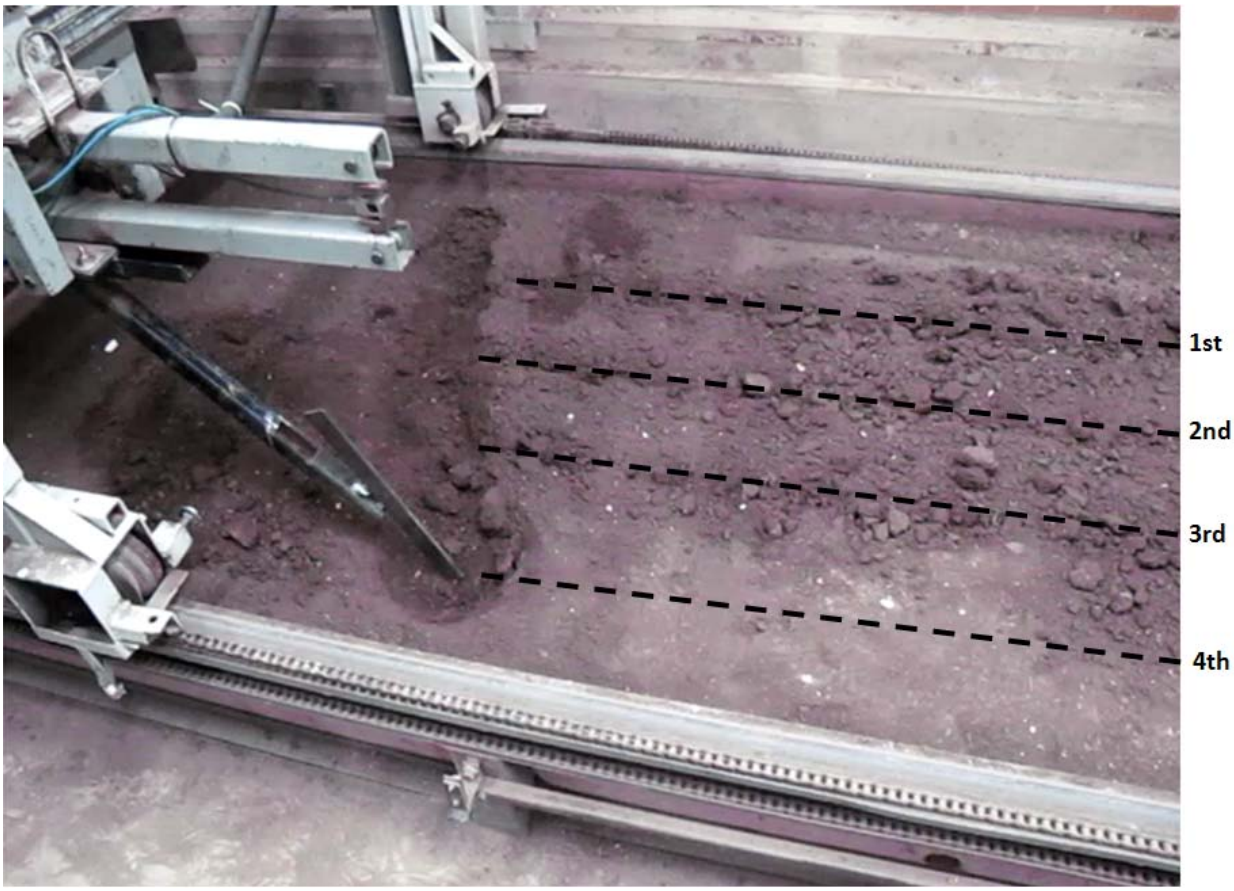

Figure B.1: repetition of the experimental tests on the same blade and same condition

Signals from load cells were filtered in order to find the corresponding blade's draft force after each test. Then the experimental draft forces are tabulated and the test with the mean value of draft force was selected as a reference test result for the specific blade configuration and blade's condition. As shown in Table B.1, the test results for rectangular blade with rake angle $\alpha = 60^{\circ}$ and depth of interaction $d_1 = 50mm$ and with of blade $W_1 = 40mm$ were tabulated; the 3rd test was selected as a reference for the experimental force result for this type of blade.

Table B.1: experimental tests results on the rectangular blade with $\alpha = 60^{\circ}$, $d_1 = 50mm$ and $W_1 = 40mm$

Test Number	**Final Draft Force**
1	427
2	409
3	415
4	406
5	413
6	419

Appendix C

A Sample of Ansys program for Curved rectangular blade with $\alpha = 45^{\circ}$ and $\alpha_c = 90^{\circ}$

```
Finish
/clear
/prep7
/title,soil
!mat 1(Blade)
Mp,ex,1,2e11
Mp,prxy,1,.3
Mp,dens,1, 7850
!Mat2(soil)
Mp,ex,2,5e6
Mp,prxy,2,.36
Mp,dens,2,1200
TB,DP,2
TBDATA,1,2e4,35,20
!--------- ------------------Modeling of Soil-----
Et,1,solid45
Keyopt,1,1,1
Keyopt,1,2,0
Type,1
Mat,1
r,1
!---------- Blade & soil bin parameter----------
h1=.05
w1=(.05)
d=.02
H=2*h1
W=(.24)
LS=.2
Lb=.05
LE=.05
HS=.1
HS1=HS-h1
R=.07
alp=77
HM=.26
Q=1.3
PI = 4*ATAN(1)
l=cos(alp*(PI/180))
m=sin(alp*(PI/180))
t=tan(alp*(PI/180))
!------------Modeling of blade-------------------------
k,400,-(H/t),((.7)*H+HS1),((W-w1)/2)
k,401,0,HS1,((W-w1)/2)
KK=-(sqrt((H*H)+((H/t)*(H/t))))
k,402,KK,HS1,((W-w1)/2)
k,403,(d-(H/t)),((.7)*H+HS1),((W-w1)/2)
k,404,d,HS1,((W-w1)/2)
k,405,(KK+.05),HS1,((W-w1)/2)
LARC,400,401,402,-R
LARC,403,404,405,-R
k,500,-(H/t),((.7)*H+HS1),((W+w1)/2)
k,501,0,HS1,((W+w1)/2)
k,502,KK,HS1,((W+w1)/2)
k,503,(d-(H/t)),((.7)*H+HS1),((W+w1)/2)
k,504,d,HS1,((W+w1)/2)
k,505,(KK+.05),HS1,((W+w1)/2)
LARC,500,501,502,-R
LARC,503,504,505,-R
!-------- -----------check HM here-------------------------
KL,1,HM,2,
kl,2,HM,5
l,504,501
l,503,500
l,401,404
l,400,403
l,400,500
l,403,503
l,404,504
```

```
l,401,501
type,1
mat,1
al,9,10,8,6
al,1,2,8,7
al,12,11,7,5
al,3,4,5,6
al,1,12,3,9
al,10,2,11,4
va,1,2,3,4,5,6
Lesize,1,,,7,
Lesize,2,,,7,
Lesize,3,,,7,
Lesize,4,,,7,
Lesize,9,,,6
Lesize,10,,,6
Lesize,11,,,6
Lesize,12,,,6
Lesize,5,,,3
Lesize,6,,,3
Lesize,7,,,3
Lesize,8,,,3
MSHKEY,1
MSHAPE,0,3d
vmesh,1
!---------- Modeling of soil----------
type,1
mat,2
!----------Modeling of lines----------
k,100,0,0,0
k,101,LS,0,0
k,102,LS,HS,0
k,103,LS,HS,W
k,104,LS,0,W
k,105,LS,HS1,0
k,106,LS,HS1,W
k,107,LS,HS,(W-w1)/2
k,108,LS,HS,(W+w1)/2
k,109,LS,HS1,(W-w1)/2
k,110,LS,HS1,(W+w1)/2
k,111,LS,0,(W-w1)/2
k,112,LS,0,(W+w1)/2
k,113,Lb,0,0
k,114,Lb,HS,0
k,115,Lb,HS1,0
k,116,Lb,HS,(W-w1)/2
k,117,Lb,HS1,(W-w1)/2
k,118,Lb,0,(W-w1)/2
k,119,Lb,HS,(W+w1)/2
k,120,Lb,HS1,(W+w1)/2
k,121,Lb,0,(W+w1)/2
k,122,Lb,HS,W
k,123,Lb,HS1,W
k,124,Lb,0,W
k,125,d,0,W
k,126,d,0,(W+w1)/2
k,127,d,0,(W-w1)/2
k,128,d,0,0
k,129,d,HS1,0
k,130,d,HS1,((W-w1)/2)
k,131,d,HS1,((W+w1)/2)
k,132,d,HS1,W
!-----first arc-------------------------
k,601,(d-(H/t)),((.7)*H+HS1),((W+w1)/2)
k,602,d,HS1,((W+w1)/2)
k,603,(KK+.05),HS1,((W+w1)/2)
LARC,601,602,603,-R
KL,13,HM,604
```

```
LARC,604,602,603,-R
!-----second arc------------
k,701,(d-(H/t)),((.7)*H+HS1),((W-w1)/2)
k,702,d,HS1,((W-w1)/2)
k,703,(KK+.05),HS1,((W-w1)/2)
LARC,701,702,703,-R
KL,15,HM,704
LARC,704,702,703,-R
!-----Third arc------------
k,801,(d-(H/t)),((.7)*H+HS1),0
k,802,d,HS1,0
k,803,(KK+.05),HS1,0
LARC,801,802,803,-R
KL,17,HM,804
LARC,804,802,803,-R
!-----forth arc------------
k,901,(d-(H/t)),((.7)*H+HS1),W
k,902,d,HS1,W
k,903,(KK+.05),HS1,W
LARC,901,902,903,-R
KL,19,HM,904
LARC,904,902,903,-R
!-----doublicate first arc------------
k,1001,(d-(H/t)),((.7)*H+HS1),((W+w1)/2)
k,1002,(KK+.05),HS1,((W+w1)/2)
LARC,1001,131,1002,-R
KL,13,HM,1003
LARC,1003,131,1002,-R
!-----doublicate second arc------------
k,1004,(d-(H/t)),((.7)*H+HS1),((W-w1)/2)
k,1005,(KK+.05),HS1,((W-w1)/2)
LARC,1004,130,1005,-R
KL,15,HM,1006
LARC,1006,130,1005,-R
```

```
!----------------Modeling of Volumes------
!-------Volume 2 ------
l,904,604
l,602,902
l,122,904
l,123,902
l,119,604
l,120,602
l,122,119
l,123,120
l,119,120
l,122,123
al,31,29,25,27
al,32,30,28,26
al,20,34,27,28
al,31,32,33,34
al,30,14,33,29
al,14,25,20,26
va,7,8,9,10,11,12
Lesize,25,,,4,.2
Lesize,26,,,4,5
Lesize,31,,,4,.2
Lesize,32,,,4,.2
Lesize,33,,,6,
Lesize,14,,,6,Q
Lesize,20,,,6,Q
Lesize,34,,,6,
Lesize,30,,,6
Lesize,29,,,6
Lesize,28,,,6
Lesize,27,,,6
MSHKEY,1
MSHAPE,0,3d
vmesh,2
```

```
!------Volume 3 ------
l,1006,1003
l,119,116
l,120,131
l,120,117
l,131,130
l,117,130
l,116,1006
l,116,117
l,119,1003
al,41,35,36,43
al,37,38,40,39
al,22,37,33,43
al,38,33,36,42
al,40,42,41,24
al,24,39,22,35
va,13,14,15,16,17,18
Lesize,35,,,6
Lesize,36,,,6
Lesize,39,,,6
Lesize,38,,,6
Lesize,33,,,6,
Lesize,22,,,6,Q
Lesize,24,,,6,Q
Lesize,42,,,6,
Lesize,37,,,6
Lesize,40,,,6
Lesize,41,,,6
Lesize,43,,,6
MSHKEY,1
MSHAPE,0,3d
vmesh,3
!-------Volume 4 ------
l,704,804
l,702,802
l,704,116
l,702,117
l,117,115
l,116,114
l,114,115
l,114,804
l,115,802
al,51,44,49,46
al,45,52,47,48
al,46,42,47,16
al,42,48,50,49
al,50,51,18,52
al,18,44,16,45
va,19,20,21,22,23,24
Lesize,44,,,4,5
Lesize,49,,,4,5
Lesize,48,,,4,5
Lesize,45,,,4,5
Lesize,50,,,6,
Lesize,18,,,6,Q
Lesize,16,,,6,Q
Lesize,51,,,6
Lesize,52,,,6
Lesize,40,,,6
Lesize,46,,,6
MSHKEY,1
MSHAPE,0,3d
vmesh,4
!-------Volume 5 ------
l,123,124
l,120,121
l,124,121
l,125,124
```

```
l,125,126
l,126,121
l,902,125
l,602,126
al,57,55,56,58
al,28,56,53,59
al,55,32,54,53
al,54,30,60,58
al,26,60,57,59
va,8,25,26,27,28,29
Lesize,54,,,3,5
Lesize,60,,,3,5
Lesize,53,,,3,5
Lesize,59,,,3,5
Lesize,57,,,4,.2
Lesize,55,,,4,.2
Lesize,56,,,6
Lesize,58,,,6
MSHKEY,1
MSHAPE,0,3d
vmesh,5
!-------Volume 6 ------
l,121,118
l,117,118
l,127,118
l,127,126
l,127,702
l,602,702
al,47,38,30,66
al,61,58,64,63
al,54,61,62,38
al,62,47,65,63
al,66,60,64,65
va,28,30,31,32,33,34
Lesize,66,,,6
Lesize,64,,,6
Lesize,61,,,6
Lesize,63,,,6
Lesize,62,,,3,5
Lesize,65,,,3,.2
MSHKEY,1
MSHAPE,0,3d
vmesh,6
!-------Volume 7 ------
l,118,113
l,128,113
l,128,127
l,115,113
l,128,802
al,67,68,69,63
al,70,67,62,48
al,70,52,71,68
al,45,71,69,65
va,33,20,35,36,37,38
Lesize,67,,,4,5
Lesize,69,,,4,.2
Lesize,68,,,6
Lesize,70,,,3,5
Lesize,71,,,3,.2
MSHKEY,1
MSHAPE,0,3d
vmesh,7
!-------Volume 8 ------
l,123,106
l,124,104
l,120,110
l,121,112
l,110,106
```

```
l,106,104
l,104,112
l,110,112
al,74,32,72,76
al,55,73,78,75
al,72,53,73,77
al,76,77,78,79
al,74,79,75,54
va,27,39,40,41,42,43
Lesize,74,,,5,10
Lesize,75,,,5,10
Lesize,72,,,5,10
Lesize,73,,,5,10
Lesize,76,,,4,5
Lesize,78,,,4,.2
Lesize,77,,,3,5
Lesize,79,,,3,5
MSHKEY,1
MSHAPE,0,3d
vmesh,8
!-------Volume 9 ------
l,109,110
l,111,112
l,117,109
l,118,111
l,109,111
al,82,74,38,80
al,75,81,83,61
al,80,84,81,79
al,84,82,83,62
va,32,43,44,45,46,47
Lesize,82,,,5,10
Lesize,83,,,5,10
Lesize,80,,,6
Lesize,81,,,6
Lesize,84,,,3,5
MSHKEY,1
MSHAPE,0,3d
vmesh,9
!-------Volume 10 ------
l,105,109
l,101,105
l,101,111
l,101,113
l,105,115
al,89,48,82,85
al,87,88,67,83
al,85,86,87,84
al,89,70,88,86
va,36,47,48,49,50,51
Lesize,89,,,5,.1
Lesize,88,,,5,.1
Lesize,85,,,4,.2
Lesize,87,,,4,.2
Lesize,86,,,3,.2
MSHKEY,1
MSHAPE,0,3d
vmesh,10
!-------Volume 11 ------
l,108,110
l,103,106
l,122,103
l,103,108
l,119,108
al,94,31,92,93
al,92,91,72,34
al,93,90,76,91
al,94,90,74,33
```

```
va,10,39,52,53,54,55
Lesize,92,,,5,10
Lesize,94,,,5,10
Lesize,91,,,6,
Lesize,90,,,6,
Lesize,93,,,4,.2
MSHKEY,1
MSHAPE,0,3d
vmesh,11
!-------Volume 12 ------
l,108,107
l,107,109
l,116,107
al,97,94,95,36
al,95,96,80,90
al,97,96,82,42
va,16,55,44,56,57,58
Lesize,97,,,5,10
Lesize,95,,,6
Lesize,96,,,6,
MSHKEY,1
MSHAPE,0,3d
vmesh,12
!-------Volume 13 ------
l,105,102
l,102,107
l,102,114
al,100,49,97,99
al,99,98,85,96
al,100,98,89,50
va,22,58,48,59,60,61
Lesize,100,,,5,.1
Lesize,99,,,4,.2
Lesize,98,,,6,2
MSHKEY,1
MSHAPE,0,3d
vmesh,13
!-------Volume 14 ------
k,1100,-LE,0,W
k,1101,-LE,0,((W+w1)/2)
k,1102,-LE,HS1,W
k,1103,-LE,HS1,((W+w1)/2)
l,1102,902
l,1102,1103
l,1103,602
l,125,1100
l,126,1101
l,1100,1101
l,1100,1102
l,1101,1103
al,102,101,26,103
al,104,106,105,57
al,107,101,59,104
al,103,60,105,108
al,102,107,106,108
va,62,63,64,65,66,29
Lesize,108,,,3,.2
Lesize,107,,,3,.2
Lesize,106,,,4,.2
Lesize,102,,,4,.2
Lesize,105,,,3,10
Lesize,104,,,3,10
Lesize,101,,,3,.1
Lesize,103,,,3,.1
MSHKEY,1
MSHAPE,0,3d
vmesh,14
!-------Volume 15 ------
```

k,1200,-LE,HS,W

k,1201,-LE,HS,((W+w1)/2)

l,1200,1201

l,1200,1102

l,1201,1103

l,1200,904

l,1201,604

al,109,112,25,113

al,112,110,101,20

al,113,111,103,14

al,109,110,102,111

va,12,62,67,68,69,70

Lesize,110,,,6,

Lesize,111,,,6,

Lesize,112,,,3

Lesize,113,,,3

Lesize,109,,,4,.2

MSHKEY,1

MSHAPE,0,3d

vmesh,15

!-------Volume 16 ------

k,1300,-LE,0,((W-w1)/2)

k,1301,-LE,HS1,((W-w1)/2)

l,1103,1301

l,1301,1300

l,1300,1101

l,1301,702

l,1300,127

al,114,115,116,108

al,115,117,65,118

al,117,114,103,66

al,118,116,105,64

va,34,65,71,72,73,74

Lesize,115,,,3,5

Lesize,116,,,6

Lesize,114,,,6

Lesize,118,,,3,.1

Lesize,117,,,3,.1

MSHKEY,1

MSHAPE,0,3d

vmesh,16

!-------Volume 17 ------

k,1400,-LE,0,0

k,1401,-LE,HS1,0

l,1401,1400

l,1401,802

l,1400,128

l,1400,1300

l,1401,1301

al,120,123,117,45

al,122,121,69,118

al,119,123,115,122

al,120,119,121,71

va,72,38,75,76,77,78

Lesize,119,,,3,5

Lesize,122,,,4,.2

Lesize,121,,,3,.1

Lesize,120,,,3,.1

Lesize,123,,,4,.2

MSHKEY,1

MSHAPE,0,3d

vmesh,17

!-------Volume 18 ------

k,1500,-LE,HS,0

k,1501,-LE,HS,((W-w1)/2)

l,1501,1500

l,1500,1401

l,1500,804

```
l,1501,704
l,1501,1301
al,124,126,127,44
al,124,125,123,128
al,126,125,120,18
al,127,128,117,16
va,24,75,79,80,81,82
Lesize,126,,,3
Lesize,124,,,4,5
Lesize,125,,,6,
Lesize,128,,,6,
Lesize,127,,,3
MSHKEY,1
MSHAPE,0,3d
vmesh,18
/pnum,area,1
/pnum,kp,1
!---- ----------Contact element------------------
Et,2,conta173
Et,3,targe170
KEYOPT,2,1,0
KEYOPT,2,10,2
KEYOPT,2,12,2
Et,4,conta173
KEYOPT,4,1,0
KEYOPT,4,10,2
KEYOPT,4,12,3
Et,5,targe170
!-------------- blade contact--------
ASEL,S,,,6
NSLA,S,1
real,1
TYPE,2
mat,1
ESURF
ALLSEL,all
ASEL,S,,,18
NSLA,S,1
TYPE,3
mat,2
ESURF
ALLSEL,ALL
!------------ soil contact(above volume) --------
ASEL,S,,,14
NSLA,S,1
real,2
TYPE,3
mat,2
ESURF
ALLSEL,all
ASEL,S,,,30
NSLA,S,1
TYPE,4
mat,2
ESURF
ALLSEL,ALL
!----- ----------soil contact(left volume) --------
ASEL,S,,,15
NSLA,S,1
real,2
TYPE,3
mat,2
ESURF
ALLSEL,all
ASEL,S,,,11
NSLA,S,1
TYPE,4
mat,2
```

```
ESURF
ALLSEL,ALL
!------------ soil contact(right volume) ----
ASEL,S,,,17
NSLA,S,1
real,2
TYPE,3
mat,2
ESURF
ALLSEL,all
ASEL,S,,,21
NSLA,S,1
TYPE,4
mat,2
ESURF
ALLSEL,ALL
!----------------- soil contact(above volume) ----
ASEL,S,,,14
NSLA,S,1
real,1
TYPE,2
mat,2
ESURF
ALLSEL,all
ASEL,S,,,30
NSLA,S,1
TYPE,5
mat,2
ESURF
ALLSEL,ALL
!----- ----------------soil contact(left) ----
ASEL,S,,,15
NSLA,S,1
real,1
TYPE,2
mat,2
ESURF
ALLSEL,all
ASEL,S,,,11
NSLA,S,1
TYPE,5
mat,2
ESURF
ALLSEL,ALL
!-------- -------------soil contact(right) ----
ASEL,S,,,17
NSLA,S,1
real,1
TYPE,2
mat,2
ESURF
ALLSEL,all
ASEL,S,,,21
NSLA,S,1
TYPE,5
mat,2
ESURF
ALLSEL,ALL
*do,k,1,216
ekill,2076+k
*enddo
!---------------solution------------
/solu
Antype,0
SOLCONTROL,ON
Autots,on
Nlgeom,on
neqit,100
```

```
ACEL,,9.8
!------------Boundary Constrain
ASEL,S,,,64
NSLA,S,1
d,all,all
nsel,all
ASEL,S,,,68
NSLA,S,1
d,all,all
nsel,all
ASEL,S,,,9
NSLA,S,1
d,all,all
nsel,all
ASEL,S,,,26
NSLA,S,1
d,all,all
nsel,all
ASEL,S,,,53
NSLA,S,1
d,all,all
nsel,all
ASEL,S,,,41
NSLA,S,1
d,all,all
nsel,all
ASEL,S,,,54
NSLA,S,1
d,all,all
nsel,all
ASEL,S,,,57
NSLA,S,1
d,all,all
nsel,all
ASEL,S,,,42
NSLA,S,1
d,all,all
nsel,all
ASEL,S,,,46
NSLA,S,1
d,all,all
nsel,all
ASEL,S,,,60
NSLA,S,1
d,all,all
nsel,all
ASEL,S,,,50
NSLA,S,1
d,all,all
nsel,all
ASEL,S,,,61
NSLA,S,1
d,all,all
nsel,all
ASEL,S,,,51
NSLA,S,1
d,all,all
nsel,all
ASEL,S,,,37
NSLA,S,1
d,all,all
nsel,all
ASEL,S,,,23
NSLA,S,1
d,all,all
nsel,all
ASEL,S,,,78
NSLA,S,1
```

d,all,all

nsel,all

ASEL,S,,,81

NSLA,S,1

d,all,all

nsel,all

ASEL,S,,,49

NSLA,S,1

d,all,all

nsel,all

ASEL,S,,,45

NSLA,S,1

d,all,all

nsel,all

ASEL,S,,,40

NSLA,S,1

d,all,all

nsel,all

ASEL,S,,,35

NSLA,S,1

d,all,all

nsel,all

ASEL,S,,,25

NSLA,S,1

d,all,all

nsel,all

ASEL,S,,,31

NSLA,S,1

d,all,all

nsel,all

ASEL,S,,,74

NSLA,S,1

d,all,all

nsel,all

ASEL,S,,,76

NSLA,S,1

d,all,all

nsel,all

ASEL,S,,,63

NSLA,S,1

d,all,all

nsel,all

ASEL,S,,,70

NSLA,S,1

d,all,all

nsel,all

ASEL,S,,,66

NSLA,S,1

d,all,all

nsel,all

ASEL,S,,,71

NSLA,S,1

d,all,all

nsel,all

ASEL,S,,,80

NSLA,S,1

d,all,all

nsel,all

ASEL,S,,,77

NSLA,S,1

d,all,all

nsel,all

ASEL,S,,,1

NSLA,S,1

d,all,uy,0

d,all,uz,0

nsel,all

```
ASEL,S,,,30
NSLA,S,1
d,all,uy,0
nsel,all
!------------ ----------Do loop--------
*do,i,1,10
*if,i,eq,1,then
!-------- motion of the blade--------
*do,j,1,7
time,j/2
aSEL,S,,,5
NSLa,S,1
d,all,ux,((0)+((j)*0.00045))
nsel,all
nsub,800
solve
*enddo
*elseif,i,eq,2,then
*do,j,8,11
time,j/2
aSEL,S,,,5
NSLa,S,1
d,all,ux,((.00315)+((j-8)*0.0004))
nsel,all
nsub,800
solve
*enddo
*elseif,i,eq,3,then
*do,j,12,15
time,j/2
aSEL,S,,,5
NSLa,S,1
d,all,ux,((.00435)+((j-12)*0.0004))
nsel,all
nsub,800
solve
*enddo
*elseif,i,eq,4,then
*do,j,16,30
time,j/2
aSEL,S,,,5
NSLa,S,1
d,all,ux,((.00555)+((j-16)*0.0003))
nsel,all
nsub,800
solve
*enddo
*elseif,i,eq,5,then
*do,j,18,50
time,j/2
aSEL,S,,,5
NSLa,S,1
d,all,ux,((.0087)+((j-18)*0.0006))
nsel,all
nsub,800
solve
*enddo
*elseif,i,eq,6,then
*do,j,28,80
time,j/2
aSEL,S,,,5
NSLa,S,1
d,all,ux,((.0143)+((j-28)*0.0005))
nsel,all
nsub,800
solve
*enddo
*endif
```

!-- killing the contact element between (Above and Below)

!-------------above

ekill,(1896-(6*i)+1)

ekill,(1896-(6*i)+2)

ekill,(1896-(6*i)+3)

ekill,(1896-(6*i)+4)

ekill,(1896-(6*i)+5)

ekill,(1896-(6*i)+6)

!-------------below

ekill,(1903-i)

ekill,(1909-i)

ekill,(1915-i)

ekill,(1921-i)

ekill,(1927-i)

ekill,(1933-i)

ealive,(2112-(6*i)+1)

ealive,(2112-(6*i)+2)

ealive,(2112-(6*i)+3)

ealive,(2112-(6*i)+4)

ealive,(2112-(6*i)+5)

ealive,(2112-(6*i)+6)

!-------------below

ealive,(2119-i)

ealive,(2125-i)

ealive,(2131-i)

ealive,(2137-i)

ealive,(2143-i)

ealive,(2149-i)

!----- killing the contact element between (Above and left)

!-------------above

ekill,(1939-i)

ekill,(1945-i)

ekill,(1951-i)

ekill,(1957-i)

ekill,(1963-i)

ekill,(1969-i)

!-------------left

ekill,(1975-i)

ekill,(1981-i)

ekill,(1987-i)

ekill,(1993-i)

ekill,(1999-i)

ekill,(2005-i)

!-------------above

ealive,(2155-i)

ealive,(2161-i)

ealive,(2167-i)

ealive,(2173-i)

ealive,(2179-i)

ealive,(2185-i)

!-------------left

ealive,(2191-i)

ealive,(2197-i)

ealive,(2203-i)

ealive,(2209-i)

ealive,(2215-i)

ealive,(2221-i)

!-- -- killing the contact element between (Above and right)

!-------------above

ekill,(2011-i)

ekill,(2017-i)

ekill,(2023-i)

ekill,(2029-i)

ekill,(2035-i)

ekill,(2041-i)

!-------------right

ekill,(2047-i)

ekill,(2053-i)

ekill,(2059-i)

ekill,(2065-i)

ekill,(2071-i)

ekill,(2077-i)

!----------above

ealive,(2227-i)

ealive,(2233-i)

ealive,(2239-i)

ealive,(2245-i)

ealive,(2251-i)

ealive,(2257-i)

!----------right

ealive,(2263-i)

ealive,(2269-i)

ealive,(2275-i)

ealive,(2281-i)

ealive,(2287-i)

ealive,(2293-i)

!----------

*enddo